ABSTRACT

CHAPMAN, BRIAN STEVEN. Magnetic Functionalization of Silica-Overcoated Gold Nanorods via Heteroaggregation and Direct Electrospinning of Sol Gel Derived Oxide Fibers. (Under the direction of Dr. Joseph B. Tracy).

Gold nanorods (GNRs) have garnered significant interest for applications in photothermal therapy, drug delivery, catalysis, and biomedical imaging because of their shape-dependent localized surface plasmon resonance (LSPR). GNRs are also of interest for use in multifunctional composite nanoparticles (NPs) consisting of multiple NPs with different properties, which can have novel optical, magnetic, and catalytic properties. Another field of growing interest is electrospun ceramic fibers with sub-μm diameters and lengths of 100s of μm for applications including filtration, sensors, electronics and photovoltaics.

Three advancements in the fields of colloidal NPs and ceramic electrospinning are discussed in this dissertation: (1) The development of a novel method for assembling composite NPs that exploits the aggregation properties of hydrophobic NPs when exposed to polar solvents. In this work, hydrophobic, oleylamine-stabilized magnetite NPs (Fe_3O_4 NPs) dispersed in hexanes assemble into dense coatings on the surface of silica-overcoated GNRs (SiO_2-GNRs) dispersed in ethanol when these dispersions are mixed. By using an optimized volume ratio of ethanol to hexanes (2:1), heteroaggregation of Fe_3O_4 onto the SiO_2 surface occurs, while avoiding homoaggregation of Fe_3O_4 and SiO_2-GNRs. These composites are shown to be stable, magnetically responsive, and can be dispersed in nonpolar solvents. Their surfaces can also be modified for dispersion in polar solvents. (2) The development of direct electrospun titania (TiO_2) fibers using ethanol with diameters smaller than 100 nm. In direct electrospinning, fibers are electrospun from a viscous sol without using a polymer

additive to assist in fiber formation. In comparison, previous research on direct electrospun fibers required the use the toxic solvent, 2-methoxyethanol, and achieved fiber diameters of ~500-1500 nm. (3) The development of direct electrospun SiO_2 fibers containing SiO_2-GNRs and a study of their thermal stability when heated in air. The fibers are shown to be heat stable to above 900 °C, while the SiO_2-GNRs are shown to be stable to 600 °C.

Magnetic Functionalization of Silica-Overcoated Gold Nanorods via Heteroaggregation and Direct Electrospinning of Sol Gel Derived Oxide Nanofibers

by
Brian Steven Chapman

A dissertation submitted to the Graduate Faculty of
North Carolina State University
in partial fulfillment of the
requirements for the degree of
Doctor of Philosophy

Materials Science and Engineering

Raleigh, North Carolina

2017

APPROVED BY:

_____	_____
Dr. Joseph B. Tracy Committee Chair	Dr. Yaroslava G. Yingling
_____	_____
Dr. Thomas H. LaBean	Dr. Orlin D. Velev

DEDICATION

I dedicate this to my wife, Emily and my daughter, Eliza. Getting a Ph.D. is hard, and I don’t think I could have done it without them.

BIOGRAPHY

I was born on July 18, 1985 to parents James Chapman and Kathy Chapman. I was raised in Howell, Michigan with my brothers Andrew Chapman, Paul Chapman, Thomas Chapman, and Richard Chapman. For my undergraduate studies, I attended Michigan State University and graduated in 2008 with a B.S. in Chemistry. I then worked as a high school Chemistry teacher in Charles County, Maryland, where I met my wife, Emily Rhode. In 2012, I made the decision to return to school to pursue a Ph.D. I was accepted into the Ph.D. program at North Carolina State University and joined Joseph Tracy's research group, where I studied colloidal nanoparticles. My daughter, Eliza Kathryn Rhode Chapman was born November 10th, 2016.

ACKNOWLEDGMENTS

First, I would like to thank my wife who has supported me for the past 5 years as I pursued a Ph.D. in Materials Science and Engineering. It hasn't always been easy, but when things became overwhelming, she was there for me. I could not have done this without her.

I would also like to thank my parents, James and Kathy, and my brothers, Andrew, Paul, Thomas, and Richard. I grew up in a vibrant and inquisitive home that gave me the foundation to be the man that I am today.

I would like to thank my Advisor, Dr. Joseph Tracy for the guidance and mentorship that he has provided me over the years. I would also like to thank current and former members of the Tracy Research Group who have helped me with my research. In particular, I would like to thank Wei-Chen Wu (Ivy), who taught me so much of what I know about gold nanorods.

I would also like to thank Richard and Judith Rhode for their support and all the times they watched Eliza while I worked on my dissertation.

TABLE OF CONTENTS

List of Figures viii
Chapter 1. Noble Metal Nanoparticles 1
1.1 Development of Noble Metal Nanoparticle Synthesis 1
1.2 Turkevich Method 2
1.3 Optical Properties of Gold Nanoparticles 3
1.3.1 Composition 5
1.3.2 Size 6
1.3.3 Shape 7
1.3.4 Dielectric 8
1.4 Electrostatic Stabilization 9
1.5 References 12
Chapter 2. Gold Nanorods 16
2.1 Optical Properties 16
2.1.1 Polarization Dependence 16
2.1.2 Dielectric 17
2.2 Gold Nanorod Synthesis 19
2.2.1 Development of CTAB-Coated Gold Nanorods 19
2.3 Secondary Injection of Ascorbic Acid 21
2.4 Factors Influencing the Synthesis of Gold Nanorods 22
2.4.1 Silver Ions 22
2.4.2 Bromide Ions 23
2.4.3 Secondary Injection Rate 23
2.4.4 Temperature 24
2.4.5 pH 24
2.4.6 Seed Concentration 25
2.5 Stabilization 25
2.5.1 CTAB 25
2.5.2 Polyethylene glycol 27
2.5.3 Silica 29
2.6 Reproducibility Challenges 30
2.7 References 32
Chapter 3. Electrospinning Ceramic Fibers 37
3.1 Apparatus and Mechanism 37
3.2 Electrospinning Parameters 39
3.2.1 Concentration of Solution for Electrospinning 40
3.2.2 Flow Rate 40
3.2.3 Applied Voltage 41
3.2.4 Distance 41
3.3 Patterning Fibers 42
3.4 Ceramic Fibers 45
3.4.1 Polymer-Assisted Electrospinning 45

3.4.2 Direct Electrospinning 46
3.5 References 50
Chapter 4. Aggregation and DLVO Theory 54
4.1 DLVO Theory 54
4.2 Non-DLVO Forces 57
4.2.1 Steric Stabilization 58
4.2.2 Osmotic Repulsion 59
4.2.3.Hydrophobic Effect 59
4.2.4 Solvation Forces 60
4.2.5 Heteroaggregation 61
4.3 Aggregate Morphology 62
4.4 Inducing Aggregation 64
4.5 References 66
Chapter 5. Heteroaggregation Approach for Depositing Magnetite Nanoparticles onto Silica-Overcoated Gold Nanorods 70
5.1 Introduction 70
5.2 Experimental Section 75
5.2.1 Assembly of Fe_3O_4-SiO_2-GNRs 75
5.2.2 Functionalization of Fe_3O_4-SiO_2-GNRs with PEG-Catechol 76
5.2.3 Characterization 77
5.3 Results and Discussion 77
5.3.1 Mechanism of Heteroaggregation 78
5.3.2 Optical Properties 79
5.3.3 Magnetic Separation 80
5.3.4 Stability 82
5.3.5 Functionalization for Dispersion in Water 83
5.4 Conclusions 85
5.5 References 86
5.6 Supporting Information 93
5.6.1 Chemicals for Nanoparticle Synthesis, Purification, and Heteroaggregation 93
5.6.2 Synthesis of SiO_2-GNRs 93
5.6.3 Synthesis of Fe_3O_4 NPs 94
5.6.4 Synthesis and Purification of PEG-Catechol 95
5.6.4.1 Chemicals for Synthesis of PEG-Catechol 95
5.6.4.2 Synthesis and Purification of PEG-Catechol 96
5.6.5 Unnormalized Optical Absorbance Spectra 97
5.6.7 References for Supporting Information 98
Chapter 6. Direct Electrospinning of Titania Fibers with Ethanol 99
6.1 Introduction 99
6.2 Experimental Section 102
6.2.1 Sol Gel Synthesis 102

6.2.2 Electrospinning 103
6.2.3 Characterization and Conversion into Anatase TiO_2 104
6.3 Results and Discussion 104
6.3.1 Fiber Morphology 104
6.3.2 Guidance for Preparing the TiO_2 Sol 106
6.3.2 Guidance for Electrospinning 107
6.3.3 *In Situ* X-Ray Diffraction 108
6.4 Conclusions 110
6.5 References 111
Chapter 7: Silica-Overcoated Gold Nanorods in Direct Electrospun Silica Nanofibers 114
7.1 Introduction 114
7.2 Experimental 116
7.2.1 Chemicals 116
7.2.2 Synthesis of Silica-Overcoated Gold Nanorods 117
7.2.3 Preparation of Sol for Direct Electrospinning 118
7.2.4 Electrospinning 118
7.2.5 Heating 119
7.3 Results 120
7.4 Conclusions 124
7.5 References 125
Chapter 8. Contributions to Other Projects 127
8.1 Longitudinal Alignment and Optical Characterization of Gold Nanostars in Electrospun Polymer Fibers 127
8.2 PEGylated Gold Nanorods for Diffusion-Sensitive Optical Coherence Tomography 128
8.3 Silica-Overcoated Zeolite Nanoplatelets 129
8.4 Low Aspect-Ratio Gold Nanorods 130
8.5 References 131
Appendix 133
Appendix 1. Short Aspect Ratio Gold Nanorods 134
Appendix 2. PEGylation 136
Appendix 3. Identifying a Good Batch of CTAB 138
Appendix References 142

LIST OF FIGURES

Figure 1.1 The Lycurgus Cup, an example of noble metal NPsa embedded in glass, made in the 4th century BC. (Left) Cup, when illuminated from outside, scatters light. (Middle) Cup, when illuminated from inside, absorbs light. (Right) TEM micrograph of AgAu NPs present in cup. 2

Figure 1.2 16-nm citrate stabilized gold nanoparticles, published by Frens in 1973. 3

Figure 1.3 A diagram representing the collective oscillation of delocalized electrons in response to an electromagnetic field. 4

Figure 1.4 Calculated change in the extinction efficiency of a silver NP as it transitions from a cube to an icosahedron to a sphere. 8

Figure 1.5 Diagram of the Stern-Guoy-Chapman model of the electrostatic bilayer. 11

Figure 1.6 Plot of the surface potential from the SGC model as a function of distance from the charged surface at two electrolyte concentrations. 12

Figure 2.1 Absorption spectra of GNRs aligned in a poly(vinyl alcohol) thin film when excited with polarized light. 0° and 90° correspond to light parallel and perpendicular to the long axis of the GNRs, respectively. 17

Figure 2.2 (Left) Simulations showing the impact of the dielectric on the medium surrounding GNRs with an aspect ratio of 3.5 on their surface plasmon resonance. (Right) Simulations of extinction spectra of SiO_2-GNRs illustrating how the thickness of SiO_2 shells affects the LSPR. 18

Figure 2.3 Phase diagram of the structure of aqueous CTAB as a function of temperature and concentration. 26

Figure 2.4 Depiction of the bilayer structure of CTAB-stabilized GNRs. 27

Figure 2.5 GNR synthesis performed using CTAB from (a) Fluka, (b) MP Biomedicals, (c) Acros, (d) Sigma, and (e) Aldrich. The top row (1) is TEM and the bottom row (2) is SEM. 31

Figure 3.1 The basic electrospinning set-up using a high-voltage power supply, syringe pump (not shown), spinneret, and a collector plate. This set up produces non-woven fiber assemblies. 38

Figure 3.2 Image (top) and schematic (bottom) of the Taylor cone that forms during the electrospinning process when an increasing electric field (from left to right) is applied. As the field increases, charges on the surface increase, stretching the bead into a conical shape. 39

Figure 3.3 Various collectors for patterning electrospun fibers: (a) rotating drum, (b) rotating wire drum, (c) rotating disk, (d) parallel electrodes, (e) electrode array, and (f) hoop. Electrode diagrams are from Teo and Ramakrishna. 44

Figure 3.4 The difference in sol and gel structure when formed in an acidic and a basic solution. 48

Figure 3.5 The morphology of a silica sol when the ratio of water to alkoxide is (a) > 2 or (b) < 2. 49

Figure 4.1 Schematic of the interaction energy curve (V_t) of two particles, as a sum the van der Waals, V_{vdW}, and the electrostatic bilayer, V_{es}, terms as a function of separation distance. E_a is the energy barrier to aggregation and E_w is energy well that keeps aggregated particles attached to one another. Schematic is not to scale, instead elements are adjusted to enhance clarity. 56

Figure 4.2 Three regimes of aggregation behavior, determined by the height of the aggregation barrier, E_a: (a) high aggregation barrier, $E_a > kT$, (b) low aggregation barrier, $E_a < kT$, and (c) no aggregation barrier. 57

Figure 4.3 Schematic of the interaction energies in a binary particle system. E_{AA}, E_{BB}, and $E_{AB,}$ are the aggregation barriers for each type of aggregation. 62

Figure 4.4 From top to bottom, TEM images of gold, silica, polystyrene, and simulated particles that have undergone (left) DLCA and (right) RLCA. 63

Figure 4.5 Homoaggregation of hydrophobic gold NPs (top) to form controlled nanoclusters (bottom) through the addition of water. Adding water decreases the barrier to aggregation. 65

Figure 5.1 TEM images (common scale bar) of (a) SiO_2-GNRs with 19 nm SiO_2 shells, (b) 7-nm Fe_3O_4 NPs, and (c) Fe_3O_4-SiO_2-GNRs formed by heteroaggregation of Fe_3O_4 NPs onto SiO_2-GNRs. 78

Figure 5.2 Optical absorbance spectra of the assembly and purification of (1a) SiO_2-GNRs in ethanol and (1b) Fe_3O_4 NPs in hexanes: (2) unpurified Fe_3O_4-SiO_2-GNRs upon mixing and (3) Fe_3O_4-SiO_2-GNRs after centrifugation and redispersion in hexanes. Note: The SiO_2-GNR stock solution was diluted with 2 volumea of ethanol for acquiring (1a), and the Fe_3O_4 NP stock solution was diluted with half a volume of hexanes for acquiring (1b). These dilutions were chosen to mimic mixing of the stock solutions at the 2:1 hexanes:ethanol volume ratio for heteroaggregation, (2). After centrifugation, the product was redispersed in the same volume of solvent as before purification for acquiring (3). 80

Figure 5.3 (a) Photos of the magnetic separation process conducted over 45 minutes. (b) Optical absorbance spectra of Fe_3O_4-SiO_2-GNRs remaining dispersed in hexanes in the top of the cuvette while placing a permanent magnet next to the bottom of the cuvette for magnetic separation. Spectra were collected in 5-minute intervals for 45 minutes, and an additional spectrum was acquired after 120 minutes. (c) Diagram of the arrangement of the cuvette, magnet, and beam path for measurement of the residual dispersed Fe_3O_4-SiO_2-GNRs that are not pulled to the magnet. 81

Figure 5.4 Optical absorbance spectra of Fe_3O_4-SiO_2-GNRs during five rounds of purification through magnetic extraction, normalizes at 400 nm. Before acquiring each spectrum, the Fe_3O_4-SiO_2-GNRs were magnetically extracted using a permanent magnet. The supernatant was removed, and the sample was redispersed in a fixed volume of fresh hexanes and sonicated for 5 minutes. 83

Figure 5.5 (a) Optical absorbance spectra, normalized at 400 nm, and TEM (common scale bar) of (b) Fe_3O_4-SiO_2-GNRs in toluene and (c) PEG-Fe_3O_4-SiO_2-GNRs in water. 84

Figure 5.6 Unnormalized optical absorbance spectra of Fe_3O_4-SiO_2-GNRs during five rounds of purification through magnetic extraction. The normalized version of these spectra is provided in the main text, Figure 4. 97

Figure 5.7 Unnormalized optical absorbance spectra of Fe_3O_4-SiO_2-GNRs in toluene and PEG-Fe_3O_4-SiO_2-GNRs in water. The normalized version of these spectra is provided in the main text, Figure 5. 97

Figure 6.1 SEM images of amorphous TiO_2 nanofibers on a Si wafer (a) after electrospinning and (b) after heating to 450 °C in air for 2 hours. Insets show the sample samples at higher magnification. 105

Figure 6.2 Histograms of the diameter of TiO_2 fibers before and after heating to 450 °C for two hours. For each sample, 200 fibers were measured. 106

Figure 6.3 XRD of electrospun TiO_2 fibers on a Si wafer while heating to 900 °C at a rate of 1 °C / min. Diffractograms collected continuously at a rate of 1 measurement every ~15 minutes. Diffractograms were collected for 2θ values from 20° to 45° with a step of 0.026°. (a) All measurements from 0 to 900 ° (b) measurements from 774 °C to 900 °C and 20 ° to 40 ° to highlight peaks forming at higher temperatures. 109

Figure 7.1 SEM image of direct electrospun SiO_2 nanofibers with incorporated SiO_2-GNRs (a) before heat treatment and (b) after heating to 900 °C for three hours. Insets show the samples at higher magnification. 121

Figure 7.2 Histogram of the diameter of SiO_2 nanofibers before and after heating to 900 °C for three hours. For each sample, 200 fibers were measured. 122

Figure 7.3 TEM of (a) SiO_2-GNRs and electrospun composite SiO_2 nanofibers (b) before heat treatment and after heating for 3 hours at (c) 400 °C, (d) 500 °C, (e) 600 °C, (f) 700 °C, (g) 800 °C, and (h) 900 °C. 124

Figure 8.1 (a) TEM of AuNS with an inset of their optical absorbance spectrum, (b) SEM of aligned fibers, (c) TEM of AuNS aligned in a PEO fiber, and (d) STEM of AuNS aligned in fibers. 128

Figure 8.2 (a) Zeolite nanoplatelets and (b) SiO_2-zeolite nanoplatelets. 129

Figure 8.3 STEM of electrospun PEO fibers containing aligned QDNRs and low aspect ratio GNRs. 130

Figure 8.4 Optical absorbance spectra of low-aspect ratio GNRs and optical emission spectra of QDNRs, highlighting their spectral overlap. 131

Figure A.1 Examples of absorbance spectra from primary and secondary growth of GNRs synthesized using different lots of CTAB using 1x$AgNO_3$. Lot B could potentially produce rods with a longitudinal LSPR at 800 nm. 141

Figure A2 Optical absorbance spectra of the primary growth of GNRs produced using different amounts of Ag. 141

CHAPTER 1. Noble Metal Nanoparticles

Noble metal nanoparticles (NPs) are defined as gold, silver, palladium, and platinum particles with diameters below 100 nm. In this size range, these metals display properties distinct from their bulk counterparts. Amongst these properties, they exhibit shape-dependent optical absorbance, light scattering, new catalytic properties, and photothermal heating.[1-3] As a result, NPs are finding applications in many fields, including electronics, photovoltaics, sensors, and a variety of biomedical applications, such as drug delivery, photothermal therapy, and multimodal imaging.[4]

1.1 Development of Noble Metal Nanoparticle Synthesis

Historians have found evidence of noble metal NPs in stained glass from as early as the 4th century BC. The most notable example is the Lycurgus Cup (Figure 1),[5] an example of ruby glass that exemplifies ancient use of noble metal NPs. The Lycurgus cup contains small quantities of a gold-silver alloy NPs that result in unique optical properties. Figure 1 shows the difference in the way light interacts with the glass, when it scatters and transmits light. Up to and through the 19th century, colloidal gold NPs, also called gold sols, were investigated for applications in medicine, art, and alchemy, but the turning point for NP research was work done by Michael Faraday in the 1850s.[6] Faraday developed a method for synthesizing stable colloidal gold NPs by reducing gold chloride with phosphorus, and he studied their optical properties, deducing the presence of gold particles in his solution.[7]

Work on noble metal NPs continued through the 19th and early 20th centuries, with major contributions from Zsigmondy, Svedberg, Mie, and Gans. Zsigmondy developed an ultra-microscope to image the light scattered by NPs, a technique now known as dark-field microscopy.[8] Svedberg, in his research on colloids and proteins, developed the method of ultracentrifugation to isolate colloidal NPs and investigated their size-dependent properties during sedimentation.[6] Mie and Gans developed mathematical models to explain the way spherical gold NPs absorb and scatter light, and Gans expanded the model to include ellipsoidal NPs.[8]

Figure 1.1 The Lycurgus Cup, an example of noble metal NPs embedded in glass, made in the 4th century BC. (Left) Cup, when illuminated from outside, scatters light. (Middle) Cup, when illuminated from inside, absorbs light. (Right) TEM micrograph of AgAu NPs present in cup.[5]

1.2 Turkevich Method

One of the simplest and most popular method of synthesizing gold NPs was developed by Turkevich[9] and Frens[10] in the mid 20th century. Their approach to making gold

NPs produced uniform and monodisperse NPs with a high level of control over size. In this method, now known as the Turkevich method, an aqueous solution of gold chloroaurate ($HAuCl_4$) is heated to 100 °C. A solution of citric acid is added with rapid stirring, which reduces Au^{3+} to Au^0. Reduction with citric acid produces a high concentration of Au^0. Within minutes, spherical gold NPs nucleate and then grow, reaching final diameters of 10-20 nm (Figure 1.2) The molar ratio of citric acid to gold gives control over the size of the NPs, where increasing this ratio results in smaller particles.

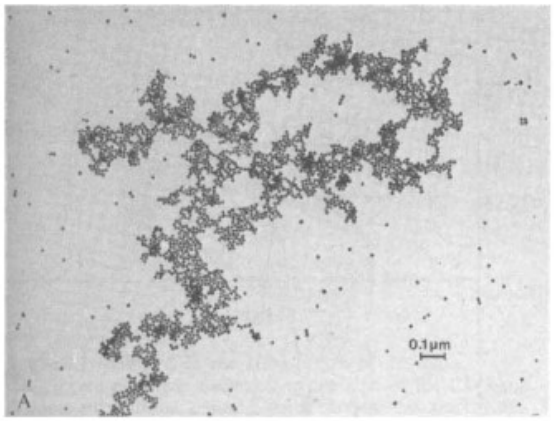

Figure 1.2 16-nm citrate stabilized gold NPs, published by Frens in 1973.[10]

1.3 Optical Properties of Gold Nanoparticles

Noble metal NPs have novel optical properties. Of particular interest is the localized surface plasmon resonance (LSPR). The LSPR is a shape- and composition-dependent property of noble metal NPs, which is a direct result of the delocalized nature of metallic electrons. The valence electrons in bulk gold are delocalized, causing its electrical and

thermal conductivity, as well as its optical properties. When bulk gold is shrunk to 100 nm, the "delocalized" conduction band electrons are now contained in a 100 nm sphere. It is the confinement of these electrons that produces the LSPR of noble metal NPs.[11]

The LSPR occurs when light, an oscillating electromagnetic wave, comes into contact with a metal NP. The electromagnetic wave causes the electrons on the surface the NP to oscillate, as well. The electrons on the surface of the NP shifted toward one side, which is balanced by a lower electron density on the other side of the NP (Figure 1.3). This produces a temporary positive and negative end, or dipole to form on the surface of the NP. The NP then produces a restoring force. The LSPR depends on four factors, the density of electrons, the effective electron mass, and the shape, and size of the NP.[12]

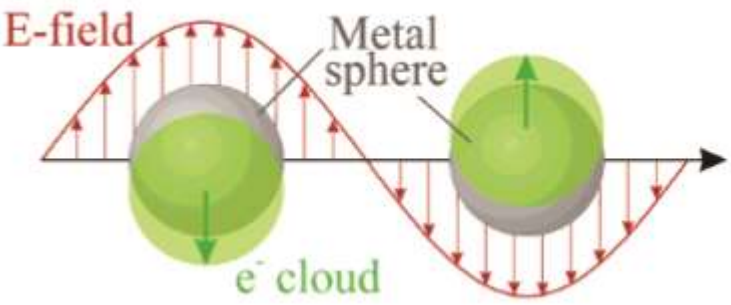

Figure 1.3 A diagram representing the collective oscillation of delocalized electrons in response to an electromagnetic field.[12]

1.3.1 Composition

The LSPR of the NP strongly depends on the composition. In the case of gold NPs, the LSPR is a single peak at 520 nm, producing a vibrant red color. For silver NPs, the LSPR resonance is at 400 nm, appearing yellow, and in platinum, the LSPR is it at 215 nm, ultraviolet light. The dependence of the LSPR on the composition of the NPs derives from the dielectric function of the NPs, the density of electric charges, and the effective electron mass.

Different elements have distinct absorption spectra, and as might be expected, when multiple elements are combined, the optical properties vary accordingly. As an example, alloys of gold and silver exhibit a single peak, between the LSPR of gold and silver.[13-15] The wavelength of the LSPR has a linear dependence on the molar composition of the NP. The LSPR of a NP containing 90% silver and 10% gold will have a LSPR much closer 400 nm, as opposed to an alloy containing 90% gold, which would have a LSPR closer to the 520 nm, because of the influence of gold. The explanation for the relationship is somewhat more complicated than combining the dielectrics or other parameters unique to each material. The dielectric of an alloy of two elements is not simply a combination of components, but a unique dielectric that needs to be determined.[16] Although this complexity exists, the LSPR wavelength nevertheless depends linearly on the mole fraction.[16]

The effects of elemental distribution in bimetallic NPs highlight the connections among the composition, structure, and optical properties. The previous discussion considered

alloy NPs, where two elements are homogenously mixed. In a core/shell morphology, one element is at the center of the NP, and the second element fully encapsulates it. In the case of a NP with a gold core and a silver center, the absorption spectrum blue shifts and broadens, but not to the degree expected when comparing to the equivalent alloy.[14,17,18] In some cases, two distinct peaks appear, depending on the thickness of the shell in addition to the red- or blueshift of the LSPR.[19] Variation among the results can likely be attributed to alloying at the interface of the two elements.[18] If the boundary was more distinct, then two absorption peaks would be observed instead of one.[18]

1.3.2 Size

The size of spherical NPs has a minor impact on the LSPR. According to Mie theory, the radius of the NP does have a role in determining the wavelength of the LSPR. As a particle increases in size, the LSPR will increase in intensity. To a lesser extent, the size also impacts the wavelength of the LSPR. As the size of the NP increases, the position of the LSPR redshifts.[20] One cause of this phenomenon is the size dependence of the dielectric function for smaller sizes. As the size of the NP decreases, it becomes smaller than the mean free path of conduction electrons within the NPs. Above diameters of 25 nm, a much stronger redshift can be attributed to more complex quadrupole and octopole vibrational modes contributing to the absorption spectrum.[21]

1.3.3 Shape

The shape of a metal NP also directly impacts its LSPR wavelength. Gold NPs shaped like spheres, rods, cubes, triangular prisms, and stars all have different absorbance spectra, despite having the same elemental composition. Gold nanorods are one of the simpler and more commonly studied anisotropic NPs, and will be discussed in more detail in Chapter 2, whose shape-dependent optical properties are briefly reviewed here. Gold nanorods possess two LSPRs, a transverse LSPR that absorbs at ~520 nm, and a longitudinal LSPR absorbs in the red and near-infrared spectra. The two surface LSPR are directly influenced by the geometry of the NPs. The transverse LSPR occurs when electromagnetic radiation drives oscillations of electrons along the length of the nanorod, and the longitudinal LSPR occurs when oscillations of the electrons are driven along the width of the nanorod. The exact wavelength of the longitudinal LSPR does not depend on the length of the nanorod, but rather on the ratio of the length to diameter of the nanorod. A nanorod with an aspect ratio of 2:1 will absorb at ~600 nm, an aspect ratio of 4:1 will absorb at 800 nm, and higher aspect ratios will continue to push the LSPR further into the near infrared. It should also be noted that, although it is quite minor, the transverse LSPR blueshifts slightly as the aspect ratio increases. For instance, a 4:1 ratio will have a transverse LSPR at 515 nm, while a gold nanorod with an aspect ratio of 2:1 will have a transverse LSPR closer to 520 nm.[22,23]

The impact of shape on the absorption spectra of more complex noble metal NP shapes can be understood as an extension of the properties of gold nanorods. As a slightly more complex example compared to a nanorod, an oblate ellipsoid has three LSPRs, one

longitudinal mode and two transverse modes, corresponding to the length and width of the oblate ellipsoid.[24] A triangular plate has a four peaks corresponding to in- and out-of-plane dipole and in- and out-of-plane quadrupole modes.[25] The LSPR of cubes and icosohedra are even more complex, with 6 or more modes (Figure 1.4).[26] Gold nanostars or nanourchins possess LSPRs corresponding to each branch of the star. Because of the large distribution of lengths and widths in nanostars multiple LSPRs overlap. Combining multiple absorption bands into an arch spanning 600-900 nm and a single 515 nm peak that the corresponds to the tip of the star.[27,28]

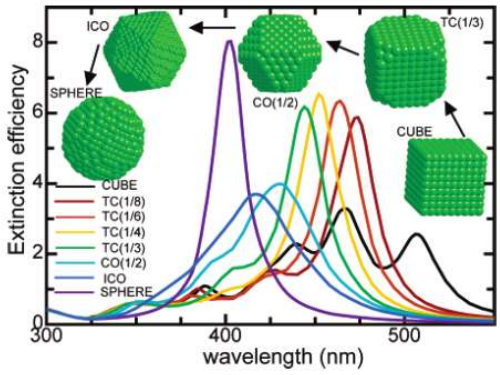

Figure 1.4 Calculated change in the extinction efficiency of a silver NP as it transitions from a cube to an icosahedron to a sphere.[26]

1.3.4 Dielectric

The dielectric of the surrounding medium can have a strong effect on the absorption spectrum of noble metal NPs. Increasing the dielectric of the surrounding medium has a positive linear effect on the wavelength of the LSPR.[12] This implies that transferring the same NP into different solvents will causing changes in the LSPR, even if there is no change

in morphology or agglomeration.[26] This also means that the LSPR shifts when adding a coating to a NP. As an example, silica has a higher dielectric constant than many solvents, and by introducing a layer of silica onto a NP, the LSPR can be redshifted.[29,30] The redshift in absorption occurs at shorter shell thicknesses, but as the shell thickness increases, scattering in the shell because a bigger factor, causing the LSPR to blueshift slightly.[30]

1.4 Electrostatic Stabilization

Because many of the properties of noble metal NPs directly result from confining electrons within the volume of the NP, it is important that they remain distinct and separated. This can be challenging, because the morphology of NP is much less thermodynamically favored than the bulk metal. Within each NP, there are powerful attractive van der Waals forces that if two particles were to come close enough together, they would fuse into each other, a process called coalescence. Although these van der Waals forces are strong, this is a rather short-range force, and Brownian forces determine the motion of NPs, except at short interparticle distances. To produce and maintain discrete NPs, repulsive interparticle forces are needed, especially at short interparticle distances.[31] There are many ways to stabilize NPs; electrostatic stabilization is discussed below, and a more comprehensive discussion of NP stabilization can be found in Chapter 4.

In electrostatic stabilization, positive or negative charges on the surface of the NP provide net repulsive Coulombic forces between NPs, which prevent agglomeration. Visualizing NPs as being studded with positive or negative charges on their surfaces can

often provide a useful understanding of how electrostatic stabilization occurs, although the reality is that the charges at the surface of NP is more complicated. As opposed to be being a simple corona of negative charge, charges in solution counterbalance the surface charges, forming a bilayer structure. This electrical double layer is best understood using the Stern-Gouy-Chapman (SGC) Model. The SGC model can be broken down into four parts, the charged surface, the inner and outer planes of the Helmholtz layer, and the diffuse layer. The charged surface is the source of either positive or negative electrostatic charge. The Helmholtz layer is a compact layer of solvent ions with an opposite charge to the charged surface that balances out the charged surface. The inner and outer planes of the Helmoltz layers (IHP and OHP) are considered to be fixed to the charged surface and not impacted by thermal motion. The IHP consists of a uniform layer of ions and solvent molecules that are either directly bound or adsorbed onto the charged NP surface. The OHP follows directly after the IHP and consists of fully solvated ions that are bound to the IHP. The diffuse layer contains more solvated ions oppositely charged to the OHP. This layer is much more diffuse than the OHP and is subject to thermal motion, and as a result, is much more dynamic than the Helmholtz layer.[32]

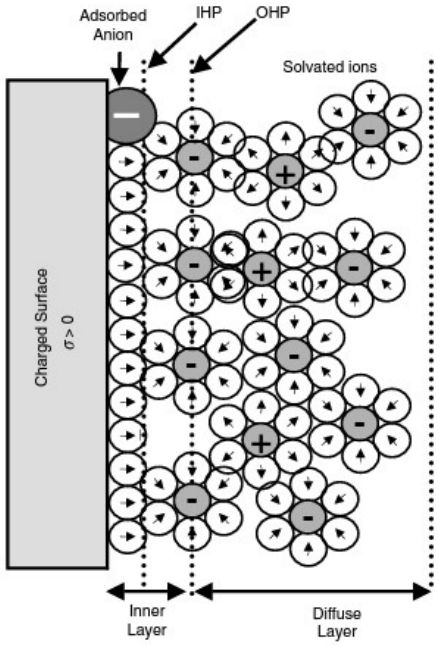

Figure 1.5 Diagram of the Stern-Guoy-Chapman model of the electrostatic bilayer.[32]

The surface potential decreases linearly with distance from the charged surface in the IHP and OHP, although the decrease is more pronounced in the IHP. The surface potential decreases exponentially at the diffuse layer. The diffuse layer contains a lower concentration of ions, compared the Helmholtz layer, but the concentration of ions in this layer depends on the overall concentration of electrolyte in solution. A high concentration of electrolytes improves the ability of the diffuse layer to counterbalance the charges in the Helmholtz layer, increasing the rate at which the surface potential decreases (Figure 1.6). If enough salt is added to the solution, it can completely screen the surface repulsion, and agglomeration can occur.[31]

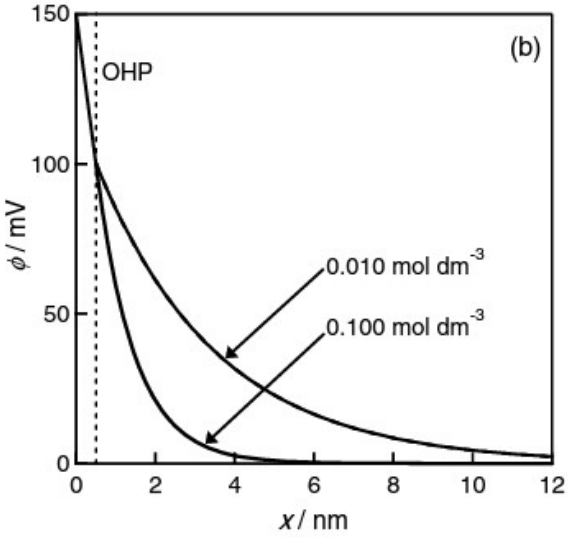

Figure 1.6 Plot of the surface potential from the SGC model as a function of distance from the charged surface at two electrolyte concentrations.[32]

1.5 References

(1) El-Sayed, M. A. Some Interesting Properties of Metals Confined in Time and Nanometer Space of Different Shapes. *Accounts of Chemical Research* **2001**, *34*, 257-264.

(2) Yeh, Y.-C.; Creran, B.; Rotello, V. M. Gold nanoparticles: preparation, properties, and applications in bionanotechnology. *Nanoscale* **2012**, *4*, 1871-1880.

(3) Natsuki, J.; Natsuki, T.; Hashimoto, Y. A Review of Silver Nanoparticles: Synthesis Methods Properties and Applications. *International Journal of Materials Science and Applications* **2015**, *4*, 325-332.

(4) Sreeprasad, T. S.; Pradeep, T. Noble Metal Nanoparticles. In *Springer Handbook of Nanomaterials*, Vajtai, R., Ed. Springer Berlin Heidelberg: Berlin, Heidelberg, 2013; pp 303-388.

(5) Freestone, I.; Meeks, N.; Sax, M.; Higgitt, C. The Lycurgus Cup — A Roman nanotechnology. *Gold Bulletin* **2007**, *40*, 270-277.

(6) Sharma, V.; Park, K.; Srinivasarao, M. Colloidal dispersion of gold nanorods: Historical background, optical properties, seed-mediated synthesis, shape separation and self-assembly. *Materials Science and Engineering: R: Reports* **2009**, *65*, 1-38.

(7) Faraday, M. The Bakerian Lecture: Experimental Relations of Gold (and Other Metals) to Light. *Philosophical Transactions of the Royal Society of London* **1857**, *147*, 145-181.

(8) Polte, J. Fundamental growth principles of colloidal metal nanoparticles - a new perspective. *CrystEngComm* **2015**, *17*, 6809-6830.

(9) Turkevich, J. Colloidal gold. Part I. *Gold Bulletin* **1985**, *18*, 86-91.

(10) Frens, G. Controlled Nucleation for the Regulation of the Particle Size in Monodisperse Gold Suspension. *Nature Physical Science* **1973**, *241*, 20-22.

(11) Sajanlal, P. R.; Sreeprasad, T. S.; Samal, A. K.; Pradeep, T. Anisotropic nanomaterials: structure, growth, assembly, and functions. *Nano Reviews* **2011**, *2*, 10.3402/nano.v2i0.5883.

(12) Kelly, K. L.; Coronado, E.; Zhao, L. L.; Schatz, G. C. The Optical Properties of Metal Nanoparticles: The Influence of Size, Shape, and Dielectric Environment. *The Journal of Physical Chemistry B* **2003**, *107*, 668-677.

(13) Al-Azawi, M. A.; Bidin, N.; Bououdina, M.; Mohammad, S. M. Preparation of gold and gold–silver alloy nanoparticles for enhancement of plasmonic dye-sensitized solar cells performance. *Solar Energy* **2016**, *126*, 93-104.

(14) Shore, M. S.; Wang, J.; Johnston-Peck, A. C.; Oldenburg, A. L.; Tracy, J. B. Synthesis of Au(Core)/Ag(Shell) Nanoparticles and their Conversion to AuAg Alloy Nanoparticles. *Small* **2011**, *7*, 230-234.

(15) Wilcoxon, J. Optical Absorption Properties of Dispersed Gold and Silver Alloy Nanoparticles. *The Journal of Physical Chemistry B* **2009**, *113*, 2647-2656.

(16) Link, S.; Wang, Z. L.; El-Sayed, M. A. Alloy Formation of Gold−Silver Nanoparticles and the Dependence of the Plasmon Absorption on Their Composition. *The Journal of Physical Chemistry B* **1999**, *103*, 3529-3533.

(17) Han, H.; Fang, Y.; Li, Z.; Xu, H. Tunable surface plasma resonance frequency in Ag core/Au shell nanoparticles system prepared by laser ablation. *Applied Physics Letters* **2008**, *92*, 023116.

(18) Mulvaney, P.; Giersig, M.; Henglein, A. Electrochemistry of multilayer colloids: preparation and absorption spectrum of gold-coated silver particles. *The Journal of Physical Chemistry* **1993**, *97*, 7061-7064.

(19) Lu, L.; Burkey, G.; Halaciuga, I.; Goia, D. V. Core–shell gold/silver nanoparticles: Synthesis and optical properties. *J Colloid Interface Sci* **2013**, *392*, 90-95.

(20) Logunov, S. L.; Ahmadi, T. S.; El-Sayed, M. A.; Khoury, J. T.; Whetten, R. L. Electron Dynamics of Passivated Gold Nanocrystals Probed by Subpicosecond Transient Absorption Spectroscopy. *The Journal of Physical Chemistry B* **1997**, *101*, 3713-3719.

(21) Link, S.; El-Sayed, M. A. Size and Temperature Dependence of the Plasmon Absorption of Colloidal Gold Nanoparticles. *The Journal of Physical Chemistry B* **1999**, *103*, 4212-4217.

(22) Chen, H.; Shao, L.; Li, Q.; Wang, J. Gold nanorods and their plasmonic properties. *Chemical Society Reviews* **2013**, *42*, 2679-2724.

(23) Lohse, S. E.; Murphy, C. J. The Quest for Shape Control: A History of Gold Nanorod Synthesis. *Chemistry of Materials* **2013**, *25*, 1250-1261.

(24) Fan, H.; Lopez, G. P.; Brinker, C. J.; Lu, Y. Prototyping of patterned functional nanostructures. Google Patents: 2002.

(25) Sau, T. K.; Rogach, A. L.; Jäckel, F.; Klar, T. A.; Feldmann, J. Properties and Applications of Colloidal Nonspherical Noble Metal Nanoparticles. *Adv Mater* **2010**, *22*, 1805-1825.

(26) Noguez, C. Surface Plasmons on Metal Nanoparticles: The Influence of Shape and Physical Environment. *The Journal of Physical Chemistry C* **2007**, *111*, 3806-3819.

(27) van der Zande, B. M. I.; Böhmer, M. R.; Fokkink, L. G. J.; Schönenberger, C. Aqueous Gold Sols of Rod-Shaped Particles. *The Journal of Physical Chemistry B* **1997**, *101*, 852-854.

(28) Yu; Chang, S.-S.; Lee, C.-L.; Wang, C. R. C. Gold Nanorods: Electrochemical Synthesis and Optical Properties. *The Journal of Physical Chemistry B* **1997**, *101*, 6661-6664.

(29) Vanderkooy, A.; Chen, Y.; Gonzaga, F.; Brook, M. A. Silica Shell/Gold Core Nanoparticles: Correlating Shell Thickness with the Plasmonic Red Shift upon Aggregation. *ACS Applied Materials & Interfaces* **2011**, *3*, 3942-3947.

(30) Park, H. J.; Ah, C. S.; Kim, W.-J.; Choi, I. S.; Lee, K.-P.; Yun, W. S. Temperature-induced control of aspect ratio of gold nanorods. *Journal of Vacuum Science & Technology A: Vacuum, Surfaces, and Films* **2006**, *24*, 1323-1326.

(31) Horinek, D. DLVO Theory. In *Encyclopedia of Applied Electrochemistry*, Kreysa, G.; Ota, K.-i.; Savinell, R. F., Eds. Springer New York: New York, NY, 2014; pp 343-346.

(32) Cosgrove, T. *Colloid Science : Principles, Methods and Applications (2)*. Wiley-Blackwell: Hoboken, GB, 2010.

CHAPTER 2. Gold Nanorods

Research on nanoparticles (NPs) has vastly expanded since the work and time of Faraday. Gold nanorods (GNRs) are long and narrow gold NPs with cylindrical shapes that have garnered special attention because of their novel optical properties. Interest in GNRs stems from the intense longitudinal surface plasmon resonance (LSPR) that can be tuned to absorb at specific wavelengths ranging from green to near infrared by controlling the aspect ratio (length / width) of GNRs.[1,2]

2.1 Optical Properties

As has been discussed in Chapter 1, GNRs possess two LSPRs. The first LSPR, the transverse LSPR, corresponds to oscillation along the diameter of the GNR, and absorbs at 515-520 nm. The second LSPR, the longitudinal surface plasmon, corresponds to oscillation along the length of the GNR, and absorbs light at longer wavelengths. The longitudinal LSPR has a linear relationship with the aspect ratio of the GNR, allowing for the longitudinal LSPR to be tuned by varying the aspect ratio of the GNRs. It should also be noted that there is a slight blueshift in the transverse LSPR as the aspect ratio increases.[3]

2.1.1 Polarization Dependence

Since the LSPR depends on the axis of the GNR along which the electrons oscillate, GNRs have polarization-dependent optical properties. This phenomenon is not noticeable when GNRs are dispersed in solvents, because the GNRs are randomly oriented and thus all

orientations are sampled. When GNRs are aligned in a thin film[2], fibers,[4] or on substrate,[5] polarization-dependent properties can be measured. If the source in a spectrophotometer is polarized, absorption spectra can be controlled such that if the GNRs are oriented parallel to the polarization direction, the electric field vector, then only the longitudinal LSPR is visible, and if the light polarized perpendicular to the long axes of the GNRs, then only the transverse LSPR is observed. When light is polarized at in intermediate angle, the absorption spectrum will have contributions from both the longitudinal and transverse modes (Figure 2.1).

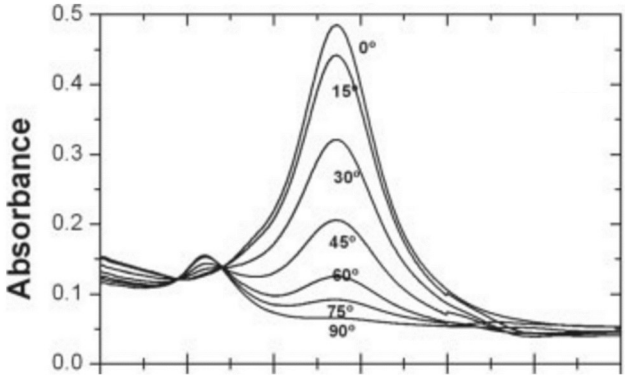

Figure 2.1 Absorption spectra of GNRs aligned in a poly(vinyl alcohol) thin film when excited with polarized light. 0° and 90° correspond to light parallel and perpendicular to the long axis of the GNRs, respectively.[6]

2.1.2 Dielectric

Just as the LSPR of spherical NPs is influenced by the dielectric environment, the optical properties of GNRs are also sensitive to the dielectric environment. The most notable difference between the spherical NPs and GNRs is that the dielectric has a much more

dramatic impact on the longitudinal LSPR of GNRs. Altering the refractive index of the solvent can change the wavelength of the longitudinal LSPR resonance by as much as 100 nm (Figure 2.3).[2] Just as coatings on spherical Au NPs affect the dielectric environment and can cause shifting in the surface plasmon, coatings on GNRs can also cause shifts in the longitudinal LSPR. An overcoating of mesoporous silica can change the LSPR by as much as 60 nm, but the effect becomes less dramatic as the shell grows thicker because the change in dielectric environment is less dramatic[7] (Figure 2.2).

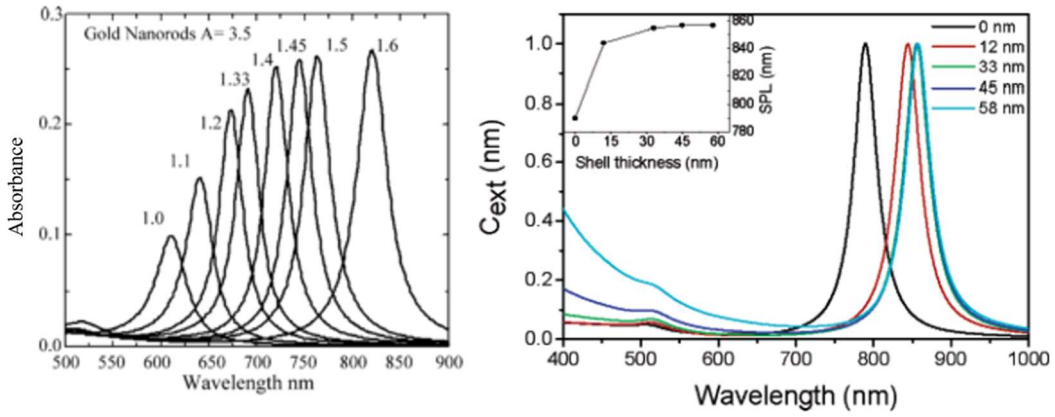

Figure 2.2 (Left) Simulations showing the impact of the dielectric on the medium surrounding GNRs with an aspect ratio of 3.5 on their surface plasmon resonance.[2] (Right) Simulations of extinction spectra of SiO_2-GNRs illustrating how the thickness of SiO_2 shells affects the LSPR.[7]

2.2 Gold Nanorod Synthesis

The first example of the synthesis of colloidal GNRs was the electrodeposition of gold in a porous aluminum oxide in 1997.[8] The pores served as a template for the rods, which were released be dissolving the alumina template and adding a surfactant to prevent agglomeration. Since then, several methods have been developed for producing GNRs, from solution-based methods using surfactants, lithography, and template-based methods where rods are formed by a mold. Each method has its advantages and disadvantages, but the method used in this research and further discussed is a cetyltrimethylammonium bromide (CTAB)-based, seed-mediated approach. Before discussing in detail the method used in this research, the development of the CTAB-based approach is briefly reviewed.

2.2.1 Development of CTAB-Coated Gold Nanorods

The first example of the CTAB-based synthesis of GNRs was an electrochemical approach from 1997.[9] In this method, a redox reaction was performed using a gold electrode in the presence of CTAB and other surfactants that form rod-shaped micelles. It was hypothesized that gold NPs would form within the micelles, templating a rod shape, while at the same time providing colloidal stability. Although the hypothesis was ultimately incorrect, CTAB was found to facilitate formation of rod-shaped gold NPs by more tightly binding onto certain facets of the gold crystal and thus preventing the deposition of gold onto those surfaces.[10]

The next major milestone in the synthesis of GNRs was the seed-based method by Jana, Gearheart, and Murphy.[11] This work started with the synthesis of CTAB-stabilized seeds using a powerful reducing agent. The seed-based method is useful because formation of nanorods is a kinetic process that requires careful control of parameters to achieve uniform size, but this careful control is the opposite of what is required for uniform seeds. By separating the nucleation and growth, sodium borohydride ($NaBH_4$), a powerful reducing agent can be used to form monodisperse seed crystals with diameters of 4-5 nm. The growth step uses ascorbic acid, a much milder reducing agent that requires the surface of the gold seed to completely reduce $HAuCl_4$, reducing the formation of byproducts. Jana also identified that silver ions can play a role in improving the yield and quality of the product.

The next major advancement in the development of the synthesis of GNRs was Nikoobakht and El Sayed's work.[12] This work identified the need to use CTAB as the stabilizing surfactant in the seed solution. In contrast Jana's seeds were citrate stabilized, and by using only one surfactant, Nikoobakht and El Sayed were able to reduce the number of byproducts and improve the GNR's monodispersity. The work also expanded the role of silver in the synthesis of GNRs, showing that varying the amount of Ag^+ in the growth controlled the aspect ratio of the nanorods. Using silver, nanorods with plasmon resonances of 600-1300 nm were achieved.

The work of Murray et al.[13] further improved the quality of the GNRs with aromatic additives, further improving the monodispersity and reducing the amount of CTAB required by half. By adding aromatic salts such as sodium salicylate into the CTAB solution, the

phenyl groups in these additives penetrated the hydrophobic part of the CTAB micelles, which alters the structure in which they pack on the GNRs. This work had the effect of increasing the yield of the GNR synthesis and drastically improved the monodispersity. A high level of monodispersity is critical for self-assembly and colloidal crystals. Although this work did not discover the importance of bromide ions in the GNR synthesis, it suggested a reason that a high concentration of CTAB was necessary in previous work was because of a need for a high concentration of bromide ions. By adding potassium bromide to increase the bromide concentration, a lower concentration of CTAB can be used.

2.3 Secondary Injection of Ascorbic Acid

The results reported in chapters 5 and 7 rely primarily on the synthesis developed by previous members of the Tracy group, published by Kozek et al[14] who were inspired by work published by Vigderman and Zubarev,[15] where it was discovered that increasing the amount of reducing agent in the synthesis, 100% of $HAuCl_4$ could be converted into GNRs. Kozek et al. found that a similar effect could be achieved by incorporating a continuous secondary injection of ascorbic acid into the GNR synthesis. The methods from the El Sayed group mentioned above involved two steps, making the seed then growing the rods.[12] The problem with this approach is that it utilizes only 30% of the gold in solution. This is inefficient, and the excess gold needs to be promptly removed at the end of the synthesis or else the nanorods will continue to change shape.

Performing a secondary injection of ascorbic acid reduces and deposits the remain Au onto the surface of the existing GNRs. This ascorbic acid addition step does not drive a secondary nucleation event. By controlling the rate of ascorbic acid injection, the deposition of gold can be controlled such that the aspect ratio can be maintained while the GNRs grow. Maintaining the same aspect ratio requires faster deposition on the ends of the GNRs than on the sides. By decreasing the injection rate of ascorbic acid, the rate of deposition of gold on the tips and sides becomes more equal, resulting in a decrease in the aspect ratio.

2.4 Factors Influencing the Synthesis of Gold Nanorods

A particularly useful aspect of many methods for synthesizing GNRs is that the shape of the GNRs can be controlled. By varying multiple parameters, the size and aspect ratio of GNRs can be controlled.

2.4.1 Silver Ions

Silver ions are a critical element in increasing the yield of GNRs, as was discussed in Section 2.2.1. Reduced silver deposits onto the sides of the GNRs, greatly increasing the yield of GNRs.[12] In addition to improving yield, varying the concentration of silver ions in solution can affect the aspect ratio of the GNRs. Increasing the concentration of silver in the growth solution has the effect of redshifting the surface plasmon. The plasmon can be shifted 50 nm from the initial plasmon by changing the silver concentration.[12,16] There is a limit to this lever, where decreasing or increasing the silver concentration too much will decrease the yield of nanorods and increasing the yield of spherical shapes.

2.4.2 Bromide Ions

Bromide ions are also important in the synthesis of GNRs. The bromide ion is an important part of the quaternary amine complex that forms on the GNRs surface. If bromide is excluded from the synthesis, for example, replacing CTAB with cetyltrimethylammonium chloride (CTAC) results in no GNRs.[17] Adding too much additional bromide ion to the synthesis results in blueshifting and eventually, no nanorod formation. At a too high of a concentration, bromide will deposit onto the ends of the GNRs, inhibiting deposition of Au.[18] Adding bromide to the synthesis has the effect of reducing the negative impacts of impurities in CTAB, increasing the reproducibility the synthesis.[14] Batch-to-batch issues will be discussed more in Section 2.6.

2.4.3 Secondary Injection Rate

The rate of the secondary injection of ascorbic acid is a useful lever for fine tuning the optical absorbance spectra after completing primary growth. The secondary injection rate, discussed in Section 2.3, can be selected to maintain the aspect ratio of the GNRs from the primary growth. Decreasing the injection rate decreases the preference for the gold atoms to deposit onto the ends of the GNRs. At the slowest addition rate, lasting one day, the rate of growth on the tips and the sides of the GNRs will be equal. This results in an overall decrease in the aspect ratio of the GNRs and a decrease in their plasmon resonance wavelength.[14] By decreasing the injection rate, the plasmon resonance wavelength can be decreased by 100 nm. This can be used to produce GNRs with aspect ratios as low as 1.5:1 with a plasmon

resonance of 610 nm. Work on exploiting the injection rate and silver concentration to produce low-aspect-ratio, short wavelength GNRs can be found in Appendix 1.

2.4.4 Temperature

Temperature can be a complicated variable in the synthesis of GNRs. CTAB forms micelles only when the temperature is above 24.8 °C.[19] Therefore, the reaction mixture needs to kept above this temperature for the CTAB to form micelles. One the other hand, the synthesis of GNRs is a kinetically controlled processes. Raising the temperature increases the energy in the system, making it easier for gold to deposit on the sides, resulting in more a thermodynamically controlled process. Performing the synthesis at higher temperatures results in shorter aspect ratios and a broader size distribution.[20]

2.4.5 pH

pH can also play a role in the seed-mediated synthesis of GNRs. It has been shown that a higher (lower) pH increases (decreases) the aspect ratio of the GNRs.[21] The reducing agent used in the GNR synthesis, ascorbic acid, is a weak acid. As a result, altering the pH of the growth solution changes the concentration of ascorbic acid, its monoanion, and its dianion. The reduction potentials of the three species are different, resulting in a change in the rate of the growth of GNR.

2.4.6 Seed Concentration

The concentration of the seed NPs can also affect the reaction products. Injecting less seed into the growth solution results in a lower yield of larger GNRs with shorter aspect-ratio, blueshifting the plasmon resonance. Injecting more seed will increase the aspect ratio and redshift the plasmon resonance, but there is a limit to how much increasing the seed concentration can impact the aspect ratio.[15]

2.5 Stabilization

As has been discussed already, CTAB is the surfactant that stabilizes the GNRs. The initial rationale for selecting CTAB was that it forms rod-shaped micelles under certain conditions. More recent research suggests that the mechanism behind the formation of nanorods is more complicated, which is discussed below after additional introduction to the structure and properties of CTAB.

2.5.1 CTAB

CTAB is a cationic salt consisting of a 16-carbon alkyl chain at one end and a quaternary ammonium group on the other end, with a bromide counterion. Depending on the concentration of CTAB, temperature, and the use of other additives, aqueous CTAB can assemble into structures ranging from spheres, worm-like rods, liquid crystal, or lamella.[22-24] A phase diagram of these structures as they depend on temperature and concentration is presented in Figure 2.3.

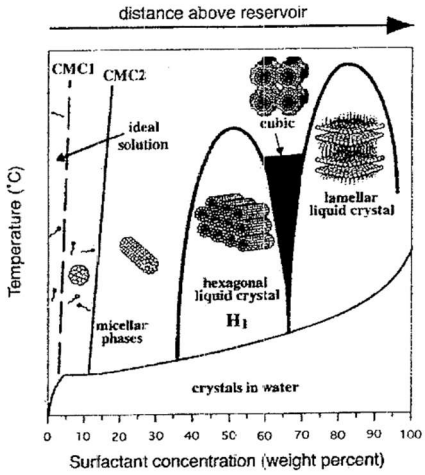

Figure 2.3 Phase diagram of the structure of aqueous CTAB as a function of temperature and concentration.[25]

The key structure in the synthesis of GNRs is the micellular structure, where the CTAB forms a bilayer with the hydrophobic alkyl chains inside and quaternary ammoniums on the outside, exposed to water.[26,27](Figure 2.4). The ammonium groups together with the bromide ions are capable of coordinating with the gold atoms along facets of the gold crystal, but they bind more effectively along (100) facets than (111) facets.[28] This means that the micelle packs more densely on (100) planes and less densely on (111) planes. Consequently, the more densely packed CTAB reduces the rate of Au deposition on the (100) plane driving the gold to form a rod shape.[28,29] The end result is GNRs coated with bilayers of CTAB. CTAB provides a combination of electrostatic stabilization through the exposed quaternary ammonium groups and a steric repulsion from the layer of alkyl chains.[30,31]

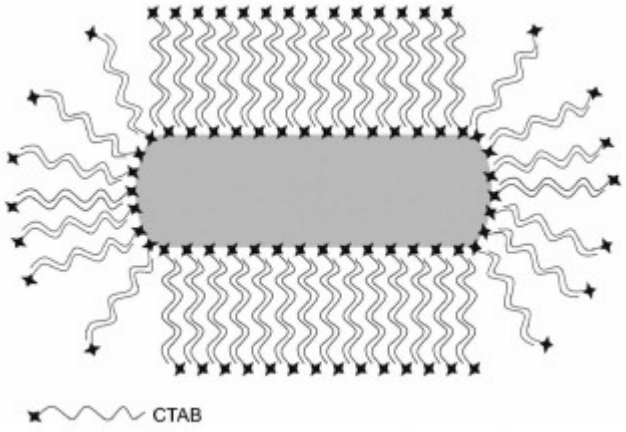

Figure 2.4 Depiction of the bilayer structure of CTAB-stabilized GNRs.[27]

CTAB coatings result in a highly stable dispersion of GNRs, provided some excess CTAB is added to prevent dissociation from the surfaces of the GNRs.[27] For GNRs to remain well dispersed, the CTAB concentration must be high enough to allow CTAB to form micelles. The lowest concentration of CTAB, under which micelles still form is 1 mM.[32] Below this concentration, GNRs are no longer stable. GNRs are also more resistant to agglomeration when salts are added in comparison with citrate-stabilized NPs. GNRs also need to remain in an aqueous environment. They can remain suspended when a small amount of alcohol is added, but larger amounts will strip CTAB from the surfaces of the GNRs, causing agglomeration.

2.5.2 Polyethylene Glycol

Although CTAB can be used to stabilize GNRs indefinitely, CTAB is a problem for biomedical applications because it is not biocompatible.[33-35] Dispersions of GNRs containing

CTAB concentrations exceeding 10 mM CTAB have been shown to be cytotoxic. Below 10 mM, the CTAB is bound to the GNRs and does not show the same level of cytotoxicity, but bound CTAB will eventually dissociated from the GNRs and become cytotoxic.[33] To use GNRs in biomedical applications, CTAB needs to be removed and another material added to stabilize the product. A common approach is to replace CTAB with poly(ethylene glycol) (PEG).[35] PEG will not directly bind with gold, so PEG is thiolated on one end because of the strong binding of thiols to gold. When PEG-thiol is added to GNRs with a CTAB concentration of 1 mM or lower, the PEG-thiol can displace the CTAB.[36] The improved stability of PEGylated GNRs comes from hydrogen bonds in the ether groups with water and the steric stabilization of the polyether chain.[37] PEGylated GNRs are stable in many solvents, including ethanol, methanol, dimethyl formamide, tetrahydrofuran, and dichloromethane and can withstand high electrolyte environments, such as phosphate buffer.[38]

Displacing CTAB during functionalization with PEG-thiol can be challenging, however.[35,39] Recent work suggest that significant amounts of CTAB remain attached to GNRs after PEGylation.[40,41] The binding of CTAB to the GNR surface is sufficiently strong that even CTAB molecules attached to the initial seed remain attached to the GNRs, instead of diffusing into the solution overtime. The remaining CTAB is a two-fold problem, because it both interferes with PEGylation and is cytotoxic even at low concentrations. One study suggests the number of PEG chains grafted to GNRs is as low as two or three per GNR.[40] The PEGylation procedure described above is moderately effective at PEGylating GNRs, but

needs refinement. An improved procedure for functionalizing CTAB-stabilized GNRs with PEG-thiol is reported Appendix 2.

2.5.3 Silica

Another method for stabilizing GNRs is to deposit SiO_2 shells.[42-45] Overcoating GNRs with SiO_2 provides multiple benefits. First, SiO_2 is biocompatible,[46] and CTAB can be completely removed from GNRs. Second, SiO_2 improves the thermal stability of GNRs.[36,47] Third, overcoating GNRs with SiO_2 introduces surfaces that can be functionalized using silanes. Trialkoxysilanes, $(RO)_3SiR'$, where RO is an alkoxy group and R' can be one of many organic functional groups can be used to functionalize a silica surface with R'. This approach be used to coat a silica surface with a vast range of different functional groups that can be purchased or synthesized.[48-50]

SiO_2-overcoated GNRs are used in research presented in Chapters 5, 7, and 8. The method used to synthesize SiO_2-overcoated GNRs was developed by Wu and Tracy.[42] A detailed description of this synthesis is included in Chapter 5. Briefly, CTAB-stabilized GNRs are concentrated to 2.5 mM of CTAB and ~3.8 mg/mL of GNRs. CTAB serves as template for deposition of a mesoporous SiO_2 shell. The pH of the solution is brought to 10.4 to drive formation of NPs, and TEOS is continuously injected into the solution over a 5 minute period. Using this method, GNRs can be synthesized with a shell thickness of 3-20 nm. Improved control over the thickness of thin shells can be achieved by adding a PEG-

functionalized triethoxysilane. PEG-silane terminates growth of the SiO_2 shell and can be used to make a SiO_2 shells as thin as 2 nm.

2.6 Reproducibility Challenges

One of the most significant obstacles in the synthesis of CTAB-stabilized GNRs is inconsistencies in the purity of CTAB. A study of how the source of the CTAB affects the quality of the GNRs showed that many brands do not produce GNRs while others can, and within the brands that can produce nanorods, the morphology varied (Figure 2.5).[51] The greater challenge of working with CTAB is that variation among lots of the same brand and product of CTAB is enough to cause inconsistencies in the products. Lot-to-lot variation in the quality of CTAB results in variations in size, aspects ratios, yield, and undesirable biproducts. Research suggests that a major source of variation in the quality of GNRs is the presence of iodide impurities in the CTAB.[52,53] At low concentrations (μM range), iodide in the CTAB deposits on the (111) facet of the GNR, inhibiting CTAB from binding on that surface of the GNR, which allows gold to deposit on the ends.[54] A too high concentration of iodide results in the formation of nanoprisms because iodide covers the entire crystal, altering the reactivity of crystal facets.[54]

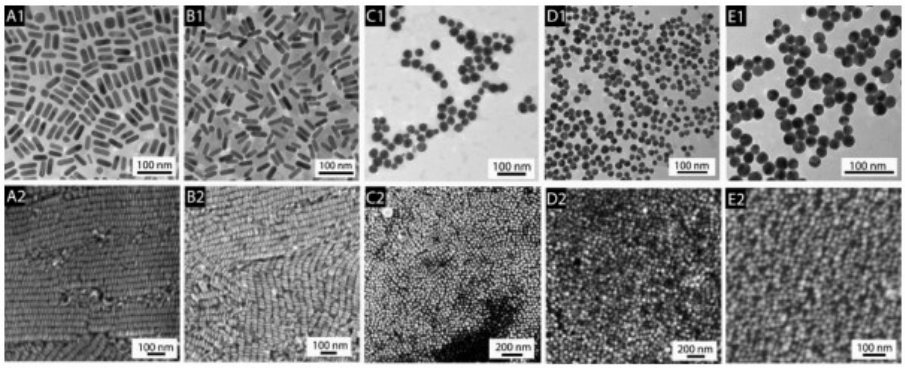

Figure 2.5 GNR synthesis performed using CTAB from (a) Fluka, (b) MP Biomedicals, (c) Acros, (d) Sigma, and (e) Aldrich. The top row (1) is TEM and the bottom row (2) is SEM.[51]

In practice, variations in the purity of CTAB mean that researchers cannot assume that a specific brand of product will produce the desired product. A protocol for identifying a batch of CTAB of sufficient quality is reported in Appendix 3. As a synopsis, identifying a batch of CTAB involves: (1) purchasing a small amount of CTAB, (2) synthesizing GNRs using the typical procedure, (3) examining the optical absorbance spectrum for signs of byproducts or low yield, and (4) adjusting the silver concentration to achieve the desired aspect ratio. If minor adjustments to the procedure will not provide a high yield of reasonably monodisperse GNRs, then another batch will be chosen for testing. With some patience, a good batch of CTAB can be found and stocked.

2.7 References

(1) Lohse, S. E.; Murphy, C. J. The Quest for Shape Control: A History of Gold Nanorod Synthesis. *Chemistry of Materials* **2013**, *25*, 1250-1261.

(2) Pérez-Juste, J.; Pastoriza-Santos, I.; Liz-Marzán, L. M.; Mulvaney, P. Gold nanorods: Synthesis, characterization and applications. *Coordination Chemistry Reviews* **2005**, *249*, 1870-1901.

(3) Link, S.; Mohamed, M. B.; El-Sayed, M. A. Simulation of the Optical Absorption Spectra of Gold Nanorods as a Function of Their Aspect Ratio and the Effect of the Medium Dielectric Constant. *The Journal of Physical Chemistry B* **1999**, *103*, 3073-3077.

(4) Roskov, K. E.; Kozek, K. A.; Wu, W.-C.; Chhetri, R. K.; Oldenburg, A. L.; Spontak, R. J.; Tracy, J. B. Long-Range Alignment of Gold Nanorods in Electrospun Polymer Nano/Microfibers. *Langmuir* **2011**, *27*, 13965-13969.

(5) Ahmed, W.; Kooij, E. S.; van Silfhout, A.; Poelsema, B. Quantitative Analysis of Gold Nanorod Alignment after Electric Field-Assisted Deposition. *Nano Lett* **2009**, *9*, 3786-3794.

(6) Pérez-Juste, J.; Rodríguez-González, B.; Mulvaney, P.; Liz-Marzán, L. M. Optical Control and Patterning of Gold-Nanorod–Poly(vinyl alcohol) Nanocomposite Films. *Advanced Functional Materials* **2005**, *15*, 1065-1071.

(7) Pastoriza-Santos, I.; Pérez-Juste, J.; Liz-Marzán, L. M. Silica-coating and hydrophobation of CTAB-stabilized gold nanorods. *Chemistry of Materials* **2006**, *18*, 2465-2467.

(8) van der Zande, B. M. I.; Böhmer, M. R.; Fokkink, L. G. J.; Schönenberger, C. Aqueous Gold Sols of Rod-Shaped Particles. *The Journal of Physical Chemistry B* **1997**, *101*, 852-854.

(9) Yu; Chang, S.-S.; Lee, C.-L.; Wang, C. R. C. Gold Nanorods: Electrochemical Synthesis and Optical Properties. *The Journal of Physical Chemistry B* **1997**, *101*, 6661-6664.

(10) Grochola, G.; Snook, I. K.; Russo, S. P. Computational modeling of nanorod growth. *The Journal of Chemical Physics* **2007**, *127*, 194707.

(11) Jana, N. R.; Gearheart, L.; Murphy, C. J. Seed-Mediated Growth Approach for Shape-Controlled Synthesis of Spheroidal and Rod-like Gold Nanoparticles Using a Surfactant Template. *Adv Mater* **2001**, *13*, 1389-1393.

(12) Nikoobakht, B.; El-Sayed, M. A. Preparation and Growth Mechanism of Gold Nanorods (NRs) Using Seed-Mediated Growth Method. *Chemistry of Materials* **2003**, *15*, 1957-1962.

(13) Ye, X.; Jin, L.; Caglayan, H.; Chen, J.; Xing, G.; Zheng, C.; Doan-Nguyen, V.; Kang, Y.; Engheta, N.; Kagan, C. R.; Murray, C. B. Improved Size-Tunable Synthesis of Monodisperse Gold Nanorods through the Use of Aromatic Additives. *ACS Nano* **2012**, *6*, 2804-2817.

(14) Kozek, K. A.; Kozek, K. M.; Wu, W.-C.; Mishra, S. R.; Tracy, J. B. Large-Scale Synthesis of Gold Nanorods through Continuous Secondary Growth. *Chemistry of Materials* **2013**, *25*, 4537-4544.

(15) Vigderman, L.; Zubarev, E. R. High-Yield Synthesis of Gold Nanorods with Longitudinal SPR Peak Greater than 1200 nm Using Hydroquinone as a Reducing Agent. *Chemistry of Materials* **2013**, *25*, 1450-1457.

(16) Sau, T. K.; Murphy, C. J. Seeded High Yield Synthesis of Short Au Nanorods in Aqueous Solution. *Langmuir* **2004**, *20*, 6414-6420.

(17) Murphy, C. J.; Sau, T. K.; Gole, A. M.; Orendorff, C. J.; Gao, J.; Gou, L.; Hunyadi, S. E.; Li, T. Anisotropic Metal Nanoparticles: Synthesis, Assembly, and Optical Applications. *Journal of Physical Chemistry B* **2005**, *109*, 13857-13870.

(18) Si, S.; Leduc, C.; Delville, M.-H.; Lounis, B. Short Gold Nanorod Growth Revisited: The Critical Role of the Bromide Counterion. *ChemPhysChem* **2012**, *13*, 193-202.

(19) Hirata, H.; Ohira, A.; Iimura, N. Measurements of the Krafft Point of Surfactant Molecular Complexes: Insights into the Intricacies of "Solubilization". *Langmuir* **1996**, *12*, 6044-6052.

(20) Scarabelli, L.; Sánchez-Iglesias, A.; Pérez-Juste, J.; Liz-Marzán, L. M. A "Tips and Tricks" Practical Guide to the Synthesis of Gold Nanorods. *The Journal of Physical Chemistry Letters* **2015**, *6*, 4270-4279.

(21) Busbee, B. D.; Obare, S. O.; Murphy, C. J. An Improved Synthesis of High-Aspect-Ratio Gold Nanorods. *Adv Mater* **2003**, *15*, 414-416.

(22) Lin, Z.; Cai, J. J.; Scriven, L. E.; Davis, H. T. Spherical-to-Wormlike Micelle Transition in CTAB Solutions. *The Journal of Physical Chemistry* **1994**, *98*, 5984-5993.

(23) Zhang, S.; Teng, H. N. Rheology and microstructure studies of SDS/CTAB/H2O system. *Colloid Journal* **2008**, *70*, 105-111.

(24) Mills, A. J.; Wilkie, J.; Britton, M. M. NMR and Molecular Dynamics Study of the Size, Shape, and Composition of Reverse Micelles in a Cetyltrimethylammonium Bromide (CTAB)/n-Hexane/Pentanol/Water Microemulsion. *The Journal of Physical Chemistry B* **2014**, *118*, 10767-10775.

(25) Fan, H.; Lopez, G. P.; Brinker, C. J.; Lu, Y. Prototyping of patterned functional nanostructures. Google Patents: 2002.

(26) Gao, J.; Bender, C. M.; Murphy, C. J. Dependence of the Gold Nanorod Aspect Ratio on the Nature of the Directing Surfactant in Aqueous Solution. *Langmuir* **2003**, *19*, 9065-9070.

(27) John, C. L.; Strating, S. L.; Shephard, K. A.; Zhao, J. X. Reproducibly synthesize gold nanorods and maintain their stability. *RSC Advances* **2013**, *3*, 10909-10918.

(28) Vivek, J. P.; Burgess, I. J. Quaternary Ammonium Bromide Surfactant Adsorption on Low-Index Surfaces of Gold. 1. Au(111). *Langmuir* **2012**, *28*, 5031-5039.

(29) Park, K.; Drummy, L. F.; Wadams, R. C.; Koerner, H.; Nepal, D.; Fabris, L.; Vaia, R. A. Growth Mechanism of Gold Nanorods. *Chemistry of Materials* **2013**, *25*, 555-563.

(30) Kraynov, A.; Müller, T. E. *Concepts for the Stabilization of Metal Nanoparticles in Ionic Liquids*. INTECH Open Access Publisher: 2011.

(31) Rosen, M. J. *Surfactants and Interfacial Phenomena*. Wiley-Interscience: Hoboken, N.J., 2004; Vol. 3rd ed.

(32) Kuperkar, K.; Abezgauz, L.; Prasad, K.; Bahadur, P. Formation and Growth of Micelles in Dilute Aqueous CTAB Solutions in the Presence of NaNO3 and NaClO3. *Journal of Surfactants and Detergents* **2010**, *13*, 293-303.

(33) Ray, P. C.; Yu, H.; Fu, P. P. Toxicity and Environmental Risks of Nanomaterials: Challenges and Future Needs. *Journal of environmental science and health. Part C, Environmental carcinogenesis & ecotoxicology reviews* **2009**, *27*, 1-35.

(34) Isomaa, B.; Reuter, J.; Djupsund, B. M. The subacute and chronic toxicity of cetyltrimethylammonium bromide (CTAB), a cationic surfactant, in the rat. *Archives of Toxicology* **1976**, *35*, 91-96.

(35) Alkilany, A. M.; Nagaria, P. K.; Hexel, C. R.; Shaw, T. J.; Murphy, C. J.; Wyatt, M. D. Cellular Uptake and Cytotoxicity of Gold Nanorods: Molecular Origin of Cytotoxicity and Surface Effects. *Small* **2009**, *5*, 701-708.

(36) Wu, W. C. Multifunctional Gold Nanorods: Large-Scale Synthesis, Overcoating, Alignment, and Applications. North Carolina State University, 2014.

(37) Mu, Q.; Hu, T.; Yu, J. Molecular Insight into the Steric Shielding Effect of PEG on the Conjugated Staphylokinase: Biochemical Characterization and Molecular Dynamics Simulation. *PLoS ONE* **2013**, *8*, e68559.

(38) Khlebtsov, B. N.; Panfilova, E. V.; Terentyuk, G. S.; Maksimova, I. L.; Ivanov, A. V.; Khlebtsov, N. G. Plasmonic Nanopowders for Photothermal Therapy of Tumors. *Langmuir* **2012**, *28*, 8994-9002.

(39) Liao, H.; Hafner, J. H. Gold Nanorod Bioconjugates. *Chemistry of Materials* **2005**, *17*, 4636-4641.

(40) Hore, M. J. A.; Ye, X.; Ford, J.; Gao, Y.; Fei, J.; Wu, Q.; Rowan, S. J.; Composto, R. J.; Murray, C. B.; Hammouda, B. Probing the Structure, Composition, and Spatial Distribution of Ligands on Gold Nanorods. *Nano Lett* **2015**, *15*, 5730-5738.

(41) Oyelere, A. K.; Chen, P. C.; Huang, X.; El-Sayed, I. H.; El-Sayed, M. A. Peptide-Conjugated Gold Nanorods for Nuclear Targeting. *Bioconjugate Chemistry* **2007**, *18*, 1490-1497.

(42) Wu, W.-C.; Tracy, J. B. Large-Scale Silica Overcoating of Gold Nanorods with Tunable Shell Thicknesses. *Chemistry of Materials* **2015**, *27*, 2888-2894.

(43) Obare, S. O.; Jana, N. R.; Murphy, C. J. Preparation of polystyrene- and silica-coated gold nanorods and their use as templates for the synthesis of hollow nanotubes. *Nano Lett* **2001**, *1*, 601-603.

(44) Abadeer, N. S.; Brennan, M. R.; Wilson, W. L.; Murphy, C. J. Distance and Plasmon Wavelength Dependent Fluorescence of Molecules Bound to Silica-Coated Gold Nanorods. *ACS Nano* **2014**, *8*, 8392-8406.

(45) Gorelikov, I.; Matsuura, N. Single-Step Coating of Mesoporous Silica on Cetyltrimethyl Ammonium Bromide-Capped Nanoparticles. *Nano Lett* **2008**, *8*, 369-373.

(46) Asefa, T.; Tao, Z. Biocompatibility of Mesoporous Silica Nanoparticles. *Chemical Research in Toxicology* **2012**, *25*, 2265-2284.

(47) Albrecht, W.; Deng, T.-S.; Goris, B.; van Huis, M. A.; Bals, S.; van Blaaderen, A. Single Particle Deformation and Analysis of Silica-Coated Gold Nanorods before and after Femtosecond Laser Pulse Excitation. *Nano Lett* **2016**, *16*, 1818-1825.

(48) Ramezani, M.; Vaezi, M. R.; Kazemzadeh, A. Preparation of silane-functionalized silica films via two-step dip coating sol–gel and evaluation of their superhydrophobic properties. *Applied Surface Science* **2014**, *317*, 147-153.

(49) Jesionowski, T.; Krysztafkiewicz, A. Preparation of the hydrophilic/hydrophobic silica particles. *Colloids and Surfaces A: Physicochemical and Engineering Aspects* **2002**, *207*, 49-58.

(50) Lee, C. H.; Park, S. H.; Chung, W.; Kim, J. Y.; Kim, S. H. Preparation and characterization of surface modified silica nanoparticles with organo-silane compounds. *Colloids and Surfaces A: Physicochemical and Engineering Aspects* **2011**, *384*, 318-322.

(51) Smith, D. K.; Korgel, B. A. The Importance of the CTAB Surfactant on the Colloidal Seed-Mediated Synthesis of Gold Nanorods. *Langmuir* **2008**, *24*, 644-649.

(52) Rayavarapu, R. G.; Ungureanu, C.; Krystek, P.; van Leeuwen, T. G.; Manohar, S. Iodide Impurities in Hexadecyltrimethylammonium Bromide (CTAB) Products: Lot−Lot Variations and Influence on Gold Nanorod Synthesis. *Langmuir* **2010**, *26*, 5050-5055.

(53) Smith, D. K.; Miller, N. R.; Korgel, B. A. Iodide in CTAB Prevents Gold Nanorod Formation. *Langmuir* **2009**, *25*, 9518-9524.

(54) Millstone, J. E.; Wei, W.; Jones, M. R.; Yoo, H.; Mirkin, C. A. Iodide Ions Control Seed-Mediated Growth of Anisotropic Gold Nanoparticles. *Nano Lett* **2008**, *8*, 2526-2529.

CHAPTER 3. Electrospinning Ceramic Fibers

Electrospinning is a simple method for producing polymer and ceramic fibers from a wide range of materials with diameters well into the nanoscale. The appeal of this method is its simplicity, the small diameters, and the high surface area. Numerous polymeric materials have been formed into fibers through electrospinning for applications, such as catalysis, sensing, electronics, tissue scaffolding, and filtration.[1,2] This chapter reviews the basics of electrospinning, with a primary focus on ceramic fibers and ceramic fiber composites.

3.1 Apparatus and Mechanism

To build an electrospinning set-up, one needs a high-voltage power supply, syringe pump, a spinneret, and a grounded collector plate (Figure 3.1). In electrospinning, a polymer or other viscous solution is fed through the spinneret attached to a high voltage power supply. The large voltage electrifies the solution, driving the electrospinning process. When the solution is electrified, the bead of spinning solution experiences electrostatic repulsion on its surface that competes with the surface tension within the bulk of the solution. The combined forces result in the stretching and elongation of the bead into a conical shape known as a Taylor cone (Figure 3.2).[3] When the voltage is high enough, such that the electrostatic forces are greater than the surface tension of the solution, a stream of solution jets from the tip of the cone. As the Taylor cone passes through the air, the electrified solution whips around due to electrostatic interactions between the external electric field and surface of the jet, the solvent evaporates, and the fibers continue to stretch, with final diameters as narrow as tens

of nm. The fibers then deposited onto the collector plate in a randomly oriented, nonwoven mat.

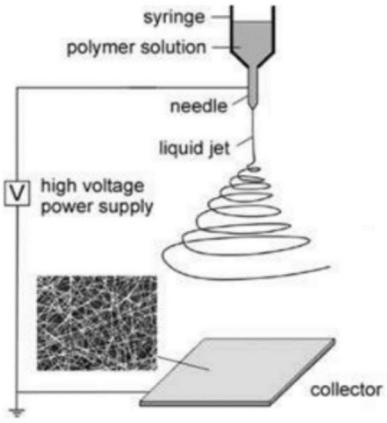

Figure 3.1 The basic electrospinning set-up using a high-voltage power supply, syringe pump (not shown), spinneret, and a collector plate. This set up produces non-woven fiber assemblies.[4]

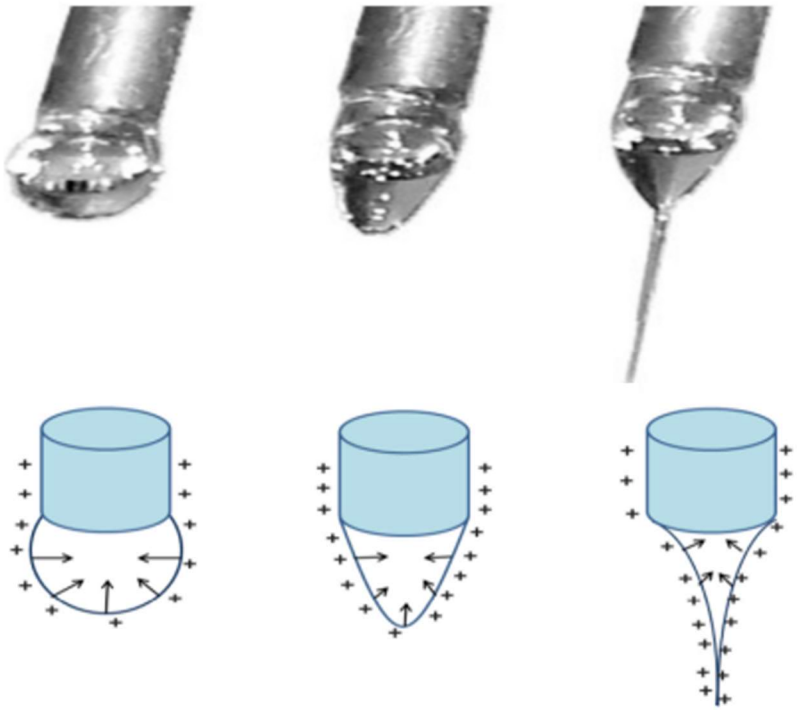

Figure 3.2 Image (top) and schematic (bottom) of the Taylor cone that forms during the electrospinning process when an increasing electric field (from left to right) is applied. As the field increases, charges on the surface increase, stretching the bead into a conical shape.[5]

3.2 Electrospinning Parameters

Although electrospinning is a relatively simple method for producing nanofibers, each material requires parameters to be optimized to achieve uniform fibers. If incorrect parameters are used, electrospray or beading can occur. The parameters can also be adjusted to control the overall diameter and morphology of the fibers.

3.2.1 Concentration of Solution for Electrospinning

One of the most important parameters in electrospinning is the concentration of the solution for electrospinning. During the formation of fibers through electrospinning, there is competition between the forces of surface tension that favor formation of individual particles and the surface charges that favor the formation of fibers. In addition to forming fibers or particles, there is also an intermediate state, where fibers form but consist of beads of polymer connected by narrow fibers.[6] The parameter that is most strongly connected the formation of beads is the viscosity or the concentration of the solution for electrospinning.[7,8] A high concentration of polymer with sufficient molecular weight will allow the polymer chain to become entangled, preventing the fibers from reshaping into beads or fibers. Increasing the concentration of the solution increases its viscoelasticity, causing it to resist rapid changes in shape, which inhibits formation of smooth fibers, resulting instead in beads in the fibers or individual particles, which is electrospray.[4] In addition to be important role of concentration and viscosity in obtaining smooth fibers of uniform diameter, concentration and viscosity also have a strong effect on the overall diameter of the fibers. Increasing the concentration of the solution for electrospinning has been shown to increase the fiber diameter.[9,10]

3.2.2 Flow Rate

The syringe pump controls the flow rate at which the solution for electrospinning is fed into the spinneret. If the flow rate is too high, forces drawing the fibers from the spinneret

are unable to keep up with the solution being fed into it, resulting in formation of droplets or beads.[11] Slightly elevated flow rates can result in the formation of fibers with larger diameters or ribbon-like shapes.[12,13] The decrease in diameter can be attributed to a decreases in surface charge. When the flow rate is too low, the spinning solution is depleted faster than it is being fed into the solution, causing instability in the Taylor cone, which results in large variations in the fiber diameter.[11]

3.2.3 Applied Voltage

The applied voltage causes the electrostatic forces that drive formation of the Taylor cone. If the voltage is now high enough to overtake the surface tension of the spinning solution, electrospinning is not possible.[14] Each material has a critical threshold voltage that needs to be overcome for electrospinning. Once this threshold voltage is exceeded, the impact of further voltage increases on the fiber diameter and morphology is less clear. Some researchers have shown that increasing voltage increases the fiber diameter,[15] while others have reported that increasing the voltage decreases the fiber diameter,[13] and others have reported that increasing the voltage causes bead formation of beads.[16] Ultimately, the impact of voltage on the diameter of the fibers depends on the specific system and situation.

3.2.4 Distance

The distance between the tip of the syringe and the collector plate can also affect the morphology of the fibers. If the tip is placed too close to the collector, then there is not enough time for the solvent to fully evaporate from the fibers.[12] Consequently, the fibers are

not fully "set," and points of contact between fibers merge into junctions, having a "welded" appearance in electron micrograph. Instead of a nonwoven mat, a cross-linked network of fibers forms. The distance can also impact the number of beads present in the fiber by limiting the amount of stretching that occurs before deposition.[13]

3.3 Patterning Fibers

The simplest method of producing electrospun fibers results a non-woven mat of continuous fibers on a flat surface. Although this pattern is useful a large variety of applications, alignment or other arrangements of the fibers are often desired. Given size the size scale of electrospun fibers and their mechanical fragility, it can be difficult to physically manipulate fibers into a desired design. As a result, methods have been developed to control the deposition of fibers during the electrospinning process.[1]

In-plane alignment of fibers can be achieved in a few different ways, either mechanically or electrostatically.[2] To mechanically produce aligned fibers, a rotating drum can be used to collect fibers. As the fibers are deposited on the surface of the drum, they mechanically align around the circumference of the drum, if is rotated at a high enough speed to match the rate of fiber deposition. The result is a large mat of aligned fibers on the drum surface. The simplest type of drum is a metal cylinder (Figure 4.1a). This method is relatively simple to implement but there is an intrinsic limit to the extent of alignment with rotating drums. Other approaches to mechanically aligning fibers include but are not limited to using

a wire drum instead of a solid drum (Figure 4.1b),[6] or using a rotating disk collector that focuses the aligned fibers on a narrow strip (Figure 4.1c).

Another approach for aligning electrospun fibers is to use electrostatics because the fibers are charged during the electrospinning process. By using two collection plates with a gap in between, an electric field is produced that directs the fibers to align across the gap, resulting in an aligned fiber mat. Such collectors can be made from parallel blades or wires (Figure 4.1d), but more complex arrays of fibers can be produced by making multiple parallel plates, resulting in simultaneous deposition of multiple orientations (Figure 4.1e). The fibers can also be collected as a twisted yarn if the fibers are collected on parallel hoops (Figure 4.1f).

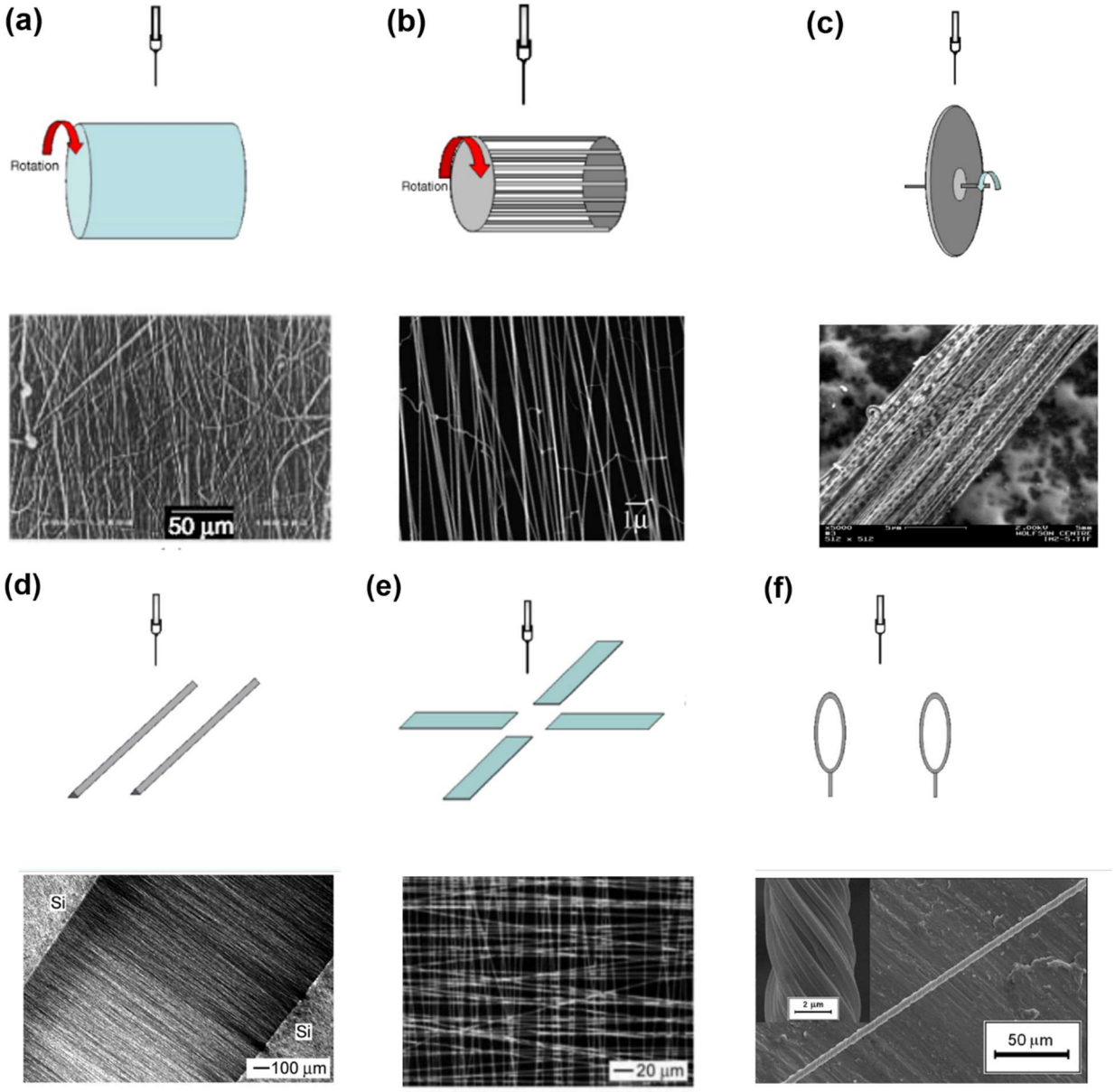

Figure 3.3 Various collectors for patterning electrospun fibers: (a) rotating drum,[17] (b) rotating wire drum,[6] (c) rotating disk,[18] (d) parallel electrodes,[19] (e) electrode array,[19] and (f) hoop.[20] Electrode diagrams are from Teo and Ramakrishna.[1]

3.4 Ceramic Fibers

Electrospinning is not restricted to polymers. Methods have been developed to electrospin ceramic and semiconductor fibers using techniques from sol gel chemistry. Techniques for producing electrospun ceramic fibers can classified in two categories, using a polymer additive to assist with electrospinning along with a ceramic precursor, and electrospinning relying exclusively on sol gel chemistry to produce a spinnable solution without adding a polymer to assist electrospinning.

3.4.1 Polymer-Assisted Electrospinning

Producing electrospun fibers begins with ceramic precursors, either a sol or a nanoparticle. The precursor for a desired ceramic material is selected and mixed with a polymer in a common solvent. The polymer carries the sol as it undergoes pulling, drying, and stretching. The fibers are then calcined to remove the polymer additive and sinter the ceramic precursor, forming the final product.[21] The ceramic precursor can interfere with the formation of fibers, which limits the choice of polymers for assisting electrospinning. Poly(vinyl alcohol) and poly(vinyl pyrolidone) are some of the more popular choices for polymer additives, but ceramic fibers have been produced using poly(vinyl acetate), polyacrylonitrile, and poly(methyl methacrylate).[22]

The appeal of polymer-assisted electrospinning is decoupling the spinnability of the polymer solution from the ceramic precursor sol. This provides greater flexibility in how ceramic precursor can be prepared to produce a desired product, with minimal concern over

how it will impact the spinnability of the sol. The type and concentration of the polymer additive can then be optimized to achieve the desired fiber morphology. As an added benefit, smaller diameter fibers can be achieved by lowering the concentration of ceramic precursor, while maintaining the same concentration of polymer. A wide range of ceramic fibers have been produced using polymer-assisted electrospinning, including TiO_2,[23] Al_2O_3,[24] SiO_2,[25] and more complex materials, such as $NiFe_2O_4$[26] and $PbZrTiO_2$, and even non-oxide ceramics, such as SiC[27] and B_4C.[28] A more complete list of ceramics that can be produced with electrospinning can be found in review by Ramaseshan et al. of electrospun ceramic fibers.[29]

3.4.2 Direct Electrospinning

Although polymer-assisted electrospinning of ceramic fibers is a simple and versatile process, for some applications, the calcination step can be problematic. The calcination step results in a large amount of shrinkage or breakage when the polymer is removed. Calcination also results in a decrease in the optical transparency of the fibers.[30] There is also evidence that removal of the polymer during the calcination can be incomplete, and residual carbon impurities can impact the properties of the ceramic fibers.[31]

To electrospin nanofibers without polymers, sol gel chemistry is exploited to produce a sol consisting of long chains with minimal branching and cross linking. Sol gel chemistry is the process of forming an inorganic gel from alkoxide precursors. SiO_2 is the most common material formed using sol gel chemistry, but many other materials can be formed using sol gel chemistry. To form a sol, alkoxide precursors, water, a solvent such as ethanol, and an

acid or base are mixed together. The mixture reacts and undergoes polymerization to form a gel. The alkoxide first undergoes hydrolysis, forming a M-OH (M = metal) group on the alkoxide. The M-OH group is the active species in the polymerization reaction. After the initial hydrolysis reaction, polycondensation of the alkoxide complexes occurs, resulting in the formation of longer chains of alkoxides.[32] These chemical reactions are written out below.

$(RO)_3M(OR) + H_2O \leftrightharpoons M(OR)_3OH + ROH$ Hydrolysis

$(RO)_3MOH + (RO)_3MOH \leftrightharpoons (RO)_3M\text{-}O\text{-}M(OR)_3 + H_2O$ Condensation

$(RO)_3MOH + (RO)_3MOR \leftrightharpoons (RO)_3M\text{-}O\text{-}M(OR)_3 + ROH$ Alcohol Condensation

To achieve a sol conducive to fiber formation through electrospinning, hydrolysis and condensation need to be controlled to facilitate formation of long-chained sols with minimal branching. A well understood method of guiding hydrolysis and condensation toward long chains is to use an acid catalyst in the synthesis.[32,33] In an-acid catalyzed sol, the rate of condensation is higher than the rate of hydrolysis, resulting in the formation of longer chains as opposed to forming new branches. In contrast, base-catalyzed processes favor hydrolysis over condensation, resulting in the formation of highly branched, nanoparticle-like structures. The difference between acid- and base-catalyzed gels is visualized in Figure 3.4.

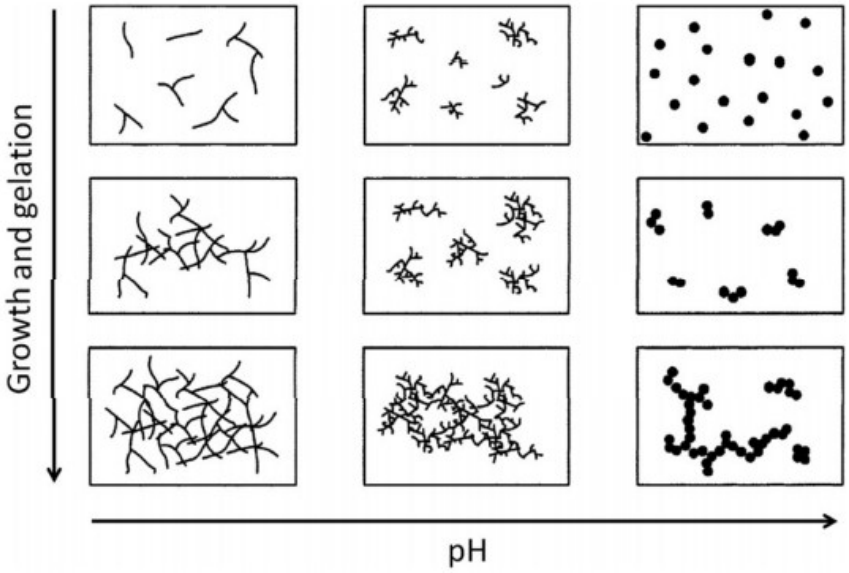

Figure 3.4 The difference in sol and gel structure when formed in an acidic and a basic solution.[34]

Another factor important in formation of long-chained sols with minimal branching is the ratio to alkoxide to water. Theoretically, a 2:1 ratio of water to a metal tetraalkoxide should result in complete condensation of the alkoxide. To do this, 2 of the 4 alkoxy groups would need to be hydrolyzed and the other two groups could undergo alcohol condensation with another alkoxy group. In reality, the reaction is not that efficient, and a ratio of 2:1 results in an incomplete reaction. Using a ratio greater than 2:1 produces a more completely condensed oxide. Using a ratio less than 2:1 results in the formation of a more ladder-like chain of condensed alkoxides[35] (Figure 3.5). Using a ratio of 2:1 alkoxide to water has been reported to produce the long-chained morphology required for electrospinning.[36]

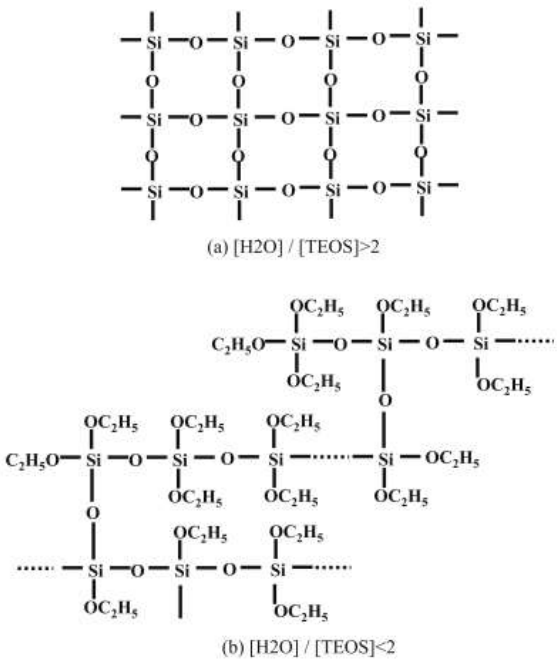

Figure 3.5 The morphology of a silica sol when the molar ratio of water to alkoxide is (a) > 2 or (b) < 2.[35]

After preparation of a viscous sol capable of entanglement, the sol can be spun using the same electrospinning methods as polymer electrospinning. The level of control over sol gel chemistry required to produce a spinnable solution is a challenge that has thus far limited the use of direct electrospinning. Only a few alkoxide precursors are known to provide the level of control needed for electrospinning, and there have been only a few examples of direct electrospun ceramic fibers. SiO_2 fibers have been produced using tetraethylorthsilicate.[37-40] Al_2O_3 fibers have been produced using aluminum *sec*-butoxide as the precursor.[41] TiO_2 fibers have been produced from titanium (IV) isopropoxide.[42,43]

$PbZrTiO_2$ has been produced using a combination of lead 2-ethylhexanoate, zirconium *n*-propoxide, and titanium (IV) isopropoxide.[44,45]

3.5 References

(1) Teo, W. E.; Ramakrishna, S. A review on electrospinning design and nanofibre assemblies. *Nanotechnology* **2006**, *17*, R89.

(2) Huang, Z.-M.; Zhang, Y. Z.; Kotaki, M.; Ramakrishna, S. A review on polymer nanofibers by electrospinning and their applications in nanocomposites. *Composites Science and Technology* **2003**, *63*, 2223-2253.

(3) Taylor, G. Disintegration of Water Drops in an Electric Field. *Proceedings of the Royal Society of London. Series A. Mathematical and Physical Sciences* **1964**, *280*, 383-397.

(4) Li, D.; Xia, Y. Electrospinning of Nanofibers: Reinventing the Wheel? *Adv Mater* **2004**, *16*, 1151-1170.

(5) Haider, A.; Haider, S.; Kang, I.-K. A comprehensive review summarizing the effect of electrospinning parameters and potential applications of nanofibers in biomedical and biotechnology. *Arabian Journal of Chemistry* **2015**.

(6) Katta, P.; Alessandro, M.; Ramsier, R. D.; Chase, G. G. Continuous Electrospinning of Aligned Polymer Nanofibers onto a Wire Drum Collector. *Nano Lett* **2004**, *4*, 2215-2218.

(7) Leach, M. K.; Feng, Z.-Q.; Tuck, S. J.; Corey, J. M. Electrospinning Fundamentals: Optimizing Solution and Apparatus Parameters. *Journal of Visualized Experiments : JoVE* **2011**, 2494.

(8) Liu, Y.; He, J.-H.; Yu, J.-y.; Zeng, H.-m. Controlling numbers and sizes of beads in electrospun nanofibers. *Polymer International* **2008**, *57*, 632-636.

(9) Tarus, B.; Fadel, N.; Al-Oufy, A.; El-Messiry, M. Effect of polymer concentration on the morphology and mechanical characteristics of electrospun cellulose acetate and poly (vinyl chloride) nanofiber mats. *Alexandria Engineering Journal* **2016**, *55*, 2975-2984.

(10) Beachley, V.; Wen, X. Effect of electrospinning parameters on the nanofiber diameter and length. *Materials science & engineering. C, Materials for biological applications* **2009**, *29*, 663-668.

(11) Zargham, S.; Bazgir, S.; Tavakoli, A.; Rashidi, A. S.; Damerchely, R. The Effect of Flow Rate on Morphology and Deposition Area of Electrospun Nylon 6 Nanofiber. *Journal of Engineered and Fibers and Fabrics* **2012**, *7*, 42-49.

(12) Li, Z.; Wang, C. Effects of Working Parameters on Electrospinning. In *One-Dimensional nanostructures: Electrospinning Technique and Unique Nanofibers*, Springer Berlin Heidelberg: Berlin, Heidelberg, 2013; pp 15-28.

(13) Megelski, S.; Stephens, J. S.; Chase, D. B.; Rabolt, J. F. Micro- and Nanostructured Surface Morphology on Electrospun Polymer Fibers. *Macromolecules* **2002**, *35*, 8456-8466.

(14) Shi, X.; Zhou, W.; Ma, D.; Ma, Q.; Bridges, D.; Ma, Y.; Hu, A. Electrospinning of Nanofibers and Their Applications for Energy Devices. *Journal of Nanomaterials* **2015**, *2015*, 20.

(15) Zhang, C.; Yuan, X.; Wu, L.; Han, Y.; Sheng, J. Study on morphology of electrospun poly(vinyl alcohol) mats. *European Polymer Journal* **2005**, *41*, 423-432.

(16) Deitzel, J. M.; Kleinmeyer, J.; Harris, D.; Beck Tan, N. C. The effect of processing variables on the morphology of electrospun nanofibers and textiles. *Polymer* **2001**, *42*, 261-272.

(17) Wannatong, L.; Sirivat, A.; Supaphol, P. Effects of solvents on electrospun polymeric fibers: preliminary study on polystyrene. *Polymer International* **2004**, *53*, 1851-1859.

(18) Theron, A.; Zussman, E.; Yarin, A. L. Electrostatic field-assisted alignment of electrospun nanofibres. *Nanotechnology* **2001**, *12*, 384.

(19) Li, D.; Wang, Y.; Xia, Y. Electrospinning of Polymeric and Ceramic Nanofibers as Uniaxially Aligned Arrays. *Nano Lett* **2003**, *3*, 1167-1171.

(20) Dalton, P. D.; Klee, D.; Möller, M. Electrospinning with dual collection rings. *Polymer* **2005**, *46*, 611-614.

(21) Wu, H.; Pan, W.; Lin, D.; Li, H. Electrospinning of ceramic nanofibers: Fabrication, assembly and applications. *Journal of Advanced Ceramics* **2012**, *1*, 2-23.

(22) Dai, Y.; Liu, W.; Formo, E.; Sun, Y.; Xia, Y. Ceramic nanofibers fabricated by electrospinning and their applications in catalysis, environmental science, and energy technology. *Polymers for Advanced Technologies* **2011**, *22*, 326-338.

(23) Li, D.; Xia, Y. Fabrication of Titania Nanofibers by Electrospinning. *Nano Lett* **2003**, *3*, 555-560.

(24) Brinker, C. J.; Scherer, G. W. *Sol-gel science: the physics and chemistry of sol-gel processing*. Academic Press: Boston, 1990.

(25) Changlu, S.; Hakyong, K.; Jian, G.; Doukrae, L. A novel method for making silica nanofibres by using electrospun fibres of polyvinylalcohol/silica composite as precursor. *Nanotechnology* **2002**, *13*, 635.

(26) Li, D.; Herricks, T.; Xia, Y. Magnetic nanofibers of nickel ferrite prepared by electrospinning. *Applied Physics Letters* **2003**, *83*, 4586-4588.

(27) Liu, H. A.; Balkus, K. J. Electrospinning of beta silicon carbide nanofibers. *Materials Letters* **2009**, *63*, 2361-2364.

(28) Welna, D. T.; Bender, J. D.; Wei, X.; Sneddon, L. G.; Allcock, H. R. Preparation of Boron-Carbide/Carbon Nanofibers from a Poly(norbornenyldecaborane) Single-Source Precursor via Electrostatic Spinning. *Adv Mater* **2005**, *17*, 859-862.

(29) Ramaseshan, R.; Sundarrajan, S.; Jose, R.; Ramakrishna, S. Nanostructured ceramics by electrospinning. *Journal of Applied Physics* **2007**, *102*, 111101.

(30) Tätte, T.; Hussainov, M.; Paalo, M.; Part, M.; Talviste, R.; Kiisk, V.; Mändar, H.; Põhako, K.; Pehk, T.; Reivelt, K.; Natali, M.; Gurauskis, J.; Lõhmus, A.; Mäeorg, U. Alkoxide-based precursors for direct drawing of metal oxide micro- and nanofibres. *Science and Technology of Advanced Materials* **2011**, *12*, 034412.

(31) Tuttle, R. W.; Chowdury, A.; Bender, E. T.; Ramsier, R. D.; Rapp, J. L.; Espe, M. P. Electrospun ceramic fibers: Composition, structure and the fate of precursors. *Applied Surface Science* **2008**, *254*, 4925-4929.

(32) Innocenzi, P. From the Precursor to a Sol. In *The Sol to Gel Transition*, Innocenzi, P., Ed. Springer International Publishing: Cham, 2016; pp 7-25.

(33) Boyd, T. Preparation and properties of esters of polyorthotitanic acid. *Journal of Polymer Science* **1951**, *7*, 591-602.

(34) Danks, A. E.; Hall, S. R.; Schnepp, Z. The evolution of 'sol-gel' chemistry as a technique for materials synthesis. *Materials Horizons* **2016**, *3*, 91-112.

(35) Iimura, K.; Oi, T.; Suzuki, M.; Hirota, M. Preparation of silica fibers and non-woven cloth by electrospinning. *Advanced Powder Technology* **2010**, *21*, 64-68.

(36) Sakka, S.; Yoko, T. Fibers from gels. *Journal of Non-Crystalline Solids* **1992**, *147*, 394-403.

(37) Choi, S.-S.; Lee, S. G.; Im, S. S.; Kim, S. H.; Joo, Y. L. Silica nanofibers from electrospinning/sol-gel process. *Journal of Materials Science Letters* **2003**, *22*, 891-893.

(38) Zhang, G.; Kataphinan, W.; Teye-Mensah, R.; Katta, P.; Khatri, L.; Evans, E. A.; Chase, G. G.; Ramsier, R. D.; Reneker, D. H. Electrospun nanofibers for potential space-based applications. *Materials Science and Engineering: B* **2005**, *116*, 353-358.

(39) Geltmeyer, J.; Van der Schueren, L.; Goethals, F.; De Buysser, K.; De Clerck, K. Optimum sol viscosity for stable electrospinning of silica nanofibres. *Journal of Sol-Gel Science and Technology* **2013**, *67*, 188-195.

(40) Patel, A. C.; Li, S.; Yuan, J.-M.; Wei, Y. In Situ Encapsulation of Horseradish Peroxidase in Electrospun Porous Silica Fibers for Potential Biosensor Applications. *Nano Lett* **2006**, *6*, 1042-1046.

(41) Maneeratana, V.; Sigmund, W. M. Continuous hollow alumina gel fibers by direct electrospinning of an alkoxide-based precursor. *Chemical Engineering Journal* **2008**, *137*, 137-143.

(42) Won Keun, S.; Donghwan, C.; Won Ho, P. Direct electrospinning of ultrafine titania fibres in the absence of polymer additives and formation of pure anatase titania fibres at low temperature. *Nanotechnology* **2006**, *17*, 439.

(43) Kim, Y. B.; Cho, D.; Park, W. H. Enhancement of mechanical properties of TiO2 nanofibers by reinforcement with polysulfone fibers. *Materials Letters* **2010**, *64*, 189-191.

(44) Yu, W.; Jorge, J. S.-A. Synthesis of lead zirconate titanate nanofibres and the Fourier-transform infrared characterization of their metallo-organic decomposition process. *Nanotechnology* **2004**, *15*, 32.

(45) Wang, Y.; Santiago-Avilés, J. J. A Review on Synthesis and Characterization of Lead Zirconate Titanate Nanofibers through Electrospinning. *Integrated Ferroelectrics* **2011**, *126*, 60-76.

CHAPTER 4. Aggregation and DLVO Theory

Aggregation is an underutilized but potentially powerful tool for assembling composite nanoparticles (NPs) that involves manipulating the mechanisms for colloidal stability of NPs. By controlling the type and rate of aggregation in a system, novel composite NPs can be formed.

4.1 DLVO Theory

Over the years, many theories have been developed to understand colloidal stability and aggregation. Several of these theories have coalesced into a single theory known as the Derjaguin, Landau, Verway, and Overbeek, or DLVO theory of aggregation.[1-3] At its simplest, DLVO theory is the idea that the interaction energy of two equivalent particles or surfaces can be understood using the equation

$$V_t = V_{vdW} + V_e \quad , \qquad (1)$$

where V_t is the total interaction energy, V_{vdW} is the van der Waals potential, and V_e is electrostatic repulsion potential. The potential from Van der Waals forces, V_{vdW} is a short-range, attractive force that quickly drops to zero as distance between two particles increases. Van der Waals attraction is composed of three forces, the interaction between two permanent dipoles, called the Keesom force, the interaction between a permanent dipole and an induced dipole, called the Debye force, and the interaction between two induced dipoles, called the London dispersion force.[4] V_{vdW} can be described using the equation[5,6]

$$\frac{V_{VdW}}{kT} = -\frac{A}{64kT}\left(\frac{2a^2}{s((4a+s)} + \frac{2a^2}{(2a+s)^2}\ln\frac{s(4a+s)}{(2a+s)^2}\right), \quad (2)$$

where A is the Hamaker constant, k is the Boltzmann constant, T is absolute temperature, a is the average particle radius, and s is the distance between two particles.

The repulsive electrostatic force, originates from charges on the surface of a particle. A more detailed description particle surface changes and its formation as an electrical double layer can be found in Section 1.5. The potential derived from the electrostatic force, V_e can be described using the equations[5,7]

$$\frac{V_e}{kT} = \frac{64\pi nkT}{\kappa}\frac{(a+\delta)^2}{(s+2a)}\left[\tanh\frac{ze\Psi_d}{4kT}\right]^2 e^{-\kappa(s-2\delta)} \quad \text{and} \quad \kappa = \left[\frac{\sum_i^N e^2 z_i^2 n_i}{\varepsilon_{rs}\varepsilon_0}\right] \quad (3,4)$$

where n is the number concentration of ions, κ is the inverse Debye length, δ is the Stern layer thickness, z is the electrolyte valence, e is elementary charge of an electron, Ψ_d is the diffusion potential, N is the number of ionic species, z_i is the valence of the electrolyte ion i, n_i is the number concentration of electrolyte ions, ε_{rs} is the relative permittivity of the electrolyte solution, and ε_o is the electric permittivity of a vacuum.

An interaction energy curve describing aggregation can be made by plotting V_t as a function of interparticle distance. The plot that results has multiple features that describe colloidal stability and aggregation (Figure 4.1). As two particles approach each other, an energy barrier (E_a) is encountered. At closer distances, there is a deep, attractive energy well (E_w), that is generally much deeper than thermal energy. As a result, particles that overcome

E_a, move into E_w and become trapped at a fixed distance. Figure 4.1 also includes a steep increase in the interaction energy at shorter distances. It should be noted that when adding Eq. 1 and 2, the plot goes to negative infinity as the interparticle distance approaches zero. DLVO theory does not account for Born repulsion, repulsive forces from electron cloud overlap that overwhelm the attractive forces at small interparticle distances.[8,9]

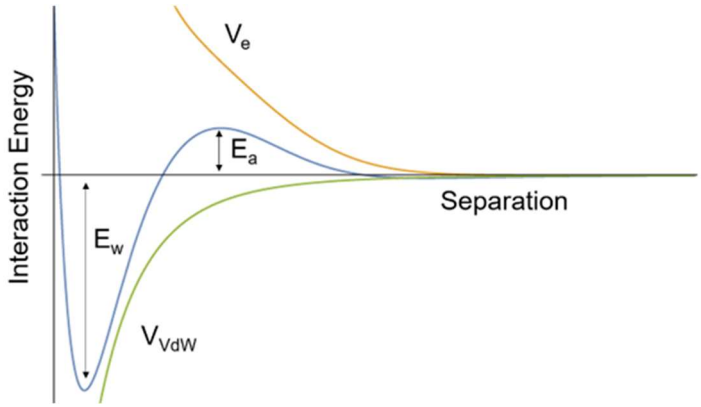

Figure 4.1 Schematic of the interaction energy curve (V_t) of two particles, as a sum the van der Waals, V_{vdW}, and the electrostatic bilayer, V_{es}, terms as a function of separation distance. E_a is the energy barrier to aggregation and E_w is energy well that keeps aggregated particles attached to one another. Schematic is not to scale, instead elements are adjusted to enhance clarity.

Although Figure 4.1 is a general interaction energy curve, it does not describe every circumstance. If E_a is greater than thermal energy in the system (kT), aggregation is unlikely to occur (Figure 4.2a). If $E_a = 0$, then there is no barrier to aggregation, and when two particles come close enough to each other, they will immediately aggregate (Figure 4.2c). If

E_a is present but less than the kT, the situation is more complex. kT is a distribution of energies and only a fraction of particle interactions will result in aggregation. A system with a higher E_a will have a slower rate of aggregation than a system with a lower E_a. The ramifications of the height of E_a on particle aggregation will be explored in Section 4.3.

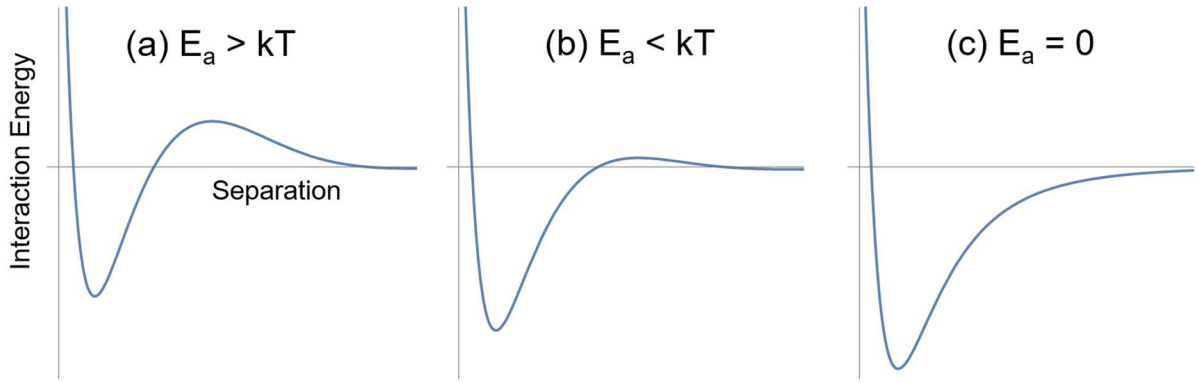

Figure 4.2 Three regimes of aggregation behavior, determined by the height of the aggregation barrier, E_a: (a) high aggregation barrier, $E_a > kT$, (b) low aggregation barrier, $E_a < kT$, and (c) no aggregation barrier.

4.2 Non-DLVO Forces

Although DLVO theory is a useful framework for modeling aggregation, the use of van der Waals attraction and electrostatic repulsions is often insufficient to adequately understand the forces involved in interactions between most kinds of particles. DLVO theory fails to take into account the presence of solvent molecules, ligands, surface roughness, surface reactivity, and a host of other factors that are unique to each system. The following are some of the more common forces that are not included in DLVO theory, but have been

used to describe aggregation in particle systems, referred to as non-DLVO or X-DLVO forces.

4.2.1 Steric Stabilization

Particles are often encapsulated with a polymer coating to prevent agglomeration. Polymer coatings provide steric stabilization. When two sterically stabilized particles collide, the polymer chains are compressed, which decreases their entropy. Reducing the entropy increases the Gibbs free energy of the system, resulting in elastic repulsive forces.[10] The elastic force that results from steric stabilization can be used to derive V_{st}, the steric repulsion potential. V_{st} can be described using two equations, one describing repulsive forces when the interparticle distance, $s > d$, the thickness of the polymer layer, another for $s \leq d$.[5,11]

$$d \leq s \Longrightarrow \left\{\frac{V_{st}}{kT} = 0\right\} \quad \text{and} \tag{5}$$

$$d > s \Longrightarrow \left\{\frac{V_{st}}{kT} = \left(\frac{2\pi}{M_w}\phi_p d^2 \rho_p\right)\left\{\frac{s}{d}\ln\left[\frac{s}{d}\left(\frac{3-s/d}{2}\right)^2\right]\right\} - 6\ln\left(\frac{3-s/d}{2}\right) + 3\left(1+\frac{s}{d}\right)\right\} \tag{6}$$

where d is the thickness of the polymer coating, M_w is the molecular weight of the polymer, ϕ_p is the volume fraction of the polymer, and ρ_p is the density of the polymer, and a is the diameter of the core particle. Equation 6 assumes the polymer layer has a uniform density and that the polymer does not begin compression until $d = s$.

4.2.2 Osmotic Repulsion

Another contribution to the stability of polymer-stabilized particles is osmotic pressure. When two particles collide, in addition to the entropy effect discussed above, compression of the polymer chains also results in increased osmotic pressure, which causes repulsion.[12] Osmotic repulsion, V_{osm}, can be described using three equations depending on the regime of behavior, which is determined by whether the interparticle distance is greater than the thickness of both interacting polymer layers, less than thickness of one polymer layer, or somewhere in-between.

$$2d \leq s \Longrightarrow \left\{\frac{V_{osm}}{kT} = 0\right\} \tag{7}$$

$$d \leq d \leq 2d \Longrightarrow \left\{\frac{V_{osm}}{kT} = \frac{a4\pi}{v_1}\phi_p^2\left(\frac{1}{2} - \chi\right)\left(d - \frac{s}{2}\right)^2\right\} \tag{8}$$

$$s < d \Longrightarrow \left\{\frac{V_{osm}}{kT} = \frac{a4\pi}{v_1}\phi_p^2\left(\frac{1}{2} - \chi\right)d^2\left(\frac{s}{2d} - \frac{1}{4} - \ln\frac{s}{d}\right)\right\}, \tag{9}$$

where χ is the Flory-Huggins solvency parameter and v_1 is the volume of a solvent moecule.

4.2.3. Hydrophobic Effect

In the context of DLVO theory of particles, the hydrophobic effect is the tendency of hydrophobic particles to aggregate when in an aqueous or other polar environment.[13,14] The driving force of the hydrophobic effect is minimization of the surface area exposed to a hydrophilic solvent or surface. The energy cost to solvate a hydrophobic particle can be

minimized by decreasing the amount of exposed surface to be solvated by aggregating.[15] The source of the hydrophobic affect is hydrogen bonding or Lewis acid-base interactions. There is an energy cost for breaking hydrogen bonds within the solvent, and minimizing exposure to the hydrophobic surface minimizes the number of bonds that are broken.[16] The potential that results from the hydrophobic effect, V_H can be described using the equations[5,16,17]

$$\frac{V_H}{surface\ area} = \Delta G_{s_0}^{AB}\left(e^{\frac{s_0 - s}{\lambda_{AB}}}\right) \tag{10}$$

where s_o is the minimum equilibrium separation distance of two particles due to Born repulsion, $\Delta G_{s_0}^{AB}$ is the free energy of acid-base interactions between particles at s_o, and λ_{AB} is the decay length for acid-base interaction, the distance at which the acid-base interaction is completely screened.

4.2.4 Solvation Forces

As was discussed in Section 1.5, the electrical double layer is more complex than a charged surface. In an aqueous environment, ions and water molecules bind to the surface of the particle and have limited mobility. This layer of solvent molecules provides a repulsive force that serves to prevent aggregation.[17] Solvation forces can be described using the equation[12,18]

$$V_s = 2\pi a P_o \lambda_s^2 e^{-(d/\lambda_s)} \tag{11}$$

where P_o is the solvation pressure as the separation distance approaches zero and λ_s is the decay length for the solvation force, or the distance at which the solvation force is completely screened.

4.2.5 Heteroaggregation

DLVO theory was developed to model the aggregation of two or more particles of the same type, a process more precisely referred to as homoaggregation. Aggregation of two or more different types of particles is referred to as heteroaggregation. Heteroaggregation introduces an added level of complexity. When mixing dissimilar particles, A and B, together, heteroaggregation introduces a higher level of complexity. Instead of only one type of interaction, three different interactions can occur, AA, BB, and AB. When three types of particles are mixed together, six interactions can occur, AA, AB, AC, BB, BC, and CC. The situation is further complicated because each kind of particle has its own mechanisms of stabilization, DLVO and non-DLVO forces, and its own aggregation barrier (Figure 4.3). The equations discussed above were developed to model homoaggregation and must be modified to describe heteroaggregation. Consequently, applying DLVO theory to heteroaggregation is much complex than homoaggregation.[19-21]

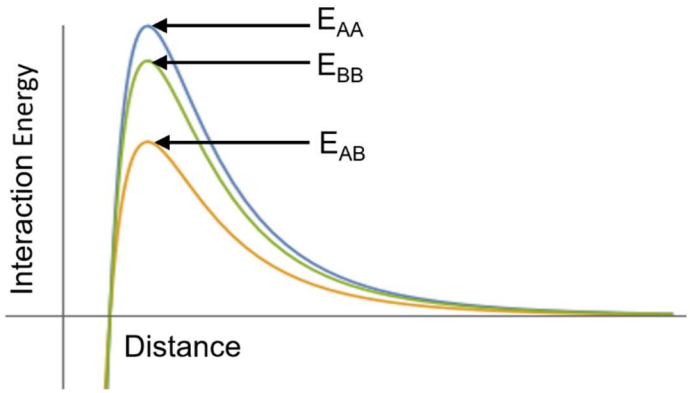

Figure 4.3 Schematic of the interaction energies in a binary particle system. E_{AA}, E_{BB}, and E_{AB}, are the aggregation barriers for each type of aggregation.

4.3 Aggregate Morphology

There are two distinct classes of aggregates that can form in a system. Diffusion-limited aggregation or cluster aggregation (DLA or DLCA) can be best described as aggregation when there is no aggregation barrier (Figure 4.2c). In this regime, aggregation is irreversible and assumed to occur 100% of the time when two particles collide. As such, the only factor that limits the growth of aggregates is the collision rate of the particles. Because of the randomness of collisions and the irreversible nature, DLA aggregates are less dense and possess a fractal-like morphology (Figure 4.4).

In reaction-limited aggregation or cluster aggregation (RLA or RLCA), there is a barrier to aggregation, but it can be overcome (Figure 4.2b). In this regime, particles are capable of aggregation, but not all collisions result in aggregation. This implies that after a particle collides with an aggregate, the particle can still move deeper into the cluster before

aggregation occurs. In this regime, aggregated particles can also redisperse. Particles that redisperse can then collide with the cluster at a different location, but particles that aggregate at a site with a higher coordination number are less likely to redisperse. Because of this capability for reconfiguration, RLA clusters are typically more densely packed than DLA clusters[22-26] (Figure 4.4).

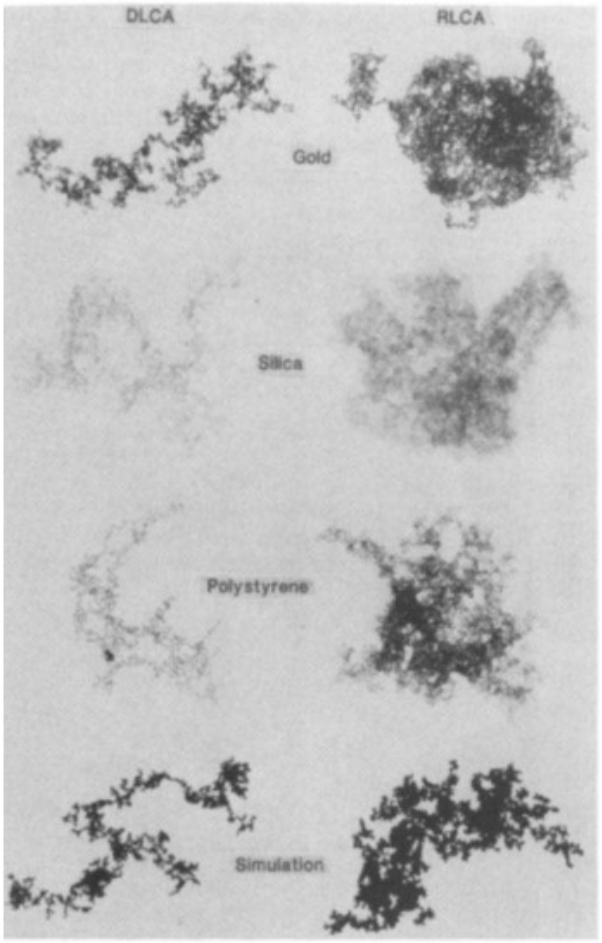

Figure 4.4 From top to bottom, TEM images of gold, silica, polystyrene, and simulated particles that have undergone (left) DLCA and (right) RLCA.[22]

4.4 Inducing Aggregation

Aggregation is often viewed as a negative feature in NP research, because it indicates a lack of stability of the dispersion of NPs in a solvent. Some researchers have developed methods of exploiting aggregation to remove undesired NP, assemble NP superlattices, and to assemble multi-NP aggregates.

As was discussed in Section 4.4, the barrier to aggregation can control whether less dense, random aggregates or more dense, structured aggregates form. Many of the parameters above can be adjusted by manipulating properties of the solvent or the surface of the NP. By subtly modifying the properties of the solvent, aggregation can be induced in such a way to encourage the assembly of nanoclusters and supracrystals.[27] Hydrophobic NPs dispersed in less polar environments, such as hexanes and toluene, and are stabilized primarily by steric and osmotic forces. Adding more polar solvents, such as ethanol and methanol, can enhance hydrophobic forces[28] and reduce steric forces[29] to lower the aggregation barrier enough to induce aggregation (Figure 4.5).[28-31] An alternative approach is to disperse NPs in a mixture of solvents of different polarities and boiling points, octane and octanol for example, and allow the solution to evaporate. As the solution evaporates, the lower boiling point solvent evaporates at a greater rate and as result, the solvent gradually increases, inducing aggregation of NPs with hydrophobic coatings or ligands.[32,33] Precise amount of electrolytes can also be added to a dispersion of NPs, to screen electrostatic repulsion enough to induce aggregation.[34] For pH sensitive NPs such as silica or titania, the pH can be varied to induce aggregation by changing the charge on the surface of the NP.[34-36]

With a sufficient understanding of the attractive and repulsive forces for a NP with a specific composition, size, shape, stabilizing agent, and solvent environment, the aggregation process can be controlled to favor desired products.

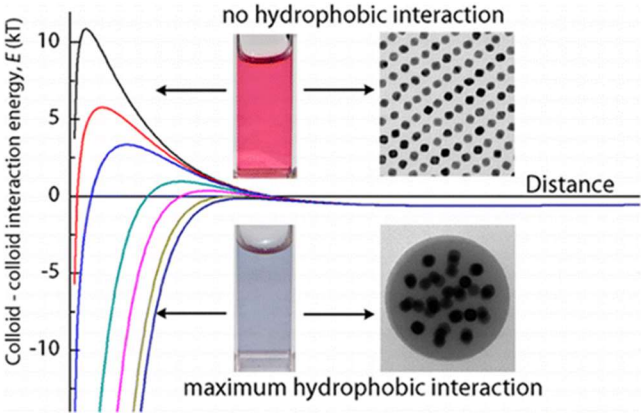

Figure 4.5 Homoaggregation of hydrophobic gold NPs (top) to form controlled nanoclusters (bottom) through the addition of water. Adding water decreases the barrier to aggregation.[28]

Selective heteroaggregation can be used to assemble composite NPs. The most common method of inducing heteroaggregation is to select oppositely charged NPs. Electrostatic interactions simultaneously cause repulsive forces that prevent homoaggregation and attractive forces that drive heteroaggregation.[36-39] Under the right conditions, simply mixing NPs together can drive heteroaggregation.[40,41]

The previous examples of inducing heteroaggregation involve selecting or modifying NPs for the purpose of inducing heteroaggregation. Much work on inducing homoaggregation to form clusters and assemblies involves tuning the solvent environment such that the barrier of aggregation is low enough to control homoaggregation. Until now, we

are not aware of research to tune the solvent environment to drive heteroaggregation in an analogous manner. A method of assembling hydrophobic magnetite NPs onto silica-overcoated gold nanorods by solvent-induced heteroaggregation is presented in Chapter 5.

4.5 References

(1) Derjaguin, B. V.; Churaev, N. V.; Muller, V. M. The Derjaguin—Landau—Verwey—Overbeek (DLVO) Theory of Stability of Lyophobic Colloids. In *Surface Forces*, Derjaguin, B. V.; Churaev, N. V.; Muller, V. M., Eds. Springer US: Boston, MA, 1987; pp 293-310.

(2) Derjaguin, B.; Landau, L. Theory of the stability of strongly charged lyophobic sols and of the adhesion of strongly charged particles in solutions of electrolytes. *Progress in Surface Science* **1993**, *43*, 30-59.

(3) Verwey, E. J. W. Theory of the Stability of Lyophobic Colloids. *The Journal of Physical and Colloid Chemistry* **1947**, *51*, 631-636.

(4) Bergström, L. Hamaker constants of inorganic materials. *Advances in Colloid and Interface Science* **1997**, *70*, 125-169.

(5) Hotze, E. M.; Phenrat, T.; Lowry, G. V. Nanoparticle Aggregation: Challenges to Understanding Transport and Reactivity in the Environment. *Journal of Environmental Quality* **2010**, *39*, 1909-1924.

(6) Stumm, W.; Morgan, J. J. *Aquatic chemistry: chemical equilibria and rates in natural waters*. Wiley: 1996.

(7) Delgado, A. V.; González-Caballero, F.; Hunter, R. J.; Koopal, L. K.; Lyklema, J. Measurement and interpretation of electrokinetic phenomena. *J Colloid Interface Sci* **2007**, *309*, 194-224.

(8) Puri, A.; Loomis, K.; Smith, B.; Lee, J.-H.; Yavlovich, A.; Heldman, E.; Blumenthal, R. Lipid-Based Nanoparticles as Pharmaceutical Drug Carriers: From Concepts to Clinic. *Critical reviews in therapeutic drug carrier systems* **2009**, *26*, 523-580.

(9) Lebovka, N. I. Aggregation of Charged Colloidal Particles. In *Polyelectrolyte Complexes in the Dispersed and Solid State I: Principles and Theory*, Müller, M., Ed. Springer Berlin Heidelberg: Berlin, Heidelberg, 2014; pp 57-96.

(10) Evans, R.; Napper, D. H. Steric stabilization II. *Kolloid-Zeitschrift und Zeitschrift für Polymere* **1973**, *251*, 329-336.

(11) Fritz, G.; Schädler, V.; Willenbacher, N.; Wagner, N. J. Electrosteric Stabilization of Colloidal Dispersions. *Langmuir* **2002**, *18*, 6381-6390.

(12) de Gennes, P. G. Polymers at an interface; a simplified view. *Advances in Colloid and Interface Science* **1987**, *27*, 189-209.

(13) Blokzijl, W.; Engberts, J. B. F. N. Hydrophobic Effects. Opinions and Facts. *Angewandte Chemie International Edition in English* **1993**, *32*, 1545-1579.

(14) Grasso*, D.; Subramaniam, K.; Butkus, M.; Strevett, K.; Bergendahl, J. A review of non-DLVO interactions in environmental colloidal systems. *Reviews in Environmental Science and Biotechnology* **2002**, *1*, 17-38.

(15) Chandler, D. Interfaces and the driving force of hydrophobic assembly. *Nature* **2005**, *437*, 640-647.

(16) Wu, W.; Giese, R. F.; van Oss, C. J. Stability versus flocculation of particle suspensions in water—correlation with the extended DLVO approach for aqueous systems, compared with classical DLVO theory. *Colloids and Surfaces B: Biointerfaces* **1999**, *14*, 47-55.

(17) Hoek, E. M. V.; Agarwal, G. K. Extended DLVO interactions between spherical particles and rough surfaces. *J Colloid Interface Sci* **2006**, *298*, 50-58.

(18) Molina-Bolívar, J. A.; Ortega-Vinuesa, J. L. How Proteins Stabilize Colloidal Particles by Means of Hydration Forces. *Langmuir* **1999**, *15*, 2644-2653.

(19) Wang, H.; Adeleye, A. S.; Huang, Y.; Li, F.; Keller, A. A. Heteroaggregation of nanoparticles with biocolloids and geocolloids. 2015.

(20) Trefalt, G.; Ruiz-Cabello, F. J. M.; Borkovec, M. Interaction Forces, Heteroaggregation, and Deposition Involving Charged Colloidal Particles. *The Journal of Physical Chemistry B* **2014**, *118*, 6346-6355.

(21) Islam, A. M.; Chowdhry, B. Z.; Snowden, M. J. Heteroaggregation in colloidal dispersions. *Advances in Colloid and Interface Science* **1995**, *62*, 109-136.

(22) Lin, M. Y.; Lindsay, H. M.; Weitz, D. A.; Ball, R. C.; Klein, R.; Meakin, P. Universality in colloid aggregation. *Nature* **1989**, *339*, 360-362.

(23) Meakin, P.; Jullien, R. The effects of restructuring on the geometry of clusters formed by diffusion-limited, ballistic, and reaction-limited cluster–cluster aggregation. *The Journal of Chemical Physics* **1988**, *89*, 246-250.

(24) Asnaghi, D.; Carpineti, M.; Giglio, M.; Sozzi, M. Coagulation kinetics and aggregate morphology in the intermediate regimes between diffusion-limited and reaction-limited cluster aggregation. *Physical Review A* **1992**, *45*, 1018-1023.

(25) Weitz, D. A.; Huang, J. S.; Lin, M. Y.; Sung, J. Limits of the Fractal Dimension for Irreversible Kinetic Aggregation of Gold Colloids. *Physical Review Letters* **1985**, *54*, 1416-1419.

(26) Ben-Naim, E.; Krapivsky, P.; Leyvraz, F.; Redner, S. Kinetics of Ballistically-Controlled Reactions. *The Journal of Physical Chemistry* **1994**, *98*, 7284-7288.

(27) Boles, M. A.; Engel, M.; Talapin, D. V. Self-Assembly of Colloidal Nanocrystals: From Intricate Structures to Functional Materials. *Chem. Rev.* **2016**, *116*, 11220-11289.

(28) Sánchez-Iglesias, A.; Grzelczak, M.; Altantzis, T.; Goris, B.; Pérez-Juste, J.; Bals, S.; Van Tendeloo, G.; Donaldson, S. H.; Chmelka, B. F.; Israelachvili, J. N.; Liz-Marzán, L. M. Hydrophobic Interactions Modulate Self-Assembly of Nanoparticles. *ACS Nano* **2012**, *6*, 11059-11065.

(29) Dutta, N.; Egorov, S.; Green, D. Quantification of Nanoparticle Interactions in Pure Solvents and a Concentrated PDMS Solution as a Function of Solvent Quality. *Langmuir* **2013**, *29*, 9991-10000.

(30) Rupich, S. M.; Shevchenko, E. V.; Bodnarchuk, M. I.; Lee, B.; Talapin, D. V. Size-Dependent Multiple Twinning in Nanocrystal Superlattices. *J. Am. Chem. Soc.* **2010**, *132*, 289-296.

(31) Talapin, D. V.; Shevchenko, E. V.; Kornowski, A.; Gaponik, N.; Haase, M.; Rogach, A. L.; Weller, H. A New Approach to Crystallization of CdSe Nanoparticles into Ordered Three-Dimensional Superlattices. *Adv. Mater.* **2001**, *13*, 1868-1871.

(32) Murray, C. B.; Kagan, C. R.; Bawendi, M. G. Self-Organization of CdSe Nanocrystallites into Three-Dimensional Quantum Dot Superlattices. *Science* **1995**, *270*, 1335-1338.

(33) Talapin, D. V.; Murray, C. B. PbSe Nanocrystal Solids for n- and p-Channel Thin Film Field-Effect Transistors. *Science* **2005**, *310*, 86-89.

(34) Shen, C.; Li, B.; Huang, Y.; Jin, Y. Kinetics of Coupled Primary- and Secondary-Minimum Deposition of Colloids under Unfavorable Chemical Conditions. *Environmental Science & Technology* **2007**, *41*, 6976-6982.

(35) Kosmulski, M. Positive Electrokinetic Charge of Silica in the Presence of Chlorides. *J. Colloid Interface Sci.* **1998**, *208*, 543-545.

(36) Dušak, P.; Mertelj, A.; Kralj, S.; Makovec, D. Controlled Heteroaggregation of Two Types of Nanoparticles in an Aqueous Suspension. *J. Colloid Interface Sci.* **2015**, *438*, 235-243.

(37) Gole, A.; Stone, J. W.; Gemmill, W. R.; zur Loye, H.-C.; Murphy, C. J. Iron Oxide Coated Gold Nanorods: Synthesis, Characterization, and Magnetic Manipulation. *Langmuir* **2008**, *24*, 6232-6237.

(38) Munshi, A. M.; Ho, D.; Saunders, M.; Agarwal, V.; Raston, C. L.; Iyer, K. S. Influence of Aspect Ratio of Magnetite Coated Gold Nanorods in Hydrogen Peroxide Sensing. *Sens. Actuators, B* **2016**, *235*, 492-497.

(39) Ziyang, L.; Yaqiong, Q.; Jianyong, F.; Jing, S.; Jun, L.; Fengqi, L.; Wensheng, Y. Monodisperse Magnetizable Silica Composite Particles from Heteroaggregate of Carboxylic Polystyrene Latex and Fe_3O_4 Nanoparticles. *Nanotechnology* **2008**, *19*, 055602.

(40) van Ewijk, G. A.; Philipse, A. P. Anomalous Attraction between Colloidal Magnetite and Silica Spheres in Apolar Solvents. *Langmuir* **2001**, *17*, 7204-7209.

(41) Pita, I. A.; Singh, S.; Silien, C.; Ryan, K. M.; Liu, N. Heteroaggregation assisted wet synthesis of core-shell silver-silica-cadmium selenide nanowires. *Nanoscale* **2016**, *8*, 1200-1209.

CHAPTER 5. Heteroaggregation Approach for Depositing Magnetite Nanoparticles onto Silica-Overcoated Gold Nanorods

5.1 Introduction

Composite nanoparticles (NPs) integrate multiple NPs into single units and are usually formed through seeded growth of one kind of NP onto another or through crosslinker molecules. By combining different kinds of NPs into composite NPs, multifunctional NPs with novel optical, magnetic, electronic, or catalytic properties can be obtained.[1-3] There are several approaches for synthesizing composite NPs, which can have a variety of sizes and morphologies, such as clusters, dendrites, chains, and sheets.[4] For some applications, it is desirable to make compact composite NPs by maximizing the loading of functional NPs and minimizing the amount of crosslinker or inert matrix material. Here, we demonstrate a simple heteroaggregation approach for depositing coatings of magnetite (Fe_3O_4) NPs onto the surface of silica-overcoated gold nanorods (SiO_2-GNRs), resulting in Fe_3O_4-SiO_2-GNRs, which maintain the longitudinal surface plasmon resonance (LSPR) of gold nanorods and are magnetically responsive. Fe_3O_4-SiO_2-GNRs are of special interest for biomedical applications because they are composed of biocompatible building blocks and are potentially useful for multimodal imaging or photothermal therapy with magnetic targeting. Heteroaggregation is a simple and versatile approach for assembling core/satellite NPs that is potentially widely applicable.

A common method for synthesizing core/satellite and core/shell NPs is seeded growth, where one inorganic phase is grown directly onto another,[5-30] which strongly depends on the composition of both phases, and heterogeneous nucleation of the satellite phase onto the core can be difficult to control. Moreover, seeded growth can require significant modifications to methods initially developed for homogeneous nucleation of the satellite phase to suppress homogeneous nucleation and provide primarily or exclusively heterogeneous nucleation.[10] Control over the size and morphology of the shell of satellite NPs is also often limited. A related method is mixing precursors for different elements and driving phase segregation by heating, which depends on the thermodynamics of the specific system.[31]

Another approach is assembly of presynthesized satellite NPs onto the surface of the core NP. This can allow more precise control over formation of the satellite NPs, for which synthetic methods are often already well established. Assembly of satellite NPs onto a core NP can be achieved using covalent crosslinkers, non-covalent interactions, and steric effects. Non-covalent interactions include van der Waals interactions from strong electrostatic interactions to weaker dipolar interactions, biological interactions, and π-π interactions.[32-38] Electrostatic attraction can be enhanced by selecting core and satellite NPs with opposite charges or by functionalizing them with opposite charges.[6,39,40] Covalent linkers are multifunctional molecules that can covalently bind to different types of NPs.[41-48] For steric effects to be significant, the coating on one type of NP must entrap the other type of NP or entangle its coating. Coatings designed for entrapment can be added in a step prior to

assembly, or coating and assembly can be performed simultaneously, where the coating material serves as the mortar to hold NPs together. Common coating materials for entrapment include polymers[49] and inorganic oxides obtained through sol-gel chemistry, such as silica (SiO_2).[43,50-53]

Several types of core/satellite NPs with gold nanorod (GNR) cores have been formed through seeded growth,[6,27] van der Waals interactions,[6,54] multifunctional molecules,[55-59] biomolecules,[26,60,61] and polymers,[56] but these methods are often limited by low-density coatings or non-uniform coverage. The native cetyltrimethylammonium bromide (CTAB) coating on GNRs is a challenge for functionalization of GNRs because CTAB is difficult to displace in aqueous environments,[62] and CTAB-stabilized GNRs are prone to agglomeration in non-aqueous solvents that can facilitate removal of CTAB. The CTAB coating on GNRs can be destabilized by increasing the salt concentration, decreasing the CTAB concentration, or changing the solvent composition.[63] These limitations of the CTAB coating can be overcome by depositing SiO_2 shells onto the GNRs, which also provides colloidal stability in methanol and ethanol. Our heteroaggregation approach for forming core/satellite Fe_3O_4-SiO_2-GNRs is based on upon the ability of SiO_2-GNRs to disperse in alcohols.

Aggregation occurs when colloids, including NPs, are destabilized, form flocs, and settle out of solution. During aggregation processes, an energy barrier that would prevent aggregation is lowered or overcome, allowing aggregation to occur.[64,65] In homoaggregation, particles of the same type flocculate, while heteroaggregation describes flocculation of different kinds of particles. Aggregation is a stochastic process, where particles collide with

one another, and if the attractive forces are strong enough or the barrier to aggregation is overcome, they remain bound together. In a binary particle system (A and B), three kinds of aggregation are possible, AA, BB, and AB. For stable colloidal suspensions, energy barriers prevent each kind of aggregation.[66,67] Manipulating the properties of the particles or their solvent environment can reduce or eliminate one or more of these barriers, thus driving aggregation.[68] If the barrier to AB aggregation is reduced or diminished while maintaining energy barriers for AA and BB aggregation, then heteroaggregation can occur selectively, without simultaneous homoaggregation.[69]

Multiple experimental levers are available for altering the energy barriers to aggregation. For example, removing stabilizing ligands from NPs can reduce the barrier to aggregation.[68] The solvent polarity can also be adjusted by adding a cosolvent with a different polarity that is miscible with the initial solvent, which can destabilize the dispersion.[70,71] The pH and salt concentration are also commonly used levers for controlling aggregation.[72,73] Moreover, the barrier to aggregation can be adjusted along a continuum by varying these parameters. Dramatically decreasing the barrier to aggregation can cause formation of fractal-like aggregates.[74] In many instances, a more controlled assembly process is desired, where a minor decrease in the barrier to aggregation drives slower aggregation, but with improved control.[75] It should also be noted that adjusting the conditions of the system may have different effects on AA, AB, and BB interactions, which could allow targeting of AA or BB homoaggregates or AB heteroaggregates.

We are aware of only two examples of heteroaggregation in non-aqueous systems, where NPs were not purposefully charged to drive heteroaggregation. We emphasize non-aqueous systems because we show that adjusting the composition of a solvent mixture is a highly effective means of controlling heteroaggregation. While charging NPs can be useful for self-assembly, we prefer milder conditions, and steric stabilization can be more effective at rendering NPs dispersible in different solvent environments. In one study, oleic acid-stabilized Fe_3O_4 NPs bound to the surfaces of larger SiO_2 NPs over the period of a month and yielded only 30% coverage of the SiO_2 surface.[32] In another study, CdSe and Au NPs stabilized with hydrophobic ligands were deposited on the surface of much larger SiO_2-coated Ag nanowires.[37] The extent of coverage was also limited, and heteroaggregation occurred over several weeks. These studies provide useful insights about heteroaggregation, but in both cases, the limited coverage and long assembly time were significant challenges. These are not intrinsic limitations, however, and we show that heteroaggregation can occur quickly and can give dense coatings. The key to achieving this improvement is to adjust the solvent conditions to properly control heteroaggregation, which was not explored in these prior studies.

Controlled assembly of Fe_3O_4-SiO_2-GNRs is achieved by inducing heteroaggregation via mixing of presynthesized Fe_3O_4 NPs and SiO_2-GNRs dispersed in non-polar (hexanes) and polar (ethanol) solvents, respectively. Fe_3O_4 NPs are deposited onto the surface of SiO_2-GNRs. Although others have produced similar GNR / Fe_3O_4 core/satellite NPs,[6,54-58] a major advantage of this method is its simplicity, speed (< 10 min), and potential generality. The

SiO_2 shell mediates the interaction between the core of the GNR and the Fe_3O_4 NPs, and no additional molecular crosslinker is employed. This heteroaggregation approach can likely be extended to other kinds of SiO_2-coated NPs or surfaces and NPs with hydrophobic ligands. The coatings of Fe_3O_4 NPs allow for manipulation of Fe_3O_4-SiO_2-GNRs with applied magnetic fields.

5.2 Experimental Section

Experimental methods for synthesizing SiO_2-GNRs,[76,77] Fe_3O_4 NPs,[78] and poly(ethyelene glycol) catechol (PEG-catechol)[79] have already been reported elsewhere. Details for these syntheses are provided in the Supporting Information.

5.2.1 Assembly of Fe_3O_4-SiO_2-GNRs

Hexanes (EMD, ACS, 98.5%) and anhydrous ethanol (Koptec, 99.5%) were used for assembly of Fe_3O_4-SiO_2-GNRs by driving heteroaggregation of Fe_3O_4 NPs and SiO_2-GNRs. The concentration of SiO_2-GNRs was 3.8 mg (measured as mg of Au) / mL of methanol, based on the assumption of 100% yields in the synthesis and purification of GNRs[76] and of SiO_2-GNRs.[77] This assumption is generally valid, because there is no apparent loss of material into the supernatant during centrifugation. 25 μL of SiO_2-GNRs in methanol was transferred into ethanol by dilution to 15 mL with ethanol. The dispersion was then centrifuged at 8,500 *g* (IEC Centra MP4 with 854 rotor) for 10 min and redispersed in 1 mL of ethanol, resulting in a final concentration of 0.095 mg/mL in ethanol. A 2-mL dispersion of Fe_3O_4 NPs in hexanes was prepared with a concentration of 1 mg/mL. These solutions, 1

mL of SiO_2-GNRs in ethanol and 2 mL of Fe_3O_4 NPs in hexanes, were then mixed with rapid stirring, followed by centrifugation at 2,500 *g* for 5 min. After removing the supernatant, the sedimented product was redispersed in hexanes. Fe_3O_4-SiO_2-GNRs can also be dispersed in other weakly polar solvents, such as toluene and tetrahydrofuran (THF). A cylindrical NdFeB permanent magnet (Bunting Magnetics, 1" diameter, 0.5" long, N35P1000500 for Figure 3a, 0.5" diameter, 0.5" long, N35P500500 for Figure 3b,c) was then placed next to the side of the glass vial to collect the Fe_3O_4-SiO_2-GNRs, leaving any excess free Fe_3O_4 NPs in the supernatant.

5.2.2 Functionalization of Fe_3O_4-SiO_2-GNRs with PEG-Catechol

Functionalization of Fe_3O_4-SiO_2-GNRs with PEG-catechol was conducted by adapting a method reported for functionalization of Fe_3O_4 NPs.[79] For PEGylation, Fe_3O_4-SiO_2-GNRs were first suspended in toluene by purifying Fe_3O_4-SiO_2-GNRs as described above but redispersing the product in the same volume of toluene instead of hexanes, resulting in the same concentration. The Fe_3O_4-SiO_2-GNRs in toluene were sonicated for 5 minutes to ensure they were well dispersed. PEG-catechol was dissolved in a small amount of toluene until reaching a final concentration of 0.1 mg/μL. This solution was mixed with the Fe_3O_4-SiO_2-GNRs at ratio of 2 mg of PEG-catechol per mg of SiO_2-GNRs. The mixture was then heated to 50 °C for two hours with gentle magnetic stirring. After cooling to room temperature, hexanes was added to drive flocculation, followed by centrifugation at low speed (2,500 *g*), removal of the supernatant, and allowing the solvent to completely evaporate under ambient atmosphere. The precipitate was then dispersed in deionized water

(Ricca, ACS Reagent grade, ASTM Type I, ASTM Type II) or anhydrous ethanol and briefly sonicated to drive dispersion of PEG-Fe_3O_4-SiO_2-GNRs.

5.2.3 Characterization

Transmission electron microscopy (TEM) was performed using a JEOL 2000FX microscope operated at 200 kV. Optical absorbance spectra were acquired with an Ocean Optics CHEM-USB-VIS-NIR spectrophotometer.

5.3 Results and Discussion

Heteroaggregation was performed using presynthesized CTAB-stabilized GNRs with core dimensions of 94 nm × 24 nm and a 19-nm thick mesoporous SiO_2 coating dispersed in ethanol (Figure 1a) and oleylamine-stabilized Fe_3O_4 NPs with a diameter of 7 nm (Figure 1b) dispersed in hexanes. Under optimized conditions, adding the SiO_2-GNRs in ethanol to the Fe_3O_4 NPs in hexanes yields a uniform coating of Fe_3O_4 NPs on the surface of the SiO_2-GNRs (Figure 1c). Fe_3O_4-SiO_2-GNRs can be assembled and purified by centrifugation in under 10 minutes. The uniformity of the coating of Fe_3O_4 NPs depends on many variables, including the concentration of Fe_3O_4 NPs and the ethanol to hexanes ratio. For too high concentrations of Fe_3O_4 NPs (> ~10 mg/mL prior to addition to the SiO_2-GNR solution), the Fe_3O_4 NPs undergo homoaggregation before binding to the SiO_2 surface, resulting in large clusters of Fe_3O_4 NPs bound to the surface of SiO_2-GNRs. If too much ethanol is used, the Fe_3O_4 NP coating loses its uniformity, and fractal-shaped aggregates form on the surface of the SiO_2-GNRs, or aggregates of Fe_3O_4-SiO_2-GNRs form (unpublished). It is important to

add the SiO_2-GNRs to the Fe_3O_4 NPs to avoid homoaggregation of the Fe_3O_4 NPs, which can occur if a small volume of hexanes containing Fe_3O_4 NPs is added to a much larger volume of SiO_2-GNRs in ethanol. The Fe_3O_4-SiO_2-GNR products from heteroaggregation can be purified by centrifugation or magnetic extraction. Fe_3O_4-SiO_2-GNRs disperse well in weakly polar solvents, such as hexanes, toluene, and THF, but do not disperse in ethanol, methanol, or water because the exterior surface of the Fe_3O_4-SiO_2-GNRs is coated with hydrophobic oleylamine ligands.

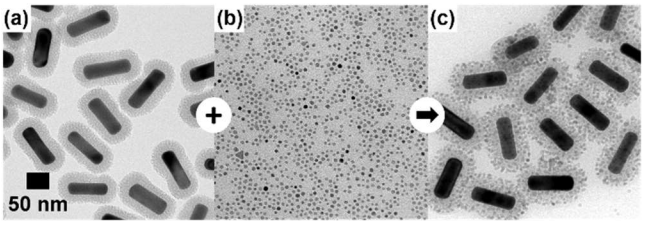

Figure 5.1 TEM images (common scale bar) of (a) SiO_2-GNRs with 19 nm SiO_2 shells, (b) 7-nm Fe_3O_4 NPs, and (c) Fe_3O_4-SiO_2-GNRs formed by heteroaggregation of Fe_3O_4 NPs onto SiO_2-GNRs.

5.3.1 Mechanism of Heteroaggregation

When Fe_3O_4 NPs dispersed in hexanes are mixed with SiO_2-GNRs dispersed in ethanol under optimized conditions, irreversible heteroaggregation occurs, while avoiding homoaggregation of Fe_3O_4 NPs or SiO_2-GNRs. Under these conditions, the barrier for heteroaggregation is lowered while maintaining the barriers for homoaggregation. As noted above, using a larger proportion of ethanol also reduced the barrier for homoaggregation of

Fe_3O_4 NPs, resulting in homoaggregation of Fe_3O_4 NPs. The dependence on the composition of the solvent mixture suggests the energy barrier for heteroaggregation is lower than for homoaggregation of Fe_3O_4 NPs, which may be rationalized by the relatively weak non-polar interactions between oleylamine-stabilized Fe_3O_4 NPs, in comparison with the stronger interactions with the polar surfaces of SiO_2-GNRs. The large size of the SiO_2-GNRs may also provide additional driving force for heteroaggregation, because the strength of van der Waals interactions increases as the size of the NPs increases. Homoaggregation of SiO_2-GNRs was not observed, which might be attributed to colloidal stability imparted by the SiO_2 shells or because the concentration of SiO_2-GNRs is much lower than that of the Fe_3O_4 NPs.

5.3.2 Optical Properties

Fe_3O_4 NPs absorb light at the blue end of the visible spectrum (Figure 2). This property is appealing for combining with SiO_2-GNRs, because there is minimal spectral overlap between Fe_3O_4 NPs and the LSPR of GNRs. Optical absorbance spectra of Fe_3O_4-SiO_2-GNRs show a redshift of 30 nm in the LSPR when the coating of Fe_3O_4 NPs is attached (Figure 2). This redshift is commonly observed when iron oxide NPs are deposited onto GNRs[12,54,55] and is attributed to the higher index of refraction of Fe_3O_4 (2.42)[80] than mesoporous SiO_2 (1.28-1.45).[81] In addition to the redshift, the absorbance broadened and decreased in intensity. Product loss during centrifugation could be responsible for at least part of the decrease in intensity. According to previous work, the higher dielectric constant of the Fe_3O_4 NPs can also cause the absorbance to broaden and be reduced in intensity.[54,55]

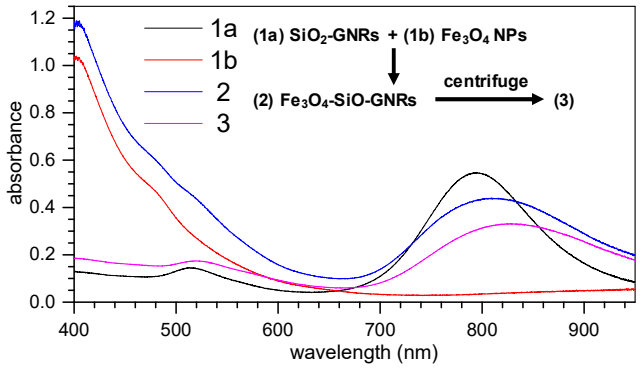

Figure 5.2 Optical absorbance spectra of the assembly and purification of (1a) SiO_2-GNRs in ethanol and (1b) Fe_3O_4 NPs in hexanes: (2) unpurified Fe_3O_4-SiO_2-GNRs upon mixing and (3) Fe_3O_4-SiO_2-GNRs after centrifugation and redispersion in hexanes. Note: The SiO_2-GNR stock solution was diluted with two volumes of ethanol for acquiring (1a), and the Fe_3O_4 NP stock solution was diluted with half a volume of hexanes for acquiring (1b). These dilutions were chosen to mimic mixing of the stock solutions at the 2:1 hexanes:ethanol volume ratio for heteroaggregation, (2). After centrifugation, the product was redispersed in the same volume of solvent as before purification for acquiring (3).

5.3.3 Magnetic Separation

Fe_3O_4-SiO_2-GNRs exhibit a strong magnetic response. When a permanent magnet is placed next to the dispersion of Fe_3O_4-SiO_2-GNRs, they collect on the wall of the vial next to the magnet (Figure 3a). The sedimented Fe_3O_4-SiO_2-GNRs readily redisperse with mild

sonication. For quantitative monitoring of the magnetic extraction process, a permanent magnet was placed next to the bottom of a cuvette containing Fe_3O_4-SiO_2-GNRs (Figure 3c). Optical absorbance spectra were collected every 5 minutes through the part of the solution at the top of the cuvette, from which Fe_3O_4-SiO_2-GNRs were depleted during magnetic extraction (Figure 3b). After 45 minutes, 85% of the Fe_3O_4-SiO_2-GNRs were removed from solution. A measurement after 120 minutes shows that 95% of the Fe_3O_4-SiO_2-GNRs have been removed.

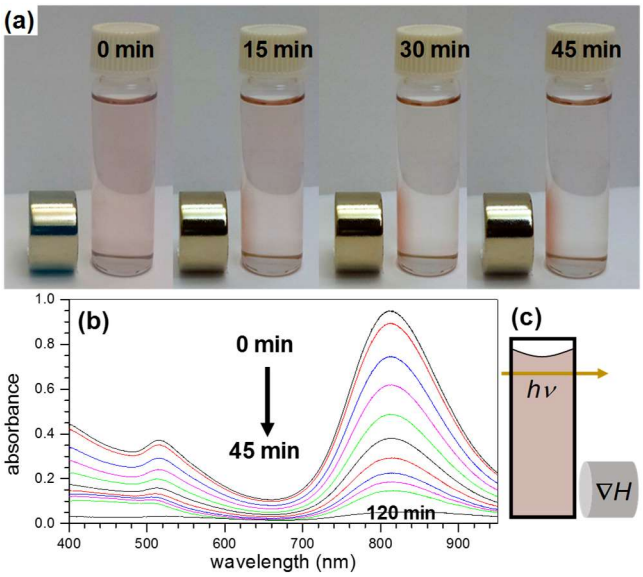

Figure 5.3 (a) Photos of the magnetic separation process conducted over 45 minutes. (b) Optical absorbance spectra of Fe_3O_4-SiO_2-GNRs remaining dispersed in hexanes in the top of the cuvette after placing a permanent magnet next to the bottom of the cuvette for magnetic separation. Spectra were collected in 5-minute intervals for 45 minutes, and an additional spectrum was acquired after 120 minutes. (c) Diagram of the arrangement of the cuvette,

magnet, and beam path for measurement of the residual dispersed Fe_3O_4-SiO_2-GNRs that are not pulled to the magnet.

5.3.4 Stability

A sample of Fe_3O_4-SiO_2-GNRs was repeatedly magnetically separated by redispersing the solids captured on the wall of the vial next to the magnet in fresh hexanes and sonicating to investigate the robustness of the coating of Fe_3O_4 NPs in Fe_3O_4-SiO_2-GNRs (Figure 4 and Supporting Information, Figure S1). An optical absorbance spectrum was acquired after each round of magnetic extraction and sonication. The spectra were normalized at 400 nm because Fe_3O_4 NPs and GNRs both contribute the absorbance at 400 nm (Figure 2). In the normalized absorbance spectra, the peak for the LSPR begins to broaden and increase in intensity starting after the third extraction and more substantially after the fifth extraction. The increase in peak height can be explained by loss of a small amount of Fe_3O_4 NPs from the surface of the Fe_3O_4-SiO_2-GNRs, because normalization at 400 nm combined with a decrease in the unnormalized absorbance at 400 nm causes an increase in the normalized absorbance at longer wavelengths. The unnormalized spectra also show decreased absorbance after each magnetic extraction step because the NPs adhere to the walls of the glass cuvette (Supporting Information, Figure S1). Broadening of the peak for the LSPR could result from agglomeration of Fe_3O_4-SiO_2-GNRs when some Fe_3O_4 NPs are removed from their surfaces or when some of the oleylamine ligands have been stripped away, because the hydrophobic surface coatings on the Fe_3O_4 NPs are required for maintaining dispersibility of Fe_3O_4-SiO_2-GNRs in hexanes.

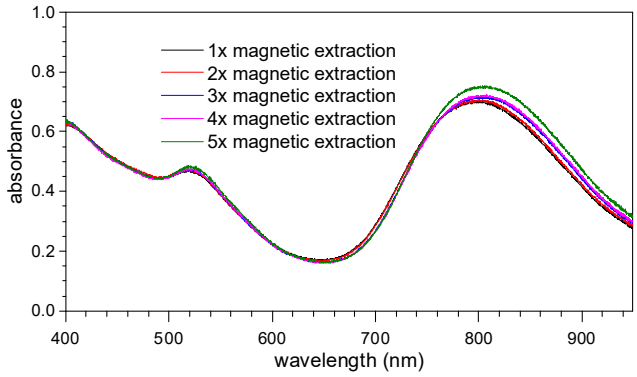

Figure 5.4 Optical absorbance spectra of Fe_3O_4-SiO_2-GNRs during five rounds of purification through magnetic extraction, normalized at 400 nm. Before acquiring each spectrum, the Fe_3O_4-SiO_2-GNRs were magnetically extracted using a permanent magnet. The supernatant was removed, and the sample was redispersed in a fixed volume of fresh hexanes and sonicated for 5 minutes.

5.3.5 Functionalization for Dispersion in Water

Oleylamine ligands stabilize the exposed surface of the Fe_3O_4 NPs, which makes Fe_3O_4-SiO_2-GNRs hydrophobic. Surface functionalization without removing the Fe_3O_4 NPs from the surface is needed for dispersing Fe_3O_4-SiO_2-GNRs in water for biomedical applications. The Fe_3O_4-SiO_2-GNRs were first transferred into toluene to confer miscibility with PEG-catechol, which was added to displace oleylamine and PEGylate the Fe_3O_4-SiO_2-GNRs, yielding PEG-Fe_3O_4-SiO_2-GNRs. The catechol group binds to the exposed Fe_3O_4 surface, and the PEG moiety provides stability in ethanol and water.[79] PEG-Fe_3O_4-SiO_2-GNRs form an aqueous dispersion that is stable for at least a month. Further experiments would be needed to assess their stability in buffers and biological environments. The optical

absorbance spectrum of PEG-Fe_3O_4-SiO_2-GNRs shows neither scattering nor a redshift that would be associated with agglomeration (Figure 5a and Supporting Information, Figure S2). Rather, the absorbance spectrum maintains the prominent absorption band of Fe_3O_4-SiO_2-GNRs prior to PEGylation and shows no sign of detachment of Fe_3O_4 NPs. There is a blueshift in the LSPR by 15 nm, which can be attributed to differences in the refractive index of toluene and water.[82] TEM of the PEG-Fe_3O_4-SiO_2-GNRs confirms that surface functionalization can be conducted without displacing the coating of Fe_3O_4 NPs (Figure 5c).

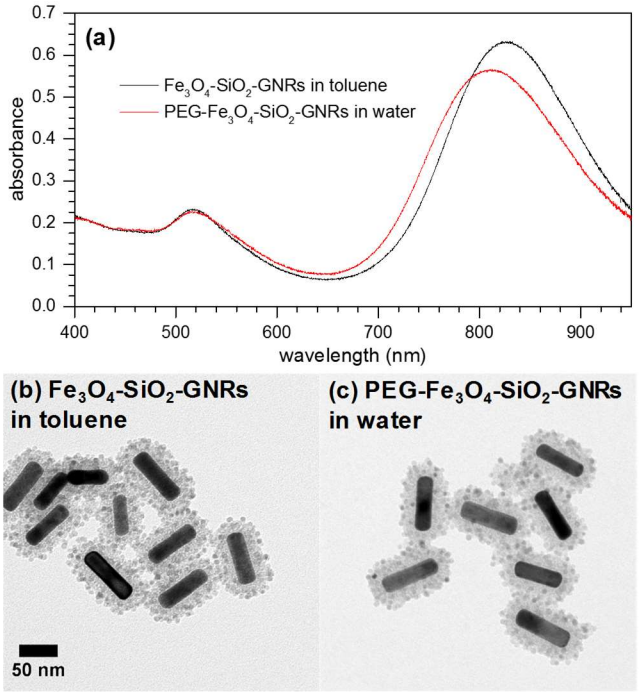

Figure 5.5 (a) Optical absorbance spectra, normalized at 400 nm, and TEM (common scale bar) of (b) Fe_3O_4-SiO_2-GNRs in toluene and (c) PEG-Fe_3O_4-SiO_2-GNRs in water.

5.4 Conclusions

By employing the well-known property of NPs stabilized by hydrophobic ligands to aggregate when exposed to polar non-solvents, we have developed a method for quickly inducing heteroaggregation of Fe_3O_4 NPs onto the surface of SiO_2-GNRs, resulting in Fe_3O_4-SiO_2-GNRs with a core/satellite morphology. By controlling the solvent polarity, uniform coatings of Fe_3O_4 NPs can be deposited onto the surface of SiO_2-GNRs within a few minutes of mixing and without requiring an additional crosslinker. This method is simple and fast because it uses presynthesized NPs, which allows independent control over the synthesis of the core and satellite NPs. Fe_3O_4-SiO_2-GNRs maintain the LSPR of the GNRs in the core and also exhibit strong responses to permanent magnets, thus allowing for magnetic manipulation and separations. Fe_3O_4-SiO_2-GNRs disperse in non-polar and weakly polar solvents, including hexanes, toluene, and THF. Surface functionalization with PEG-catechol renders them dispersible in water. Since many types of NPs are synthesized using hydrophobic ligands and there are methods for overcoating NPs with SiO_2, this technique could potentially be used to assemble a wide variety of core/satellite NPs. We anticipate this demonstration of a fast, non-aqueous heteroaggregation process will stimulate further work to apply heteroaggregation in other non-aqueous systems and to further investigate the mechanisms of heteroaggregation.

5.5 References

(1) Liu, X.; Iocozzia, J.; Wang, Y.; Cui, X.; Chen, Y.; Zhao, S.; Li, Z.; Lin, Z. Noble Metal-Metal Oxide Nanohybrids with Tailored Nanostructures for Efficient Solar Energy Conversion, Photocatalysis and Environmental Remediation. *Energy Environ. Sci.* **2017**, *10*, 402-434.

(2) Sahay, R.; Reddy, V. J.; Ramakrishna, S. Synthesis and Applications of Multifunctional Composite Nanomaterials. *Int. J. Mech. Mater. Eng.* **2014**, *9*, 25.

(3) Buck, M. R.; Schaak, R. E. Emerging Strategies for the Total Synthesis of Inorganic Nanostructures. *Angew. Chem., Int. Ed.* **2013**, *52*, 6154-6178.

(4) Nguyen, T.-D.; Tran, T.-H. Multicomponent Nanoarchitectures for the Design of Optical Sensing and Diagnostic Tools. *RSC Adv.* **2014**, *4*, 916-942.

(5) Lin, X.-M.; Samia, A. C. S. Synthesis, Assembly and Physical Properties of Magnetic Nanoparticles. *J. Magn. Magn. Mater.* **2006**, *305*, 100-109.

(6) Gole, A.; Stone, J. W.; Gemmill, W. R.; zur Loye, H.-C.; Murphy, C. J. Iron Oxide Coated Gold Nanorods: Synthesis, Characterization, and Magnetic Manipulation. *Langmuir* **2008**, *24*, 6232-6237.

(7) Shevchenko, E. V.; Bodnarchuk, M. I.; Kovalenko, M. V.; Talapin, D. V.; Smith, R. K.; Aloni, S.; Heiss, W.; Alivisatos, A. P. Gold/Iron Oxide Core/Hollow-Shell Nanoparticles. *Adv. Mater.* **2008**, *20*, 4323-4329.

(8) Wei, Y.; Klajn, R.; Pinchuk, A. O.; Grzybowski, B. A. Synthesis, Shape Control, and Optical Properties of Hybrid Au/Fe_3O_4 "Nanoflowers". *Small* **2008**, *4*, 1635-1639.

(9) Sheldon, M. T.; Trudeau, P.-E.; Mokari, T.; Wang, L.-W.; Alivisatos, A. P. Enhanced Semiconductor Nanocrystal Conductance via Solution Grown Contacts. *Nano Lett.* **2009**, *9*, 3676-3682.

(10) Carbone, L.; Cozzoli, P. D. Colloidal Heterostructured Nanocrystals: Synthesis and Growth Mechanisms. *Nano Today* **2010**, *5*, 449-493.

(11) Shore, M. S.; Wang, J.; Johnston-Peck, A. C.; Oldenburg, A. L.; Tracy, J. B. Synthesis of Au(Core)/Ag(Shell) Nanoparticles and their Conversion to AuAg Alloy Nanoparticles. *Small* **2011**, *7*, 230-234.

(12) Zhai, Y.; Han, L.; Wang, P.; Li, G.; Ren, W.; Liu, L.; Wang, E.; Dong, S. Superparamagnetic Plasmonic Nanohybrids: Shape-Controlled Synthesis, TEM-Induced

Structure Evolution, and Efficient Sunlight-Driven Inactivation of Bacteria. *ACS Nano* **2011**, *5*, 8562-8570.

(13) Hill, L. J.; Bull, M. M.; Sung, Y.; Simmonds, A. G.; Dirlam, P. T.; Richey, N. E.; DeRosa, S. E.; Shim, I.-B.; Guin, D.; Costanzo, P. J.; Pinna, N.; Willinger, M.-G.; Vogel, W.; Char, K.; Pyun, J. Directing the Deposition of Ferromagnetic Cobalt onto Pt-Tipped CdSe@CdS Nanorods: Synthetic and Mechanistic Insights. *ACS Nano* **2012**, *6*, 8632-8645.

(14) Xu, Y.; Lian, J.; Mishra, N.; Chan, Y. Multifunctional Semiconductor Nanoheterostructures via Site-Selective Silica Encapsulation. *Small* **2013**, *9*, 1908-1915.

(15) Gao, C.; Goebl, J.; Yin, Y. Seeded Growth Route to Noble Metal Nanostructures. *J. Mater. Chem. C* **2013**, *1*, 3898-3909.

(16) Banin, U.; Ben-Shahar, Y.; Vinokurov, K. Hybrid Semiconductor–Metal Nanoparticles: From Architecture to Function. *Chem. Mater.* **2014**, *26*, 97-110.

(17) Zhou, H.; Kim, J.-P.; Bahng, J. H.; Kotov, N. A.; Lee, J. Self-Assembly Mechanism of Spiky Magnetoplasmonic Supraparticles. *Adv. Funct. Mater.* **2014**, *24*, 1439-1448.

(18) Straney, P. J.; Marbella, L. E.; Andolina, C. M.; Nuhfer, N. T.; Millstone, J. E. Decoupling Mechanisms of Platinum Deposition on Colloidal Gold Nanoparticle Substrates. *J. Am. Chem. Soc.* **2014**, *136*, 7873-7876.

(19) Yu, S.; Hachtel, J. A.; Chisholm, M. F.; Pantelides, S. T.; Laromaine, A.; Roig, A. Magnetic Gold Nanotriangles by Microwave-Assisted Polyol Synthesis. *Nanoscale* **2015**, *7*, 14039-14046.

(20) Weiner, R. G.; Kunz, M. R.; Skrabalak, S. E. Seeding a New Kind of Garden: Synthesis of Architecturally Defined Multimetallic Nanostructures by Seed-Mediated Co-Reduction. *Acc. Chem. Res.* **2015**, *48*, 2688-2695.

(21) Hernández-Pagán, E. A.; Leach, A. D. P.; Rhodes, J. M.; Sarkar, S.; Macdonald, J. E. A Synthetic Exploration of Metal–Semiconductor Hybrid Particles of $CuInS_2$. *Chem. Mater.* **2015**, *27*, 7969-7976.

(22) Pavlopoulos, N. G.; Dubose, J. T.; Pinna, N.; Willinger, M.-G.; Char, K.; Pyun, J. Synthesis and Assembly of Dipolar Heterostructured Tetrapods: Colloidal Polymers with "Giant *tert*-butyl" Groups. *Angew. Chem., Int. Ed.* **2016**, *55*, 1787-1791.

(23) Pang, B.; Zhao, Y.; Luehmann, H.; Yang, X.; Detering, L.; You, M.; Zhang, C.; Zhang, L.; Li, Z.-Y.; Ren, Q.; Liu, Y.; Xia, Y. ^{64}Cu-Doped PdCu@Au Tripods: A Multifunctional Nanomaterial for Positron Emission Tomography and Image-Guided Photothermal Cancer Treatment. *ACS Nano* **2016**, *10*, 3121-3131.

(24) Nakibli, Y.; Amirav, L. Selective Growth of Ni Tips on Nanorod Photocatalysts. *Chem. Mater.* **2016**, *28*, 4524-4527.

(25) Gilroy, K. D.; Ruditskiy, A.; Peng, H.-C.; Qin, D.; Xia, Y. Bimetallic Nanocrystals: Syntheses, Properties, and Applications. *Chem. Rev.* **2016**, *116*, 10414-10472.

(26) Su, X.; Fu, B.; Yuan, J. Gold Nanocluster-Coated Gold Nanorods for Simultaneously Enhanced Photothermal Performance and Stability. *Mater. Lett.* **2017**, *188*, 111-114.

(27) Li, Y.; Zhao, J.; You, W.; Cheng, D.; Ni, W. Gold Nanorod@Iron Oxide Core-Shell Heterostructures: Synthesis, Characterization, and Photocatalytic Performance. *Nanoscale* **2017**, *9*, 3925-3933.

(28) Marusak, K. E.; Johnston-Peck, A. C.; Wu, W.-C.; Anderson, B. D.; Tracy, J. B. Size and Composition Control of CoNi Nanoparticles and Their Conversion into Phosphides. *Chem. Mater.* **2017**, *29*, 2739-2747.

(29) Reguera, J.; Jiménez de Aberasturi, D.; Henriksen-Lacey, M.; Langer, J.; Espinosa, A.; Szczupak, B.; Wilhelm, C.; Liz-Marzán, L. M. Janus Plasmonic-Magnetic Gold-Iron Oxide Nanoparticles as Contrast Agents for Multimodal Imaging. *Nanoscale* **2017**, *9*, 9467-9480.

(30) Zhan, W.; Wang, J.; Wang, H.; Zhang, J.; Liu, X.; Zhang, P.; Chi, M.; Guo, Y.; Guo, Y.; Lu, G.; Sun, S.; Dai, S.; Zhu, H. Crystal Structural Effect of AuCu Alloy Nanoparticles on Catalytic CO Oxidation. *J. Am. Chem. Soc.* **2017**, *139*, 8846-8854.

(31) Chen, P.-C.; Liu, X.; Hedrick, J. L.; Xie, Z.; Wang, S.; Lin, Q.-Y.; Hersam, M. C.; Dravid, V. P.; Mirkin, C. A. Polyelemental Nanoparticle Libraries. *Science* **2016**, *352*, 1565-1569.

(32) van Ewijk, G. A.; Philipse, A. P. Anomalous Attraction between Colloidal Magnetite and Silica Spheres in Apolar Solvents. *Langmuir* **2001**, *17*, 7204-7209.

(33) Kalsin, A. M.; Pinchuk, A. O.; Smoukov, S. K.; Paszewski, M.; Schatz, G. C.; Grzybowski, B. A. Electrostatic Aggregation and Formation of Core−Shell Suprastructures in Binary Mixtures of Charged Metal Nanoparticles. *Nano Lett.* **2006**, *6*, 1896-1903.

(34) Yeap, S. P.; Toh, P. Y.; Ahmad, A. L.; Low, S. C.; Majetich, S. A.; Lim, J. Colloidal Stability and Magnetophoresis of Gold-Coated Iron Oxide Nanorods in Biological Media. *J. Phys. Chem. C* **2012**, *116*, 22561-22569.

(35) Caputo, G.; Pinna, N. Nanoparticle Self-Assembly Using π-π Interactions. *J. Mater. Chem. A* **2013**, *1*, 2370-2378.

(36) Essinger-Hileman, E. R.; Popczun, E. J.; Schaak, R. E. Magnetic Separation of Colloidal Nanoparticle Mixtures Using a Material Specific Peptide. *Chem. Commun.* **2013**, *49*, 5471-5473.

(37) Pita, I. A.; Singh, S.; Silien, C.; Ryan, K. M.; Liu, N. Heteroaggregation Assisted Wet Synthesis of Core-Shell Silver-Silica-Cadmium Selenide Nanowires. *Nanoscale* **2016**, *8*, 1200-1209.

(38) Kister, T.; Mravlak, M.; Schilling, T.; Kraus, T. Pressure-Controlled Formation of Crystalline, Janus, and Core-Shell Supraparticles. *Nanoscale* **2016**, *8*, 13377-13384.

(39) Lu, Z.; Qin, Y.; Fang, J.; Sun, J.; Li, J.; Liu, F.; Yang, W. Monodisperse Magnetizable Silica Composite Particles from Heteroaggregate of Carboxylic Polystyrene Latex and Fe_3O_4 Nanoparticles. *Nanotechnology* **2008**, *19*, 055602.

(40) Munshi, A. M.; Ho, D.; Saunders, M.; Agarwal, V.; Raston, C. L.; Iyer, K. S. Influence of Aspect Ratio of Magnetite Coated Gold Nanorods in Hydrogen Peroxide Sensing. *Sens. Actuators, B* **2016**, *235*, 492-497.

(41) Liu, N.; Prall, B. S.; Klimov, V. I. Hybrid Gold/Silica/Nanocrystal-Quantum-Dot Superstructures: Synthesis and Analysis of Semiconductor-Metal Interactions. *J. Am. Chem. Soc.* **2006**, *128*, 15362-15363.

(42) Guo, S.; Dong, S.; Wang, E. A General Route to Construct Diverse Multifunctional Fe_3O_4/Metal Hybrid Nanostructures. *Chem. Eur. J.* **2009**, *15*, 2416-2424.

(43) Lu, Z.; Gao, C.; Zhang, Q.; Chi, M.; Howe, J. Y.; Yin, Y. Direct Assembly of Hydrophobic Nanoparticles to Multifunctional Structures. *Nano Lett.* **2011**, *11*, 3404-3412.

(44) Yin, N.; Jiang, T.; Yu, J.; He, J.; Li, X.; Huang, Q.; Liu, L.; Xu, X.; Zhu, L. Study of Gold Nanostar@SiO_2@CdTeS Quantum Dots@SiO_2 with Enhanced-Fluorescence and Photothermal Therapy Multifunctional Cell Nanoprobe. *J. Nanopart. Res.* **2014**, *16*, 2306.

(45) Jeoung, E.; Yeh, Y.-C.; Nelson, T.; Kushida, T.; Wang, L.-S.; Mout, R.; Li, X.; Saha, K.; Gupta, A.; Tonga, G. Y.; Lannutti, J. J.; Rotello, V. M. Fabrication of Functional Nanofibers Through Post-Nanoparticle Functionalization. *Macromol. Rapid Commun.* **2015**, *36*, 678-683.

(46) Ertem, E.; Murillo-Cremaes, N.; Carney, R. P.; Laromaine, A.; Janecek, E.-R.; Roig, A.; Stellacci, F. A Silica-Based Magnetic Platform Decorated with Mixed Ligand Gold Nanoparticles: A Recyclable Catalyst for Esterification Reactions. *Chem. Commun.* **2016**, *52*, 5573-5576.

(47) Höller, R. P. M.; Dulle, M.; Thomä, S.; Mayer, M.; Steiner, A. M.; Förster, S.; Fery, A.; Kuttner, C.; Chanana, M. Protein-Assisted Assembly of Modular 3D Plasmonic Raspberry-Like Core/Satellite Nanoclusters: Correlation of Structure and Optical Properties. *ACS Nano* **2016**, *10*, 5740-5750.

(48) Zhang, M.; Magagnosc, D. J.; Liberal, I.; Yu, Y.; Yun, H.; Yang, H.; Wu, Y.; Guo, J.; Chen, W.; Shin, Y. J.; Stein, A.; Kikkawa, J. M.; Engheta, N.; Gianola, D. S.; Murray, C. B.; Kagan, C. R. High-Strength Magnetically Switchable Plasmonic Nanorods Assembled from a Binary Nanocrystal Mixture. *Nat. Nanotechnol.* **2017**, *12*, 228-232.

(49) Cha, J.; Cui, P.; Lee, J.-K. A Simple Method to Synthesize Multifunctional Silica Nanocomposites, NPs@SiO_2, Using Polyvinylpyrrolidone (PVP) as a Mediator. *J. Mater. Chem.* **2010**, *20*, 5533-5537.

(50) Chan, Y.; Zimmer, J. P.; Stroh, M.; Steckel, J. S.; Jain, R. K.; Bawendi, M. G. Incorporation of Luminescent Nanocrystals into Monodisperse Core-Shell Silica Microspheres. *Adv. Mater.* **2004**, *16*, 2092-2097.

(51) Yi, D. K.; Selvan, S. T.; Lee, S. S.; Papaefthymiou, G. C.; Kundaliya, D.; Ying, J. Y. Silica-Coated Nanocomposites of Magnetic Nanoparticles and Quantum Dots. *J. Am. Chem. Soc.* **2005**, *127*, 4990-4991.

(52) Insin, N.; Tracy, J. B.; Lee, H.; Zimmer, J. P.; Westervelt, R. M.; Bawendi, M. G. Incorporation of Iron Oxide Nanoparticles and Quantum Dots into Silica Microspheres. *ACS Nano* **2008**, *2*, 197-202.

(53) Chen, O.; Riedemann, L.; Etoc, F.; Herrmann, H.; Coppey, M.; Barch, M.; Farrar, C. T.; Zhao, J.; Bruns, O. T.; Wei, H.; Guo, P.; Cui, J.; Jensen, R.; Chen, Y.; Harris, D. K.; Cordero, J. M.; Wang, Z.; Jasanoff, A.; Fukumura, D.; Reimer, R.; Dahan, M.; Jain, R. K.; Bawendi, M. G. Magneto-Fluorescent Core-Shell Supernanoparticles. *Nat. Commun.* **2014**, *5*, 5093.

(54) Truby, R. L.; Emelianov, S. Y.; Homan, K. A. Ligand-Mediated Self-Assembly of Hybrid Plasmonic and Superparamagnetic Nanostructures. *Langmuir* **2013**, *29*, 2465-2470.

(55) Wang, C.; Chen, J.; Talavage, T.; Irudayaraj, J. Gold Nanorod/Fe_3O_4 Nanoparticle "Nano-Pearl-Necklaces" for Simultaneous Targeting, Dual-Mode Imaging, and Photothermal Ablation of Cancer Cells. *Angew. Chem., Int. Ed.* **2009**, *48*, 2759-2763.

(56) Basiruddin, S. K.; Maity, A. R.; Saha, A.; Jana, N. R. Gold-Nanorod-Based Hybrid Cellular Probe with Multifunctional Properties. *J. Phys. Chem. C* **2011**, *115*, 19612-19620.

(57) Ramasamy, M.; Lee, S. S.; Yi, D. K.; Kim, K. Magnetic, Optical Gold Nanorods for Recyclable Photothermal Ablation of Bacteria. *J. Mater. Chem. B* **2014**, *2*, 981-988.

(58) Zhang, H.; Sun, Y.; Gao, S.; Zhang, H.; Zhang, J.; Bai, Y.; Song, D. Studies of Gold Nanorod-Iron Oxide Nanohybrids for Immunoassay Based on SPR Biosensor. *Talanta* **2014**, *125*, 29-35.

(59) Fan, Z.; Tebbe, M.; Fery, A.; Agarwal, S.; Greiner, A. Assembly of Gold Nanoparticles on Gold Nanorods Using Functionalized Poly(N-isopropylacrylamide) as Polymeric "Glue". *Part. Part. Syst. Charact.* **2016**, *33*, 698-702.

(60) Wu, X.; Gao, F.; Xu, L.; Kuang, H.; Wang, L.; Xu, C. A Fluorescence Active Gold Nanorod-Quantum Dot Core-Satellite Nanostructure for Sub-Attomolar Tumor Marker Biosensing. *RSC Adv.* **2015**, *5*, 97898-97902.

(61) Raeesi, V.; Chou, L. Y. T.; Chan, W. C. W. Tuning the Drug Loading and Release of DNA-Assembled Gold-Nanorod Superstructures. *Adv. Mater.* **2016**, *28*, 8511-8518.

(62) Hore, M. J. A.; Ye, X.; Ford, J.; Gao, Y.; Fei, J.; Wu, Q.; Rowan, S. J.; Composto, R. J.; Murray, C. B.; Hammouda, B. Probing the Structure, Composition, and Spatial Distribution of Ligands on Gold Nanorods. *Nano Lett.* **2015**, *15*, 5730-5738.

(63) Vigderman, L.; Khanal, B. P.; Zubarev, E. R. Functional Gold Nanorods: Synthesis, Self-Assembly, and Sensing Applications. *Adv. Mater.* **2012**, *24*, 4811-4841.

(64) Verwey, E. J. W. Theory of the Stability of Lyophobic Colloids. *J. Phys. Colloid Chem.* **1947**, *51*, 631-636.

(65) Derjaguin, B.; Landau, L. Theory of the Stability of Strongly Charged Lyophobic Sols and of the Adhesion of Strongly Charged Particles in Solutions of Electrolytes. *Prog. Surf. Sci.* **1993**, *43*, 30-59.

(66) Pugh, R. J. Selective Coagulation of Colloidal Mineral Particles. In *Colloid Chemistry in Mineral Processing*, 1992; Vol. 12, pp 268-271.

(67) Wang, H.; Adeleye, A. S.; Huang, Y.; Li, F.; Keller, A. A. Heteroaggregation of Nanoparticles with Biocolloids and Geocolloids. *Adv. Colloid Interface Sci.* **2015**, *226, Part A*, 24-36.

(68) Stolarczyk, J. K.; Deak, A.; Brougham, D. F. Nanoparticle Clusters: Assembly and Control Over Internal Order, Current Capabilities, and Future Potential. *Adv. Mater.* **2016**, *28*, 5400-5424.

(69) Snoswell, D. R. E.; Duan, J.; Fornasiero, D.; Ralston, J. The Selective Aggregation and Separation of Titania from a Mixed Suspension of Silica and Titania. *Int. J. Miner. Process.* **2005**, *78*, 1-10.

(70) Dutta, N.; Egorov, S.; Green, D. Quantification of Nanoparticle Interactions in Pure Solvents and a Concentrated PDMS Solution as a Function of Solvent Quality. *Langmuir* **2013**, *29*, 9991-10000.

(71) Kislenko, S. A.; Kislenko, V. A.; Razumov, V. F. The Effects of a Solvent and a Ligand Shell on Interaction of CdSe Quantum Dots: Molecular Dynamics Simulation. *Colloid J.* **2015**, *77*, 727-732.

(72) Shen, C.; Li, B.; Huang, Y.; Jin, Y. Kinetics of Coupled Primary- and Secondary-Minimum Deposition of Colloids under Unfavorable Chemical Conditions. *Environ. Sci. Technol.* **2007**, *41*, 6976-6982.

(73) Dušak, P.; Mertelj, A.; Kralj, S.; Makovec, D. Controlled Heteroaggregation of Two Types of Nanoparticles in an Aqueous Suspension. *J. Colloid Interface Sci.* **2015**, *438*, 235-243.

(74) Asnaghi, D.; Carpineti, M.; Giglio, M.; Sozzi, M. Coagulation Kinetics and Aggregate Morphology in the Intermediate Regimes Between Diffusion-Limited and Reaction-Limited Cluster Aggregation. *Phys. Rev. A* **1992**, *45*, 1018-1023.

(75) Lin, M. Y.; Lindsay, H. M.; Weitz, D. A.; Ball, R. C.; Klein, R.; Meakin, P. Universal Reaction-Limited Colloid Aggregation. *Phys. Rev. A* **1990**, *41*, 2005-2020.

(76) Kozek, K. A.; Kozek, K. M.; Wu, W.-C.; Mishra, S. R.; Tracy, J. B. Large-Scale Synthesis of Gold Nanorods through Continuous Secondary Growth. *Chem. Mater.* **2013**, *25*, 4537-4544.

(77) Wu, W.-C.; Tracy, J. B. Large-Scale Silica Overcoating of Gold Nanorods with Tunable Shell Thicknesses. *Chem. Mater.* **2015**, *27*, 2888-2894.

(78) Xu, Z.; Shen, C.; Hou, Y.; Gao, H.; Sun, S. Oleylamine as Both Reducing Agent and Stabilizer in a Facile Synthesis of Magnetite Nanoparticles. *Chem. Mater.* **2009**, *21*, 1778-1780.

(79) Li, Q.; Barrett, D. G.; Messersmith, P. B.; Holten-Andersen, N. Controlling Hydrogel Mechanics via Bio-Inspired Polymer-Nanoparticle Bond Dynamics. *ACS Nano* **2016**, *10*, 1317-1324.

(80) Patnaik, P. *Handbook of Inorganic Chemicals*. McGraw-Hill: New York, 2003.

(81) Brinker, C. J.; Scherer, G. W. *Sol-Gel Science: The Physics and Chemistry of Sol-Gel Processing*. Academic Press: Boston, 1990.

(82) Chen, H.; Kou, X.; Yang, Z.; Ni, W.; Wang, J. Shape- and Size-Dependent Refractive Index Sensitivity of Gold Nanoparticles. *Langmuir* **2008**, *24*, 5233-5237.

5.6 Supporting Information

5.6.1 Chemicals for Nanoparticle Synthesis, Purification, and Heteroaggregation

$HAuCl_4 \cdot xH_2O$ (Alfa Aesar, 99.999%, where *x* was estimated as 3), cetyltrimethylammonium bromide (CTAB, Amresco, 99%), $AgNO_3$ (Alfa Aesar, 99.9995%), ascorbic acid (JT Baker, 99.5%), KBr (Alfa Aesar, ACS, 99% min), deionized water (Ricca, ACS Reagent grade, ASTM Type I, ASTM Type II), $NaBH_4$ (Sigma-Aldrich, 99%, 213462), tetraethyl orthosilicate (TEOS, Alfa Aesar, 99.9%), anhydrous methanol for diluting TEOS (EMD, DriSolv), methanol for SiO_2-GNR purification (Macron, UltimAR), NaOH (Sigma-Aldrich, 99%), anhydrous ethanol (Koptec, 99.5%), oleylamine (Sigma-Aldrich, 98% primary amine), hexanes (EMD, ACS, 98.5%), toluene (JT Baker, CMOS), benzyl ether (Acros, 99%), $Fe(acac)_3$ (Strem, 99%), and tetrahydrofuran (THF, EMD, OmniSolv, Non-UV) were used for synthesizing, purifying, and conducting heteroaggregation of SiO_2-GNRs and Fe_3O_4 NPs and for dispersing the product, Fe_3O_4-SiO_2-GNRs.

5.6.2 Synthesis of SiO_2-GNRs

CTAB-stabilized gold nanorods (GNRs) were synthesized using a seed-mediated approach.[1] This method produced 1 L of aqueous GNRs containing 100 mM CTAB and 190 mg of GNRs at a concentration of ~0.8 nM. A secondary injection of ascorbic acid was used to reduce and deposit the residual Au precursor onto the surface of the GNRs. To prepare the

GNRs for overcoating with SiO_2,[2] 100 mL of the product was warmed to 28 °C and then centrifuged twice at 14,200 *g* (IEC Centra MP4 with 854 rotor). By following the established purification procedure, the final GNR concentration was increased 10-fold in a final volume of 10 mL, and the CTAB concentration was ~1 mM.[2]

The concentrated GNRs were heated to 30 °C in a water bath, and the pH was increased to 10.4 by slowly adding 0.1 M NaOH. 250 μL of 20% TEOS in anhydrous methanol was then injected into the GNRs by syringe pump at a rate to 50 μL/min, while stirring at 150 rpm. After completing the injection, the stir rate was adjusted to 30 rpm for 30 min. The mixture was then left still for 20 hours, without stirring. Upon completing the reaction, the mixture was immediately divided equally among four 40-mL centrifuge tubes. The contents of each tube were diluted to 40 mL with methanol and centrifuged at 8,500 *g* for 10 min. This dilution and centrifugation process was repeated five times, with removal of the supernatant, redispersion of the SiO_2-GNRs in fresh methanol, and sonication between runs. The final product was stored in methanol at a concentration of 3.8 mg/mL by dilution to a final volume of 5 mL with methanol.

5.6.3 Synthesis of Fe_3O_4 NPs

Oleylamine-stabilized Fe_3O_4 NPs with an average diameter of 7 nm were synthesized by scaling up a heat-up method.[3] 3.12 g of $Fe(acac)_3$ was mixed with 45 mL of benzyl ether and 45 mL of oleylamine in a 250-mL, three-necked, round-bottomed flask equipped with a condenser, thermocouple, and rubber septum. The condenser was then connected to a

vacuum and inert gas manifold, and the system was placed under vacuum for 1 hour at room temperature, followed by heating to 90 °C, backfilling with N_2, and then heating to 120 °C for 1 hour. The temperature was then ramped (at a rate of ~15 °C/min) to 290 °C and held for 1 hour. Upon cooling to room temperature, the product was purified by centrifugation by adding an equal volume of ethanol to the product and centrifuging at 2,500 *g*, followed by redispersion in hexanes for storage.

5.6.4. Synthesis and Purification of PEG-Catechol

5.6.4.1 Chemicals for Synthesis of PEG-Catechol

Methoxypoly(ethylene glycol) acetic acid (mPEG-CM, Laysan Bio, Inc., MW = 2 kDa), dopamine hydrochloride (Sigma-Aldrich), *N,N,N',N'*-tetramethyl-*O*-(1*H*-benzotriazol-1-yl)uronium hexafluorophosphate (HBTU, Sigma-Aldrich, ≥98.0%), 1-hydroxybenzotriazole hydrate (HOBt, Sigma-Aldrich, 97%), triethylamine (TEA, Sigma-Aldrich, ≥99%), dichloromethane (DCM, Sigma-Aldrich, anhydrous, ≥99.8%), *N,N*-dimethylformamide (DMF, Sigma-Aldrich, anhydrous, 99.8%), diethyl ether (Et_2O, Sigma-Aldrich, anhydrous, ≥99.7%), chloroform ($CHCl_3$, Sigma-Aldrich, ≥99.5%), sodium sulfate (Na_2SO_4, Sigma-Aldrich, ≥99.0%, anhydrous), and hydrochloric acid (HCl, Sigma-Aldrich, 37%) were used for the synthesis and purification of PEG-catechol.

5.6.4.2 Synthesis and Purification of PEG-Catechol

PEG-catechol was synthesized by modifying a commercially available PEG-COOH.[4] Briefly, 500 mg (0.19 mmol) of mPEG-CM was dissolved in 6 mL of a 2:1 (v/v) solution of DCM and DMF. 72 mg (0.38 mmol) of dopamine hydrochloride and 90 mg (0.67 mmol) of HOBt were then added, and N_2 was bubbled through the mixture for 15 min. 153 mg (0.38 mmol) of HBTU and 100 μL (0.66 mmol) of TEA were added, and the mixture was stirred under N_2 atmosphere at room temperature overnight. The solution volume was reduced by rotary evaporation, followed by acidification by adding 10 mL of 1 M HCl with mixing. The aqueous solution was extracted with 10 mL of $CHCl_3$ three times. The organic phase was then collected and dried with Na_2SO_4. After the solution was concentrated to <2 mL by rotary evaporation, it was precipitated with 30 mL of cold Et_2O at −20 °C. The crude product (white precipitate) was purified by redissolving in ∼2 mL of DCM and precipitation in 30 mL of cold Et_2O at −20 °C two more times. The precipitate was finally redissolved in H_2O and lyophilized. The final purified PEG-catechol was obtained as a white solid powder and stored at −20 °C until needed. ^{1}H NMR (D_2O) δ (ppm): 6.7−6.8 (m, 3H, aromatic), 3.3−4.0 (m, −O−C**H₂**−C**H₂**−), 3.4 (t, 2H, CH_2 adjacent to aromatic ring), 2.7 (t, 2H, −C**H₂**−NH−CO−).

5.6.5 Unnormalized Optical Absorbance Spectra

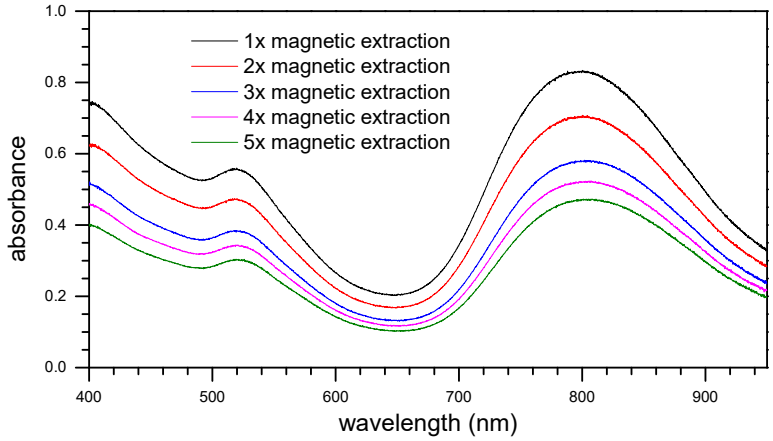

Figure 5.6 Unnormalized optical absorbance spectra of Fe_3O_4-SiO_2-GNRs during five rounds of purification through magnetic extraction. The normalized version of these spectra is provided in the main text, Figure 4.

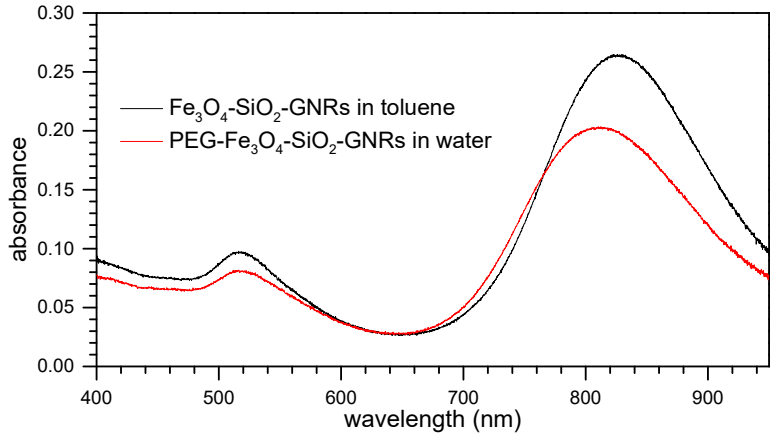

Figure 5.7 Unnormalized optical absorbance spectra of Fe_3O_4-SiO_2-GNRs in toluene and PEG-Fe_3O_4-SiO_2-GNRs in water. The normalized version of these spectra is provided in the main text, Figure 5.

5.7 References

(1) Kozek, K. A.; Kozek, K. M.; Wu, W.-C.; Mishra, S. R.; Tracy, J. B. Large-Scale Synthesis of Gold Nanorods through Continuous Secondary Growth. *Chem. Mater.* **2013**, *25*, 4537-4544.

(2) Wu, W.-C.; Tracy, J. B. Large-Scale Silica Overcoating of Gold Nanorods with Tunable Shell Thicknesses. *Chem. Mater.* **2015**, *27*, 2888-2894.

(3) Xu, Z.; Shen, C.; Hou, Y.; Gao, H.; Sun, S. Oleylamine as Both Reducing Agent and Stabilizer in a Facile Synthesis of Magnetite Nanoparticles. *Chem. Mater.* **2009**, *21*, 1778-1780.

(4) Li, Q.; Barrett, D. G.; Messersmith, P. B.; Holten-Andersen, N. Controlling Hydrogel Mechanics via Bio-Inspired Polymer-Nanoparticle Bond Dynamics. *ACS Nano* **2016**, *10*, 1317-1324.

CHAPTER 6. Direct Electrospinning of Titania Fibers with Ethanol

6.1 Introduction

Nanoscale ceramic fibers are of interest for their high surface-area-to-volume ratio and have widespread applications, including electronics, sensors, and catalysis.[1,2] Titania (TiO_2), in particular, has shown promise as a catalyst for photocatalytic water splitting and environmental remediation when in its anatase phase.[3] Here, we report electrospinning of TiO_2 nanofibers with average diameters below 100 nm and without use of a polymer additive. To the best of our knowledge, this is the smallest diameter TiO_2 fibers obtained to date, where the smallest diameter previously is 510 nm.[4] This work builds upon previous studies of direct electrospun TiO_2 fibers,[4,5] which required use of a toxic solvent, 2-methoxy ethanol[6-8] and yielded fibers with diameters greater than 0.5 μm.

Electrospinning is an established method for producing ceramic fibers with sub-μm diameters and lengths exceeding 100 μm.[1] In electrospinning, a high-voltage power supply is connected to a solution reservoir, generally a syringe, and a grounded deposition plate. As the solution is slowly pumped through the syringe under the applied voltage, rather than forming a bead at the tip of the needed, it is stretched and elongated into a "Taylor cone." When the Coulomb force exerted on the Taylor cone is high enough to overcome the surface tension of the solution, a stream of polymer solution jets from the tip of the cone. As the jet of polymer travels through the air, it whips around and the solvent evaporates, solidifying

and stretching out the fiber. Several polymers have been electrospun into fibers, including poly(ethylene oxide), poly(vinyl alcohol), polyvinylpyrrolidone, and polystyrene.[9]

Two approaches have been devised for fabricating ceramic fibers by electrospinning, a polymer-assisted method and sol-gel chemistry. In polymer-assisted electrospinning, a ceramic precursor, often a sol, a salt, or a coprecipitated nanoparticle, is mixed with a solvent and a polymer.[10] The polymer provides the appropriate rheology to allow electrospinning and templates the morphology of the fibers. The fibers are then calcined at temperatures above 450 °C to simultaneously remove the polymer additive and sinter the ceramic precursors. The benefit of this method is that the properties of the ceramic precursors play only a small role in the electrospinning process, which is instead controlled by the polymer additive. The disadvantage of this approach is that the samples can undergo large extents of shrinkage, which can result in mechanical breakage[1] and degradation of the optical properties of the fibers.[11] Polymer additives can also leave carbon residue within the fibers.[12] Because the polymer guides the electrospinning process, many types of ceramic fibers have been synthesized using this method, including TiO_2,[13] Al_2O_3,[14] SiO_2,[15] $NiFe_2O_4$,[16] SiC,[17] and B_4C.[18]

In the sol-gel chemical method for producing fibers by electrospinning, also known as direct electrospinning, polymer additives are excluded from the solution. Rather, by mixing the alkoxide precursor, solvent, water, and an acid, the viscosity of the solution can be controlled to allow electrospinning without adding a polymer. While direct electrospinning avoids the need for calcination and the associated challenges discussed above, obtaining a sol of the appropriate viscosity for electrospinning can be challenging. Because of this issue,

there have been only a few reports of direct electrospun ceramic fibers composed of SiO_2,[19-21] Al_2O_3,[22] $PbZrTiO_2$,[23,24] andTiO_2.[4,5] Another drawback of this method is that it the fiber diameters are generally greater than one μm, with one exception, where TiO_2 fibers of 500 nm were produced. As noted earlier, an issue specific to the production direct electrospun TiO_2[4,5] is the use 2-methoxy ethanol,[6-8] a known teratagen and mutagen.

For direct electrospinning, hydrolysis and condensation of the alkoxide precursor need to be controlled, such that they result in a network of long chains with minimal cross-linking or branching.[21,25] Such control can be obtained through the following steps: An acid rather than base should be used for catalyzing condensation. Acid catalysis drives formation of linear, ladder-like structures, allowing for the formation of viscous sols before gelling. In contrast, base catalysis causes branching and more readily produces nanoparticles, which does not allow for facile control of the viscosity.[25] Another important parameter is the amount of water with respect to the alkoxide. A molar ratio of 2 water : 1 alkoxide typically forms a sol with the ideal morphology.[22] Reducing the concentration can minimize cross-linking and favors electrospinning, while electrospinning of more highly concentrated sols is inhibited.[21]

Previous reports on electrospinning TiO_2 fibers either produced μm-scale TiO_2 fibers using a toxic solvent, or used polymer additives to assist with electrospinning and required calcination. Here we report use of ethanol-based sols for direct electrospinning of TiO_2 nanofibers without use of polymer additives and with average diameters below 100 nm,

which is ~5 times smaller than previous reports on TiO_2 and the first example of direct electrospun ceramic fibers with diameters below 100 nm.

6.2 Experimental Section

6.2.1 Sol Gel Synthesis

Titanium(IV) isopropoxide (TTIP, Acros Organics, 98%), anhydrous ethanol (Sigma Aldrich, 99.5%), nitric acid (Sigma Aldrich, 70%), and *N*,*N*-dimethylformamide (DMF, OmniSolv, 99.99%) were used to prepare a titania sol for electrospinning. The spinning solution for the electrospun fibers solution was developed by modifying a previous method for electrospinning TiO_2 fibers,[5] including replacing 2-methoxy ethanol with ethanol. 25 mL of ethanol was added to a 40-mL vial with a septum cap inside a glove box, to which 1.42 g of TTIP was added dropwise with rapid stirring and allowing complete mixing of the solution between drops. The vials was then sealed, stirred for 10 minutes, and removed from the glove box. 15.5 µL of concentrated nitric acid was then injected through the septum cap and allowed to sit for an additional 10 minutes. The vial is then opened to the air, and heated and 80 °C for 90 minutes with moderate stirring, followed by cooling to room temperature and rotary evaporation to reduce the total volume of the sol to ~1 mL. 50 µL of DMF was then added to the solution, and it was allowed to stir for 10 minutes. If not used immediately, the electrospinning solution was stored in a 3-mL syringe in a freezer at -16 °C. The solution showed no signs of gelation after 2 months of storage and remained suitable for electrospinning.

6.2.2 Electrospinning

A home-built setup was used for electrospinning, with a vented enclosure, horizontally oriented syringe pump, syringe, blunt-tipped needle, grounded collector plate covered with Al foil, and 30 kV power supply. The syringe prepared as described above was fitted with a 22-gauge, 1.5”-long, blunt-tipped needle. After removing pushing any air bubbles and a small amount of the solution out of the syringe, it was connected to the syringe pump, and the metal needle was connected to the power supply with an alligator clip. Using a tip-collector distance of 14 cm, the flow rate was set 1.0 to μL/min, and the voltage was set to 14 kV. When electrospinning had finished, 10 minutes elapsed before opening the enclosure and removing the sample, both to allow any residual charges on the needle and collector to dissipate, and to purge the enclosure of titania fibers that were not anchored to the collector or other surfaces. When the sample was removed, all surfaces inside the enclosure were wiped down with a damp cloth to remove any fibers that did not deposit on the plate. (Caution: This high voltage poses an electrocution hazard, and electrospinning should only be conducted with appropriate training. Enclosing the electrospinning setup in a box with interlocks can reduce the potential for exposure to the high voltage. The titania fiber also become airborne easily and pose an inhalation hazard.)

This method, as with many methods for electrospinning, may have some dependence on the ambient humidity, which varies by season. If the parameters for electrospnning need to be adjusted, the correct parameters were found by first adjusting the flow rate until fibers start to form, followed by the voltage and tip-collector distance adjusted until continuous

fibers formed. The presence of fibers was verified by depositing a test sample on a small square of Al foil and observing with on optical microscope.

6.2.3 Characterization and Conversion into Anatase TiO_2

The fibers were imaged by scanning electron microscopy (FEI Verios 460L). To prepare samples for *in situ* X-ray diffraction (XRD), titania fibers were collected on Si wafers adhered to the Al foil with double-sided tape. The samples were loaded into X-Ray diffractometer (PANalytical Empyreon) with a heating stage attachment (XRK 900). The fibers were heated under ambient atmosphere to 900 °C at a rate of 1 °C per minute. Diffractograms were collected continuously at rate of 1 measurement every 15 minutes. Values of 2θ were measured from 20° to 45° with a step of 0.026°.

6.3 Results and Discussion

6.3.1 Fiber Morphology

Nanoscale amorphous TiO_2 fibers were electrospun directly (Figure 1a), without using an organic polymer to assist with electrospinning. The fibers do not show signs of beading or crosslinking between fibers, common challenges in electrospinning. The as-spun fibers have an average diameter of 71 ± 27 nm (Figure 2). This is a 5-fold decrease in fiber diameter compared to previous studies.[4,5] The reduction of diameter can be partially attributed to replacing 2-methoxy ethanol with ethanol. The use of a solvents with lower a higher vapor pressure has been shown to decrease the diameter of polymeric nanofibers.[26]

The use of slower flow rates than are commonly applied for direct electrospinning may also contribute to the decreased diameter.[27]

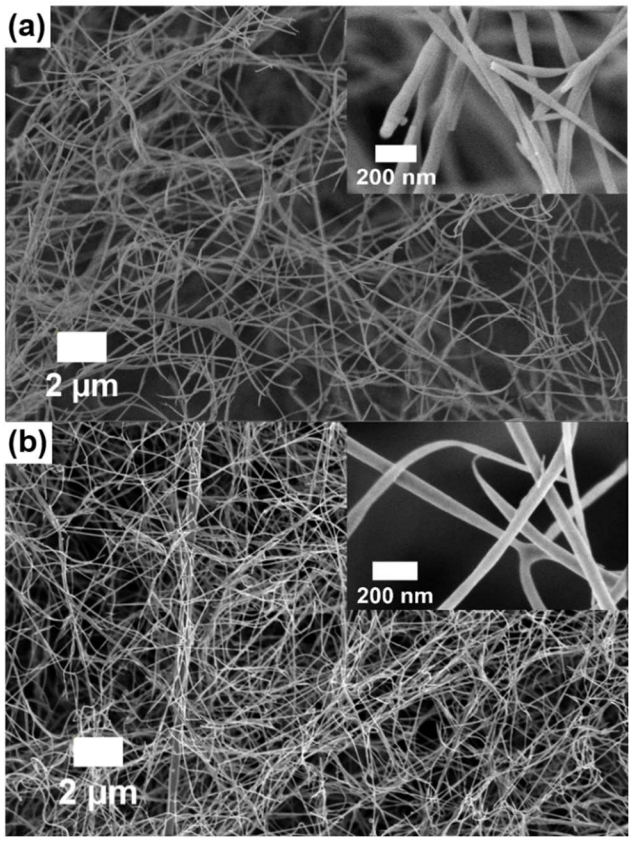

Figure 6.1 SEM images of amorphous TiO_2 nanofibers on a Si wafer (a) after electrospinning and (b) after heating to 450 °C in air for 2 hours. Insets show the sample samples at higher magnification.

A sample of TiO_2 fibers was heated to 450 °C for two hours (Figure 1b), which mimics conditions for calcining fibers that contain organic polymers.[13] The fibers show minimal morphological changes and no signs of breakage. The average fiber diameter is 64 ±

24 nm. This 10% decrease in diameter during heating can be attributed to generation and evaporation of ethanol as condensation is completed, yielding pure TiO_2 fibers.

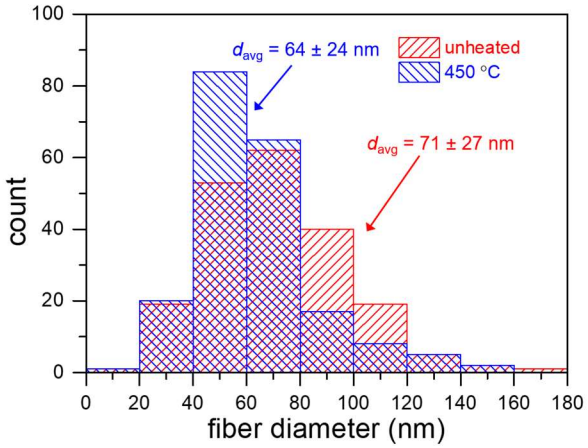

Figure 6.2 Histograms of the diameter of TiO2 fibers before and after heating to 450 °C for two hours. For each sample, 200 fibers were measured.

6.3.2 Guidance for Preparing the TiO_2 Sol

The following guidance was developed based on the more comprehensive literature for direct electrospinning of SiO_2 fibers.[19-21] The key to direct electrospinning of SiO_2 fibers without polymer additives is to produce a sol where the alkoxides form into long chains and minimizing branching or crosslinking, resulting in the formations of clusters and eventually particles. This is achieved by lowering the pH of the solution, because acid-catalyzed reactions preferentially form chains. Control over the water content and temperature are also important for controlling the rate of crosslinking, even though TTIP is less reactive than many other titanium alkoxides. If the reaction occurs too quickly, precipitates will form and

inhibit fiber formation. The appearance of cloudiness in the sol indicates that precipitation has occurred. When using ethanol instead of 2-methoxy ethanol, the amount of water in the system must be minimize, because water behaves as a catalyst. Water needs to be introduced in a controlled manner to keep the reaction slow enough that reactions form, and the 2:1 ratio of TTIP to alkoxide recommended in the literature reacted too quickly, causing precipitate to form in the sol. To compensate, the only water introduced to the system is from the HNO_3 and ambient humidity. Cross-linking is further minimized by performing the reaction under dilute conditions. For electrospinning, the solution was placed on a rotary evaporation to reduce the volume to 1 mL, which yielded a solution of appropriate viscosity for electrospinning.

6.3.3 Guidance for Electrospinning

Several parameters are important for obtaining continuous TiO_2 fibers with uniform diameters. Minor changes in the parameters for electrospinning, such as flow rate and voltage, can result in electrospray or short TiO_2 fibers. For example, minor changes in flow-rate, such as going from 1.0 μL/min to 1.1 μL/min, can change the deposition from continuous fibers to mostly particles. The voltage is similarly sensitive, where changing from 10 kV to 11 kV can result no fibers. Increasing the needle-tip distance has the effect of increasing the overall rate of deposition, but as the tip approaches the collector, more TiO_2 particles deposit onto the collector.

Challenges unique to direct electrospinning of oxide fibers include the presence of short fibers and nanoparticles. Polymer entanglement, which is controlled by the chain length and molecular weight, as in important aspect of electrospinning. The individual units in a TiO_2 sol are smaller than for electrospinning polymers. As a result, direct electrospinning of TiO_2 can be more challenging than when using a polymer. The short chains in TiO_2 sols limit the extent of entanglement. Non-optimal conditions for electrospinning can yield nanoparticles or short segments of fibers instead of contiguous fibers. To compensate for the lack of entanglement in TiO_2 sols, parameters for electrospinning need to be chosen carefully.

During direct electrospinning of TiO_2 fibers from an ethanol-based sol, some of the solution also crystalizes at the tip and causes clogging. Including a small amount of DMF in the sol slows evaporation of the solvent and inhibits crystallization of TiO_2, thus facilitating electrospinning.

6.3.3 *In Situ* X-Ray Diffraction

In situ XRD experiments of the TiO_2 fibers during heating to 900 °C under ambient atmosphere monitored formation of the anatase phase, followed by transformation into the rutile phase. Diffractograms were acquired at intervals of ~15 °C for 2θ between 20° and 45°, which contains the largest peaks in the anatase and the rutile crystal structures (Figure 3). The intensity of the broad background from amorphous TiO_2 decreases as the temperature approaches 500 °C. The peak for the anatase phase at 25.27° appears at 481- 496 °C. A

second, smaller anatase peak emerges at 37.78° between 728-743 °C and 890 °C. A rutile titania peak at 27.46° becomes visible at 852-867 °C.

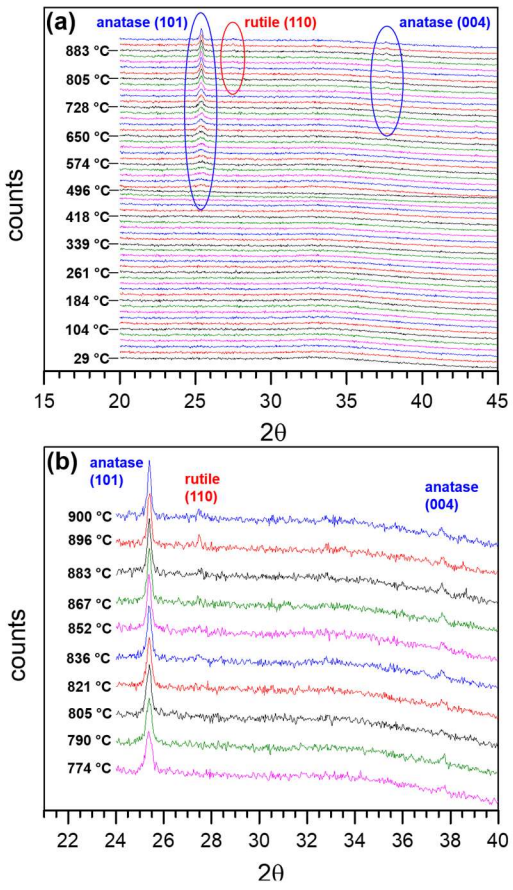

Figure 6.3 XRD of electrospun TiO_2 fibers on a Si wafer while heating to 900 °C at a rate of 1 °C / min. Diffractograms collected continuously at a rate of 1 measurement every ~15 minutes. Diffractograms were collected for 2θ values from 20° to 45° with a step of 0.026°. (a) All measurements from 0 to 900 ° (b) measurements from 774 °C to 900 °C and 20 ° to 40 ° to highlight peaks forming at higher temperatures.

In comparison, in previous work on direct-electrospun TiO_2 fibers, the anatase and rutile phases formed at 250 °C and at 600 °C, respectively.[5] Comparable polymer-assisted electrospun TiO_2 fibers reported the emergence of anatase peaks at 450 – 550 °C, with rutile appearing at 575 – 700 °C.[28-30] For TiO_2 powders and films that were analysed using a similar *in situ* method, anatase and rutile peaks appear at 400-500 °C and 600-850 °C, respectively.[31,32] Our observed conversion temperature for the anatase phase is consistent with these previous studies, while rutile was not observed until reaching 890 °C. Elevation of the rutile phase transition temperature, which is consistent with other studies of nanoscale TiO_2.[20,31,33]

6.4 Conclusions

These results highlight the viability of direct electrospinning of TiO_2 nanofibers using common, green solvents, by using sol gel chemistry to adjust the viscosity of the sol and by adjusting the parameters for electrospinning, most notably a slow flow rate than is commonly used. Eliminating the polymer additive also reduces the extent of shrinkage and breakage of the TiO_2 nanofibers during subsequent heating. Since sol gel chemistry is highly versatile and includes many metal oxides, this direct approach could likely be extended to other metal oxides and to mixed metal oxides, the solution conditions and parameters for electrospinning would need to be tailored for the molecular chemistry of different precursors.

6.5 References

(1) Wu, H.; Pan, W.; Lin, D.; Li, H. Electrospinning of ceramic nanofibers: Fabrication, assembly and applications. *Journal of Advanced Ceramics* **2012**, *1*, 2-23.

(2) Teo, W. E.; Ramakrishna, S. A review on electrospinning design and nanofibre assemblies. *Nanotechnology* **2006**, *17*, R89.

(3) Zhang, R.; Elzatahry, A. A.; Al-Deyab, S. S.; Zhao, D. Mesoporous titania: From synthesis to application. *Nano Today* **2012**, *7*, 344-366.

(4) Kim, Y. B.; Cho, D.; Park, W. H. Enhancement of mechanical properties of TiO2 nanofibers by reinforcement with polysulfone fibers. *Materials Letters* **2010**, *64*, 189-191.

(5) Won Keun, S.; Donghwan, C.; Won Ho, P. Direct electrospinning of ultrafine titania fibres in the absence of polymer additives and formation of pure anatase titania fibres at low temperature. *Nanotechnology* **2006**, *17*, 439.

(6) Nagano, K.; Nakayama, E.; Oobayashi, H.; Nishizawa, T.; Okuda, H.; Yamazaki, K. Experimental studies on toxicity of ethylene glycol alkyl ethers in Japan. *Environmental Health Perspectives* **1984**, *57*, 75-84.

(7) Miller, R. R.; Ayres, J. A.; Calhoun, L. L.; Young, J. T.; McKenna, M. J. Comparative short-term inhalation toxicity of ethylene glycol monomethyl ether and propylene glycol monomethyl ether in rats and mice. *Toxicology and Applied Pharmacology* **1981**, *61*, 368-377.

(8) Ma, H.; An, J.; Hsie, A. W.; Au, W. W. Mutagenicity and cytotoxicity of 2-methoxyethanol and its metabolites in Chinese hamster cells (the CHO/HPRT and AS52/GPT assays). *Mutation Research/Genetic Toxicology* **1993**, *298*, 219-225.

(9) Li, D.; Xia, Y. Electrospinning of Nanofibers: Reinventing the Wheel? *Advanced Materials* **2004**, *16*, 1151-1170.

(10) Sigmund, W.; Yuh, J.; Park, H.; Maneeratana, V.; Pyrgiotakis, G.; Daga, A.; Taylor, J.; Nino, J. C. Processing and Structure Relationships in Electrospinning of Ceramic Fiber Systems. *Journal of the American Ceramic Society* **2006**, *89*, 395-407.

(11) Tätte, T.; Hussainov, M.; Paalo, M.; Part, M.; Talviste, R.; Kiisk, V.; Mändar, H.; Põhako, K.; Pehk, T.; Reivelt, K.; Natali, M.; Gurauskis, J.; Lõhmus, A.; Mäeorg, U. Alkoxide-based precursors for direct drawing of metal oxide micro- and nanofibres. *Science and Technology of Advanced Materials* **2011**, *12*, 034412.

(12) Tuttle, R. W.; Chowdury, A.; Bender, E. T.; Ramsier, R. D.; Rapp, J. L.; Espe, M. P. Electrospun ceramic fibers: Composition, structure and the fate of precursors. *Applied Surface Science* **2008**, *254*, 4925-4929.

(13) Li, D.; Xia, Y. Fabrication of Titania Nanofibers by Electrospinning. *Nano Letters* **2003**, *3*, 555-560.

(14) Azad, A.-M. Fabrication of transparent alumina (Al2O3) nanofibers by electrospinning. *Materials Science and Engineering: A* **2006**, *435*, 468-473.

(15) Changlu, S.; Hakyong, K.; Jian, G.; Doukrae, L. A novel method for making silica nanofibres by using electrospun fibres of polyvinylalcohol/silica composite as precursor. *Nanotechnology* **2002**, *13*, 635.

(16) Li, D.; Herricks, T.; Xia, Y. Magnetic nanofibers of nickel ferrite prepared by electrospinning. *Applied Physics Letters* **2003**, *83*, 4586-4588.

(17) Liu, H. A.; Balkus, K. J. Electrospinning of beta silicon carbide nanofibers. *Materials Letters* **2009**, *63*, 2361-2364.

(18) Welna, D. T.; Bender, J. D.; Wei, X.; Sneddon, L. G.; Allcock, H. R. Preparation of Boron-Carbide/Carbon Nanofibers from a Poly(norbornenyldecaborane) Single-Source Precursor via Electrostatic Spinning. *Advanced Materials* **2005**, *17*, 859-862.

(19) Choi, S.-S.; Lee, S. G.; Im, S. S.; Kim, S. H.; Joo, Y. L. Silica nanofibers from electrospinning/sol-gel process. *Journal of Materials Science Letters* **2003**, *22*, 891-893.

(20) Zhang, G.; Kataphinan, W.; Teye-Mensah, R.; Katta, P.; Khatri, L.; Evans, E. A.; Chase, G. G.; Ramsier, R. D.; Reneker, D. H. Electrospun nanofibers for potential space-based applications. *Materials Science and Engineering: B* **2005**, *116*, 353-358.

(21) Geltmeyer, J.; Van der Schueren, L.; Goethals, F.; De Buysser, K.; De Clerck, K. Optimum sol viscosity for stable electrospinning of silica nanofibres. *Journal of Sol-Gel Science and Technology* **2013**, *67*, 188-195.

(22) Maneeratana, V.; Sigmund, W. M. Continuous hollow alumina gel fibers by direct electrospinning of an alkoxide-based precursor. *Chemical Engineering Journal* **2008**, *137*, 137-143.

(23) Yu, W.; Jorge, J. S.-A. Synthesis of lead zirconate titanate nanofibres and the Fourier-transform infrared characterization of their metallo-organic decomposition process. *Nanotechnology* **2004**, *15*, 32.

(24) Wang, Y.; Santiago-Avilés, J. J. A Review on Synthesis and Characterization of Lead Zirconate Titanate Nanofibers through Electrospinning. *Integrated Ferroelectrics* **2011**, *126*, 60-76.

(25) Sakka, S.; Yoko, T. Fibers from gels. *Journal of Non-Crystalline Solids* **1992**, *147*, 394-403.

(26) Asran, A. S.; Salama, M.; Popescu, C.; Michler, G. H. Solvent Influences the Morphology and Mechanical Properties of Electrospun Poly(L-lactic acid) Scaffold for Tissue Engineering Applications. *Macromolecular Symposia* **2010**, *294*, 153-161.

(27) Park, J. Y.; Lee, I. H.; Bea, G. N. Optimization of the electrospinning conditions for preparation of nanofibers from polyvinylacetate (PVAc) in ethanol solvent. *Journal of Industrial and Engineering Chemistry* **2008**, *14*, 707-713.

(28) Vasquez, H.; Gutierrez, H.; Lozano, K.; Leal, G. Titanium Dioxide Nanofibers through Forcespinning. *Journal of Engineered Fibers and Fabrics* **2015**, *10*, 129-136.

(29) Kumar, A.; Jose, R.; Fujihara, K.; Wang, J.; Ramakrishna, S. Structural and Optical Properties of Electrospun TiO2 Nanofibers. *Chemistry of Materials* **2007**, *19*, 6536-6542.

(30) Carato, B.; Carneiro, E.; Sa, P.; Almeida, B.; Carvalho, S. Properties of Electrospun TiO2 Nanofibers. *Journal of Nanotechnology* **2014**, *2014*, 5.

(31) Patra, S.; Davoisne, C.; Bouyanfif, H.; Foix, D.; Sauvage, F. Phase stability frustration on ultra-nanosized anatase TiO2. **2015**, *5*, 10928.

(32) Albetran, H. M.; O'Connor, B. H.; Low, I. M. Effect of pressure on TiO2 crystallization kinetics using in-situ high-temperature synchrotron radiation diffraction. *Journal of the American Ceramic Society* **2017**, *100*, 3199-3207.

(33) Zhang, H.; F. Banfield, J. Thermodynamic analysis of phase stability of nanocrystalline titania. *Journal of Materials Chemistry* **1998**, *8*, 2073-2076.

CHAPTER 7: Silica-Overcoated Gold Nanorods in Direct Electrospun Silica Nanofibers

7.1 Introduction

Ceramic nanofibers have tremendous promise for use in applications such as catalysis, electronics, sensors, and electrodes.[1] Nanoparticles (NPs) can also be incorporated into ceramic nanofibers to impart novel optical, magnetic, electronic, and catalytic properties, but such incorporation has been limited primarily to NPs formed *in situ* or heat-stable NPs that are not affected by the calcination step.[2] We have developed electrospun silica (SiO_2) nanofibers containing silica-overcoated gold nanorods (SiO_2-GNRs) through direct electrospinning and have investigated the thermal stability of the shape of the embedded GNRs when the fibers are heated in air.

Electrospinning is a simple method for producing a wide range of 1-D polymers and ceramics. The electrospinning setup consists of a high-voltage power supply, syringe pump, needle, and collector. Fibers are made by applying a voltage, which provides a high electric field between the tip of the needle and the grounded collector plate, while pumping a viscous polymer solution or sol of ceramic precursors through the needle. Coulombic forces draw the solution into a fiber that stretches and dries while traveling from the needle to the collector, resulting in fibers 100's of μm long and with diameters in the sub-μm and nm scales. The diameter of the fibers can be controlled by varying the concentration of the solution for electrospinning, applied voltage, needle-collector distance, and solution feed rate.[3]

Methods for producing electrospun ceramic fibers can be classified as two types. One approach is to add a ceramic precursor (salt, NPs, or sol) to a polymer solution for electrospinning. The polymer provides the viscosity and capability for entanglement necessary for electrospinning and is later removed during calcination. The other approach is to exploit sol gel chemistry to convert an alkoxide precursor into a sol that electrospins without a polymer additive. Using this method, called direct electrospinning, calcination is not required because there is no polymer additive. Given the relative simplicity of electrospinning polymer solutions, polymer-assisted electrospinning has been the generally preferred method for producing electrospun ceramic fibers. To prepare a sol conducive to electrospinning is much more difficult, and only a handful of examples can be found in the literature.

Incorporating NPs into electrospun fibers is an appealing approach for enhancing the physical and chemical properties of electrospun fibers. NPs can possess diverse and scientifically and technologically important optical, magnetic, and catalytic properties, and many have been incorporated into electrospun fibers. Incorporating NPs into polymer fibers usually simply a matter of mixing NPs into the polymer solution and then electrospinning.[2] There are some reports of applying this method for ceramics nanofibers,[4-6] but the calcination process required to remove the polymer additives can damage the NPs or negatively affect their arrangement. Many types of NPs cannot withstand the high temperatures of calcination. To obviate this challenge, NPs can be formed *in situ*. A precursor salt for NPs is added to the ceramic precursor/polymer mixture, and the salt is reduced during calcination, leaving NPs

dispersed throughout the fibers.[2] This method has been used to incorporate many types NPs (Ag, Pd, Pt, Au, ZrO_2) into different ceramic matrices (TiO_2, ZnO, Al_2O_3, SiO_2).[6-10] Although this method is effective for incorporating NPs into nanofibers, it provides limited control over the size, shape, distribution, and location of NPs.

By direct electrospinning a silica sol with pre-synthesized SiO_2-GNRs, we have shown that we are able to incorporate GNRs in SiO_2 fibers with minimal effects on the morphology of the GNRs. Although the scope of this work is limited to GNRs, many types of NPs can likely be incorporated in direct-electrospun SiO_2 fibers, as long as they are compatible with the SiO_2 precursor sol or have SiO_2 shells to impart compatibility.

7.2 Experimental

7.2.1 Chemicals

$HAuCl_4 \cdot 3H_2O$ (Alfa Aesar, 99.999%), cetyltrimethylammonium bromide (CTAB, Amresco, 99%), $AgNO_3$ (Alfa Aesar 99.9995%), ascorbic acid (J.T. Baker 99.5%), KBr (Alfa Aesar, 99% min), deionized water (Ricca, AS Reagent grade, ASTM Type I, ASTM Type II), and $NaBH_4$ (Sigma-Aldrich, 99%, 213462) were used for synthesizing GNRs. Tetraethyl orthosilicate (TEOS, Alfa Aesar, 99.9%), methanol for mixing with TEOS (EMD, DriSolv), methanol for SiO_2-GNR purification (Macron, Ultim AR), NaOH (Sigma Aldrich, 99%), and HCl (BDH, 36.5-38%) were used for depositing SiO_2 shells, yielding SiO_2-GNRs, and for purification.

7.2.2 Synthesis of Silica-Overcoated Gold Nanorods

CTAB-stabilized gold nanorods were made using a seed mediated synthesis method established by Kozek et al.[11] In this method, a one-liter aqueous dispersion of gold nanorods is produced containing 100 mM CTAB and 190 mg of gold nanorods. A secondary growth process, driven by injection of additional ascorbic acid was used to reduce residual gold precursor and deposit it onto the surface of the GNRs. To prepare the GNRs for overcoating with SiO_2,[12] 100 mL of the GNR solution was brought to 28°C and then centrifuged twice at 12,900 rpm (IEC Centra MP4, 8,500 *g*). After purification, a dispersion of 10 mL of SiO_2-GNRs was prepared with a final volume 10 mL and final concentrations of GNRs and CTAB of 1.8 mg / mL and 1 mM respectively.

The concentrated GNRs were heated to 30 °C in a water bath, and the pH was adjusted to 10.4 (measured with a Hannah Checker pH meter) using 0.1 M NaOH. 250 µL of 20% TEOS in methanol was injected into the GNRs by syringe pump at a rate to 50 µL/min and with a stir rate of 150 rpm. After completing the injection, the stir rate was adjusted to stir at 70 rpm for 30 min. The solution then aged without stirring for 20 hours. Upon completing the reaction, the product was immediately distributed among 4×40 mL centrifuge tubes. Each tube was diluted to 40 mL with methanol and centrifuged 5 times at 10,000 rpm (8,500 *g*) for 10 min. After each cycle of centrifugation, the supernatant was removed and the SiO_2-GNRs were redispersed in fresh methanol and sonicated until well dispersed. The purified SiO_2-GNRs were stored in methanol at a concentration of 3.6 mg / mL. In preparation for use in the sol for electrospinning, 2.2 mL of SiO_2-GNRs in methanol was

dispersed in ethanol through rotary evaporation of the methanol and redispersion in 1.45 mL ethanol.

7.2.3 Preparation of Sol for Direct Electrospinning

The sol for electrospinning was synthesized by an established procedure.[13] In this method, the optimal electrospinning sol was produced using a molar ratio of 1:2:2:0.01 TEOS:ethanol:H_2O:HCl. To produce the sol, 2.63 mL of TEOS was first mixed with 1.48 mL of the ethanol / SiO_2-GNR solution and left to mix for 10 minutes. Next, 12.5 µL of concentrated HCl was mixed with 438 µL of water. The dilute HCl solution was then added dropwise to a rapidly stirring mixture of TEOS and SiO_2-GNRs in ethanol, allowing for complete mixing of the solution between drops. The solution was then heated 80 °C under ambient atmosphere with moderate stirring for 30 minutes, followed by cooling to room temperature and rotary evaporation to reduce until the sol was ~40% solids (determine by heating an aliquot at 110 °C overnight) and noticeably more viscous. If not used immediately, the electrospinning solution was stored in a 3-mL syringe in a freezer at -16 °C.

7.2.4 Electrospinning

A home-built setup was used for electrospinning, with a vented enclosure, horizontally oriented syringe pump, syringe, blunt-tipped needle, grounded collector plate covered with Al foil, and 30-kV power supply. The syringe prepared as described above was fitted with a 22-gauge, 1.5”-long, blunt-tipped needle. After pushing any air bubbles and a small amount of the solution out of the syringe, it was connected to the syringe pump, and an

electrical connection between the metal needle and power supply was made with an alligator clip. Using a tip-collector distance of 10 cm, the flow rate was set to 0.5 μL/min, and the voltage was set to 10 kV.

This method, as with many methods for electrospinning, may have some dependence on the ambient humidity, which varies by season. If the parameters for electrospinning needed to be adjusted, the correct parameters were found by first adjusting the flow rate until fibers started to form, followed by the voltage and tip-collector distance adjusted until continuous fibers formed. The presence of fibers was verified by depositing a test sample on a small square of Al foil and observing with on optical microscope.

7.2.5 Heating

Electrospun fibers were deposited directly onto a SiN transmission electron microscopy (TEM) grid (Protochips) by placing the TEM grids directly on the aluminium foil-covered collector plate using double-sided tape. The electrospinning set-up was run long enough to deposit a thin layer of electrospun SiO_2 fibers onto the TEM grids. Each sample was the inserted into a tube furnace heated in air for 3 hours (after coming temperature) at 400 °C, 500 °C, 600 °C, 700 °C, 800 °C, or 900 °C with a ramp rate of 30 °C / min. TEM images were collected (JEOL 2000FX) of SiO_2-GNRs in fibers at each temperature. SEM images (FEI Verios 460L) were collected for the unheated fibers and after heating to 900 °C. SiO_2-GNRs in methanol were drop cast on Cu TEM grids with ultrathin amorphous carbon supports. (Ted Pella, 01822)

7.3 Results

Electrospun SiO_2 nanofibers containing 1% SiO_2-GNRs by weight, determined by assuming complete condensation of SiO_2, were electrospun directly onto SiN TEM grids. The as spun or green nanofibers were continuous with little evidence of beading or crosslinking between fibers, (Figure 7.1a) which are common issues in electrospinning. Although beading was not evident, there were some examples of fibers with uneven diameters over the course of the fiber's length, with some segments over 3× wider than other segments of the fiber. The green nanofibers have an average diameter of 170 ± 68 nm determine by measuring the widest segment of the fiber (Figure 7.2). Comparing the diameters of these fibers to direct electrospun SiO_2 in the literature, these fibers are half the size of what has been shown in the literature.[13-16] The reduction in diameter can be attributed to our slower flow rate.[17]

Samples of SiO_2 composite nanofibers were heated in a tube furnace at 900 °C for 3 hours. After heating, the diameter of the fibers was 139 ± 79 nm, corresponding to shrinkage by 18% (Figure 7.2). The decrease in fiber diameter can be attributed to completing condensation of an incompletely crosslinked gel, and removing any residual hydroxy and ethoxy groups.[18] The morphology of the fibers is preserved, and there are no signs of breakage during heating (Figure 7.1b).

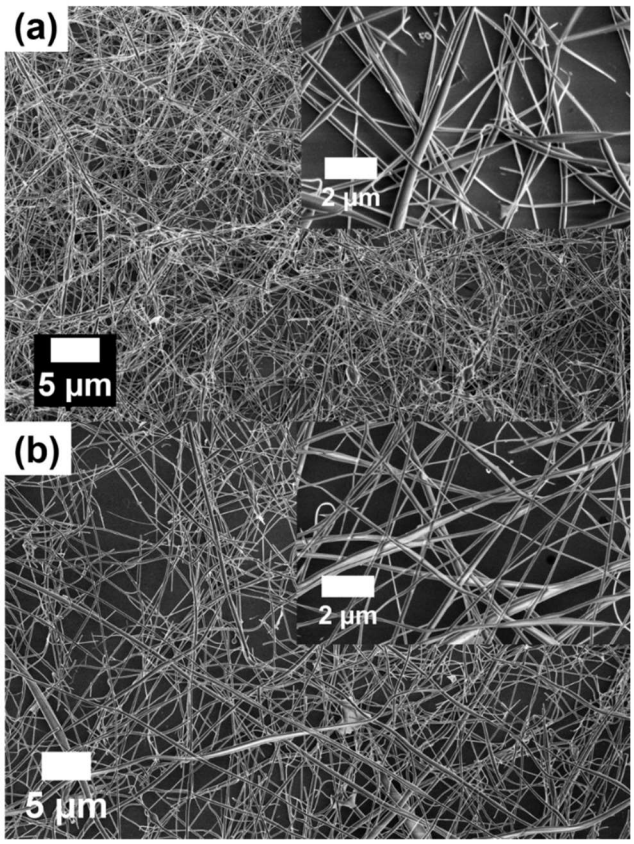

Figure 7.1 SEM image of direct electrospun SiO_2 nanofibers with incorporated SiO_2-GNRs (a) before heat treatment and (b) after heating to 900 °C for three hours. Insets show the samples at higher magnification.

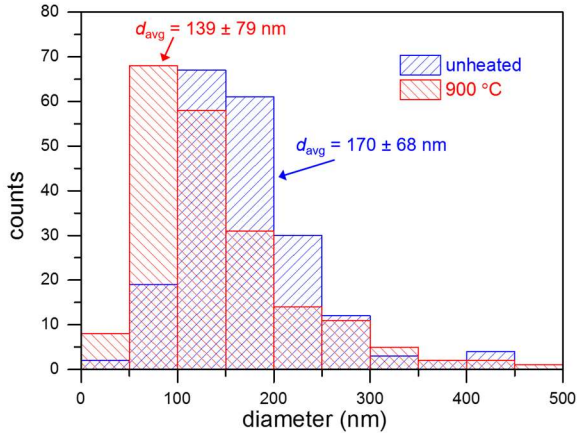

Figure 7.2 Histogram of the diameter of SiO_2 nanofibers before and after heating to 900 °C for three hours. For each sample, 200 fibers were measured.

TEM of green SiO_2 fibers shows that SiO_2-GNRs align during the electrospinning proces (Figure 3b). Prior work has demonstrated alignment of gold nanorods in polymer fibers,[19] but this is the first example of alignment in a ceramic fiber. TEM also reveals partial wetting of the SiO_2 fibers at the interface with the TEM grid, resulting in partial flattening of the fibers at interface, manifested as a shadow in the center of the fiber (Figure 3b, d, g, and h). Wetting is visible in the green fibers, which implies that it occurrs during formation and deposition. Evaporation of solvent and condensation of the fiber gel are likely responsible for the wetting effect. The fibers take time to fully cross-link and harden, and in that time, they may adhere to the substrate.[18]

To explore the thermal shape stability of the SiO_2-GNRs in SiO_2 nanofibers, samples on SiN TEM substrates were heated in air for 3 hours at temperatures ranging from 400 to

900 °C. The fibers have good structural stability when heated to 900 °C, which is expected of direct electrospun SiO_2 fibers.[13] The thermal stability of SiO_2-GNRs, on the other hand, is limited to lower temperatures at which they reshape into spheres. CTAB-stabilized GNRs are much less stable, reshaping at temperatures as low as 100 °C.[20,21] GNRs stabilized by an SiO_2 shell have much better stability in air.[22,23] TEM images of the SiO_2 fibers shows the impact of temperature on the fibers (Figure 7.3). The SiO_2-GNRs maintain their shape up to 600 °C. At 500 °C, the SiO_2-GNRs begin to exhibit cavitation between the core and shell at one end of the GNR. This cavitation has been attributed to the removal of the CTAB layer, and the heating and cooling the the GNR within SiO_2.[22,23] The GNRs begin to reshape at 700 °C. At 800 °C, there is no evidence of voids. The mesoporous SiO_2 shell encapsaulating the GNRs is visible up to 700 °C, but above 800 °C, the porosity is no longer visible, which is consistent with collapse of the pores. At temperatures above 650 °C gels with porous strucutres are know to begin densification, where the pores in the SiO_2 shell collapse.[22]

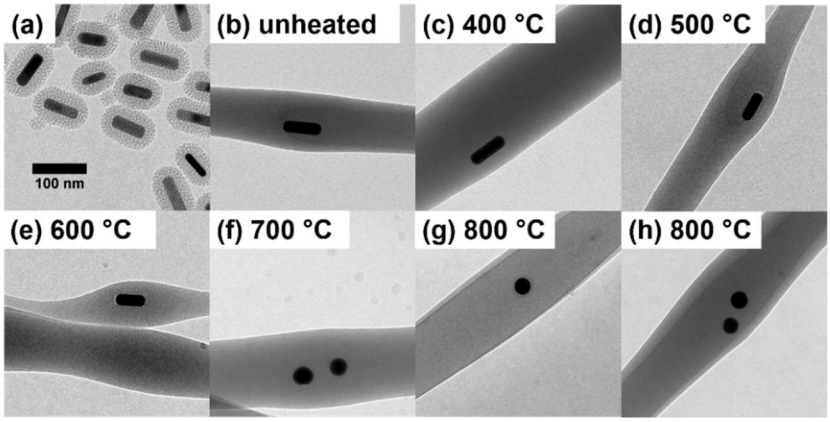

Figure 7.3 TEM of (a) SiO_2-GNRs and electrospun composite SiO_2 nanofibers (b) before heat treatment and after heating for 3 hours at (c) 400 °C, (d) 500 °C, (e) 600 °C, (f) 700 °C, (g) 800 °C, and (h) 900 °C.

7.4 Conclusions

Direct electrospun SiO_2 fibers have been produced containing SiO_2-GNRs. The fibers produced are continous, bead free, and achieve average diameters of 170 nm and 139 nm before and after calcination, respectively. The SiO_2 fibers are stable during heating, shrinking by ~20% and showing no of breakage when heated to 900 °C. SiO_2-GNRs align during electrospinning, and the alignment is maintained during densification. SiO_2-GNRs start showing signs of reshaping at 500 °C, when a void forms at one end GNR. The mesoporous structure of the SiO_2 shell collapses at 700 °C, and the GNRs reshape into spherical nanaoparticles.

7.5 References

(1) Wu, H.; Pan, W.; Lin, D.; Li, H. Electrospinning of ceramic nanofibers: Fabrication, assembly and applications. *Journal of Advanced Ceramics* **2012**, *1*, 2-23.

(2) Zhang, C.-L.; Yu, S.-H. Nanoparticles meet electrospinning: recent advances and future prospects. *Chemical Society Reviews* **2014**, *43*, 4423-4448.

(3) Li, D.; Xia, Y. Electrospinning of Nanofibers: Reinventing the Wheel? *Adv Mater* **2004**, *16*, 1151-1170.

(4) Shi, W.; Lu, W.; Jiang, L. The fabrication of photosensitive self-assembly Au nanoparticles embedded in silica nanofibers by electrospinning. *J Colloid Interface Sci* **2009**, *340*, 291-297.

(5) Wen, S.; Liu, L.; Zhang, L.; Chen, Q.; Zhang, L.; Fong, H. Hierarchical electrospun SiO2 nanofibers containing SiO2 nanoparticles with controllable surface-roughness and/or porosity. *Materials Letters* **2010**, *64*, 1517-1520.

(6) Ding, Y.; Wang, Y.; Zhang, L.; Zhang, H.; Li, C. M.; Lei, Y. Preparation of TiO2-Pt hybrid nanofibers and their application for sensitive hydrazine detection. *Nanoscale* **2011**, *3*, 1149-1157.

(7) Patel, A. C.; Li, S.; Wang, C.; Zhang, W.; Wei, Y. Electrospinning of Porous Silica Nanofibers Containing Silver Nanoparticles for Catalytic Applications. *Chemistry of Materials* **2007**, *19*, 1231-1238.

(8) Wang, X.; Dou, L.; Li, Z.; Yang, L.; Yu, J.; Ding, B. Flexible Hierarchical ZrO2 Nanoparticle-Embedded SiO2 Nanofibrous Membrane as a Versatile Tool for Efficient Removal of Phosphate. *ACS Applied Materials & Interfaces* **2016**, *8*, 34668-34676.

(9) Lin, D.; Wu, H.; Zhang, R.; Pan, W. Enhanced Photocatalysis of Electrospun Ag−ZnO Heterostructured Nanofibers. *Chemistry of Materials* **2009**, *21*, 3479-3484.

(10) Shin, H.; Abutaleb, A.; Lolla, D.; Chase, G. Effect of Calcination Temperature on NO–CO Decomposition by Pd Catalyst Nanoparticles Supported on Alumina Nanofibers. *Fibers* **2017**, *5*, 22.

(11) Kozek, K. A.; Kozek, K. M.; Wu, W.-C.; Mishra, S. R.; Tracy, J. B. Large-Scale Synthesis of Gold Nanorods through Continuous Secondary Growth. *Chemistry of Materials* **2013**, *25*, 4537-4544.

(12) Wu, W.-C.; Tracy, J. B. Large-Scale Silica Overcoating of Gold Nanorods with Tunable Shell Thicknesses. *Chemistry of Materials* **2015**, *27*, 2888-2894.

(13) Choi, S.-S.; Lee, S. G.; Im, S. S.; Kim, S. H.; Joo, Y. L. Silica nanofibers from electrospinning/sol-gel process. *Journal of Materials Science Letters* **2003**, *22*, 891-893.

(14) Patel, A. C.; Li, S.; Yuan, J.-M.; Wei, Y. In Situ Encapsulation of Horseradish Peroxidase in Electrospun Porous Silica Fibers for Potential Biosensor Applications. *Nano Lett* **2006**, *6*, 1042-1046.

(15) Zhang, G.; Kataphinan, W.; Teye-Mensah, R.; Katta, P.; Khatri, L.; Evans, E. A.; Chase, G. G.; Ramsier, R. D.; Reneker, D. H. Electrospun nanofibers for potential space-based applications. *Materials Science and Engineering: B* **2005**, *116*, 353-358.

(16) Geltmeyer, J.; Van der Schueren, L.; Goethals, F.; De Buysser, K.; De Clerck, K. Optimum sol viscosity for stable electrospinning of silica nanofibres. *Journal of Sol-Gel Science and Technology* **2013**, *67*, 188-195.

(17) Li, D.; Wang, Y.; Xia, Y. Electrospinning of Polymeric and Ceramic Nanofibers as Uniaxially Aligned Arrays. *Nano Lett* **2003**, *3*, 1167-1171.

(18) Hench, L. L.; West, J. K. The sol-gel process. *Chem Rev* **1990**, *90*, 33-72.

(19) Roskov, K. E.; Kozek, K. A.; Wu, W.-C.; Chhetri, R. K.; Oldenburg, A. L.; Spontak, R. J.; Tracy, J. B. Long-Range Alignment of Gold Nanorods in Electrospun Polymer Nano/Microfibers. *Langmuir* **2011**, *27*, 13965-13969.

(20) Zou, R.; Zhang, Q.; Zhao, Q.; Peng, F.; Wang, H.; Yu, H.; Yang, J. Thermal stability of gold nanorods in an aqueous solution. *Colloids and Surfaces A: Physicochemical and Engineering Aspects* **2010**, *372*, 177-181.

(21) Petrova, H.; Perez Juste, J.; Pastoriza-Santos, I.; Hartland, G. V.; Liz-Marzan, L. M.; Mulvaney, P. On the temperature stability of gold nanorods: comparison between thermal and ultrafast laser-induced heating. *Phys. Chem. Chem. Phys.* **2006**, *8*, 814-821.

(22) Wu, W. C. Multifunctional Gold Nanorods: Large-Scale Synthesis, Overcoating, Alignment, and Applications. North Carolina State University, 2014.

(23) Albrecht, W.; Deng, T.-S.; Goris, B.; van Huis, M. A.; Bals, S.; van Blaaderen, A. Single Particle Deformation and Analysis of Silica-Coated Gold Nanorods before and after Femtosecond Laser Pulse Excitation. *Nano Lett* **2016**, *16*, 1818-1825.

CHAPTER 8. Contributions to Other Projects

8.1 Longitudinal Alignment and Optical Characterization of Gold Nanostars in Electrospun Polymer Fibers

The goal of this project was to determine if anisotropic gold nanostars (AuNS) could be aligned on the macroscale by electrospinning to characterize the optical properties of the electrospun fibers. This project was done in collaboration with a high school student, Vamsi Varanasi of Enloe High School in Raleigh, NC. I served as his mentor and planned experiments until he had enough experience to work more independently. First, I guided him through the production of AuNS using an established method, where Au^{3+} is reduced and the AuNS are stabilized by 4-(2-hydroxyethyl)-1-piperazineethanesulfonic acid)) (HEPES).[1] I added a final step, where PEG-thiol is added at the end of the synthesis to terminate growth and prevent agglomeration, a critical step for incorporating AuNS into electrospun fibers. I performed characterization, including TEM of the AuNS and electrospun nanofibers, scanning transmission electron microscopy (STEM) of AuNS in nanofibers, and SEM of the fibers (Figure 8.1). I also prepared samples of aligned and randomly oriented fiber when Vamsi was no longer available to perform experiments.

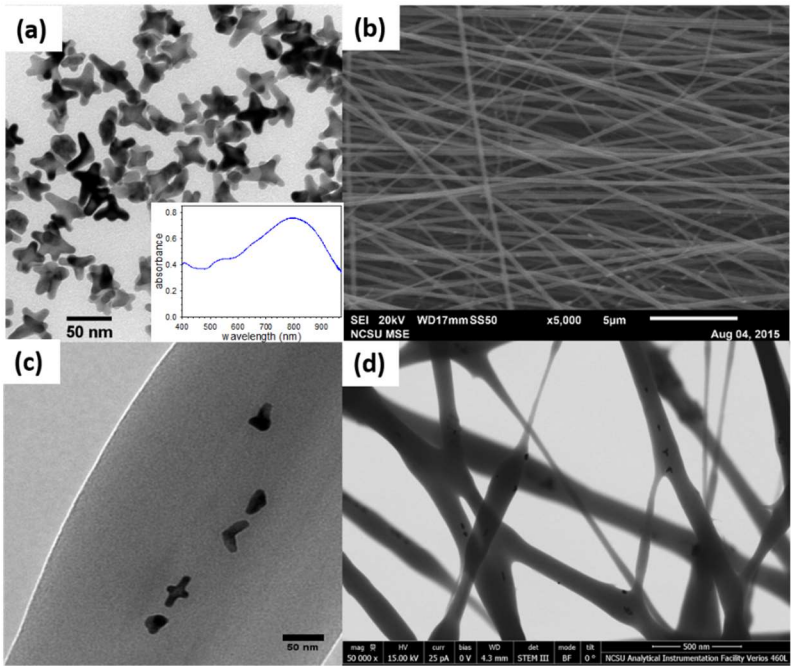

Figure 8.1 (a) TEM of AuNS with an inset of their optical absorbance spectrum, (b) SEM of aligned fibers, (c) TEM of AuNS aligned in a PEO fiber, and (d) STEM of AuNS aligned in fibers.

8.2 PEGylated Gold Nanorods for Diffusion-Sensitive Optical Coherence Tomography

The goal of this project, a collaboration with Prof. Amy Oldenburg and Prof. Richard Blackmon of the University of North Carolina-Chapel Hill was to measure the diffusion of gold nanorods (GNRs) through an extracellular matrix using optical coherence tomography.[2,3] For this purpose, CTAB-stabilized GNRs needed to be functionalized with PEG-thiol to make them compatible with their samples. The method of PEGylation used in prior research did not consistently provide sufficient stability for use in their experiments. I

improved upon the procedure for PEGylation previously used in the Tracy group.[4] The procedures for PEGylation can be found in the Appendix 2.

8.3 Silica-Overcoated Zeolite Nanopatelets

The goal of this project was to overcoat zeolite (Al_xSi_xONa) nanoplatelets with a layer of mesoporous silica (SiO_2) to improve their dispersibility and prevent stacking in solution. The SiO_2-zeolite platelets were to be used in further projects investigating convective assembly. This project was a collaboration with Prof. Ben Martin and his undergraduate student Daniel Hernandez at Texas State University. Daniel was a Research Experience for Undergraduates (REU) student. I taught Daniel how to overcoat GNRs with silica and planned experiments to determine the best approach for overcoating zeolite with silica, and performed TEM on the nanoplatelets (Figure 8.2).

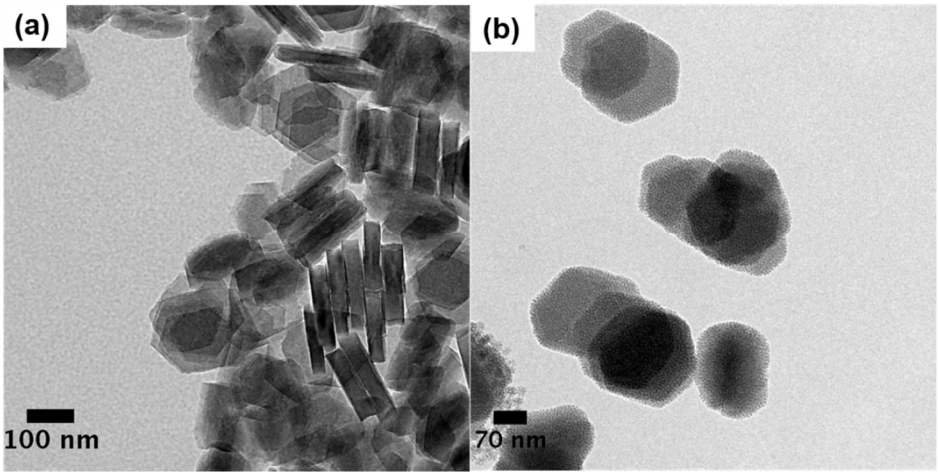

Figure 8.2 (a) Zeolite nanoplatelets and (b) SiO_2-zeolite nanoplatelets.

8.4 Low Aspect-Ratio Gold Nanorods

In collaboration with a colleague, Dr. Bryan Andersen, I developed low aspect-ratio GNRs that have an LSPR as low as 610 nm for incorporation into electrospun PEO fibers with silica- overcoated quantum dot nanorods (SiO_2-QDNR) to study Förster resonance energy transfer (FRET).[5] The procedure I developed for producing low aspect-ratio GNRs is reported in Appendix 2. I also performed STEM on the fibers (Figure 8.3 and 8.4).

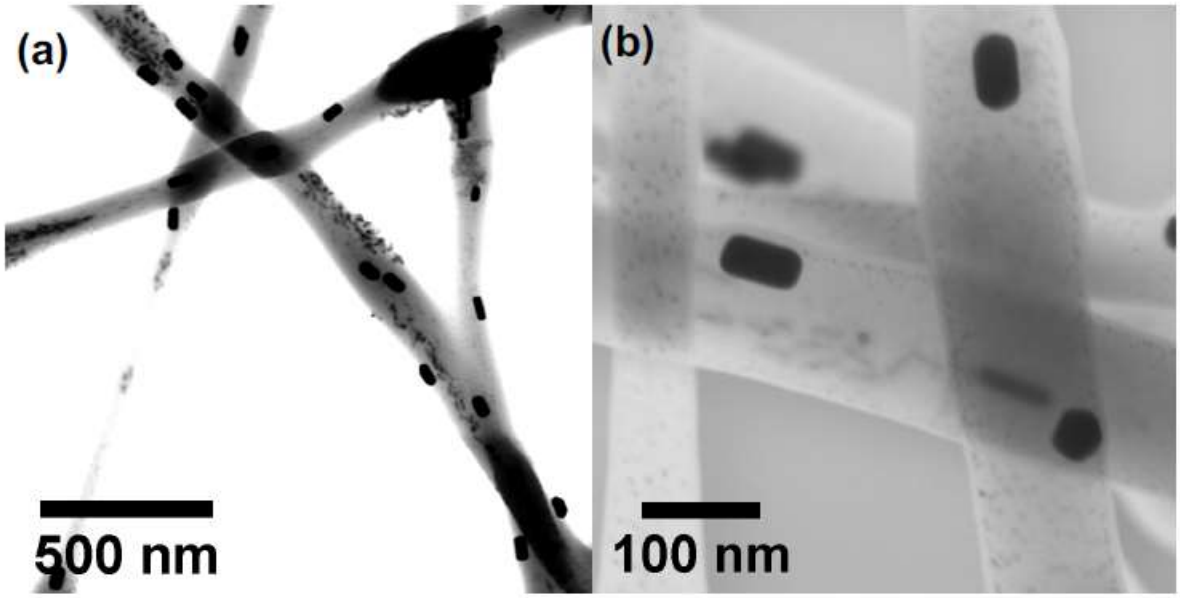

Figure 8.3 STEM of electrospun PEO fibers containing aligned QDNRs and low aspect ratio GNRs.[5]

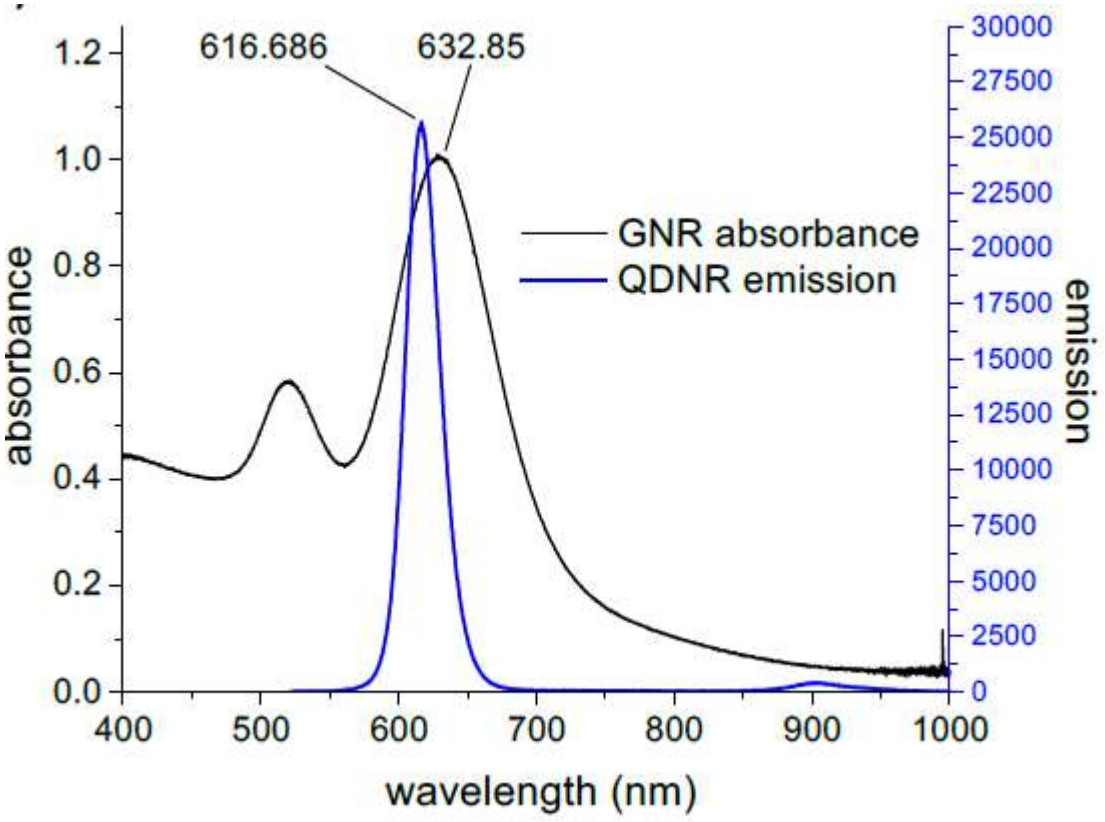

Figure 8.4 Optical absorbance spectra of low-aspect ratio GNRs and optical emission spectra of QDNRs, highlighting their spectral overlap.[5]

8.5 References

(1) Xie, J.; Lee, J. Y.; Wang, D. I. C. Seedless, Surfactantless, High-Yield Synthesis of Branched Gold Nanocrystals in HEPES Buffer Solution. *Chemistry of Materials* **2007**, *19*, 2823-2830.

(2) Blackmon, R. L.; Sandhu, R.; Chapman, B. S.; Casbas-Hernandez, P.; Tracy, J. B.; Troester, M. A.; Oldenburg, A. L. Imaging Extracellular Matrix Remodeling In Vitro by Diffusion-Sensitive Optical Coherence Tomography. *Biophysical Journal* **2016**, *110*, 1858-1868.

(3) Blackmon, R. L.; Kreda, S. M.; Sears, P. R.; Chapman, B. S.; Hill, D. B.; Tracy, J. B.; Ostrowski, L. E.; Oldenburg, A. L. Direct monitoring of pulmonary disease treatment

biomarkers using plasmonic gold nanorods with diffusion-sensitive OCT. *Nanoscale* **2017**, *9*, 4907-4917.

(4) Wu, W. C. Multifunctional Gold Nanorods: Large-Scale Synthesis, Overcoating, Alignment, and Applications. North Carolina State University, 2014.

(5) Anderson, B. D. Chemical Synthesis and Silica Overcoating of Nanoparticles with Tailored Morphologies. North Carolina State University, 2016.

APPENDIX

Appendix 1. Short Aspect Ratio Gold Nanorods

The following is a procedure that was developed for producing low aspect ratio gold nanorods (GNRs) based on the method established by Kozek et al.[1] By adjusting the concentration of silver nitrate ($AgNO_3$) and the ascorbic acid (AA) injection rate, GNRs can be made that absorb at wavelengths as low as 610 nm. The rationale for these changes is discussed in Chapter 2.

1. Start with the standard method of making 1 L of GNRs that absorb at 800 nm
    a. Quantities for growth solution
        i. 34.309 g cetyltrimethylammonium bromide (CTAB) in 450 mL H_2O
        ii. 1.12 g KBr in 10 mL H_2O
        iii. 0.0326 g $AgNO_3$ in 10 mL H_2O
        iv. 0.1857 g AA in 15 mL H_2O
        v. 0.3789 g $HAuCl_4$ 500 mL H_2O
        vi. 1.3575 mL seed solution
    b. Quantities for seed solution
        i. 0.364 g CTAB in 8 mL water
        ii. 0.011872 g KBr in 1 mL H_2O
        iii. 0.00100 g $HAuCl_4$ in 1 mL H_2O
        iv. 0.000378 g $NaBH_4$ in 0.6 mL water
    c. Secondary Growth of GNRs

i. 0.0832 g AA in 30 mL H_2O

ii. Injection rate of 175 µL / min

2. Modify the procedure to make lower-aspect-ratio GNRs

   a. Primary growth: Lower the $AgNO_3$ concentration

      i. Decrease the amount of seed by from 1x$AgNO_3$ to 0.5x

         Can be decreased more but, yield decreases

      ii. 0.0163 g $AgNO_3$ in 10 mL water

      iii. This blueshifts the absorption spectrum ~50 nm

   b. Secondary growth: decrease the AA injection rate

      i. Decrease the injection rate by 0.125×

      ii. 21.88 µL/min (total injection time of 22.85 hours)

      iii. Blueshifts the absorption spectrum an additional 100 to 150 nm

Appendix 2. PEGylation

The following is an improved procedure for functionalizing CTAB-stabilized GNR with poly(ethylene glycol) (PEG)-thiol. By destabilizing the GNRs by reducing the CTAB concentration below the critical micelle concentration, increasing the temperature of the functionalization reaction, and using a higher molecular weight PEG-thiol, we produced GNRs that are more stable for biomedical applications. The rationale for developing this procedure is presented in Chapter 8.

1. Changes to the procedure established by Wei-Chen Wu.[2]
    a. Reduced CTAB concentration from 1 mM to 0.2 mM
    b. Increased temperature of functionalization from room temperature to 40 °C
    c. Used 2000 MW PEG-thiol instead of 1000 MW PEG-thiol
2. Procedure
    a. Start with 100 mL of unprocessed CTAB stabilized GNRs (18 mg GNRs and 100 mM CTAB) heated to 28 °C until CTAB is completely dissolved
        i. Distribute GNRs into 2 centrifuge tubes, each with 50 mL of GNRs
        ii. Centrifuge once at 12,900 rpm (14,200 *g*) for 20 min
        iii. Remove 49.5 mL of supernatant (or more if possible)
            1. Best done by using first a 10 mL pipette to remove as much supernatant as possible without disturbing the precipitate
            2. then a 1 mL pipette to remove what could not be removed by the 10 mL pipette

3. then a 100 µL pipette to remove what could not be removed by the 1 mL pipette

iv. Redisperse GNRs in 50 mL of H_2O and sonicate for 1 minute

v. Centrifuge at 12,900 rpm for 20 min

vi. Remove supernatant using the same procedure described in 2a(iii)

vii. Dilute to 5 mL using H_20

b. Prepare PEG-thiol solution

i. Remove PEG-thiol from freezer and allow to warm to room temperature

ii. Measure 20 mg of PEG-thiol in a 20 mL vial

iii. Disperse in 5 mL of H_2O

c. Mix PEG-thiol solution and GNR solution

d. Place in oil bath set to 40 °C and stir at 200 rpm for 24 hours

e. Centrifuge.

i. Distribute sample into 2 centrifuge tubes (or 1 tube if a highly concentrated sample (~100× or 18 mg/mL) is require and dilute to 50 mL

ii. Centrifuge at 10,000 rpm (8,500 *g*) for 10 min

iii. Remove supernatant using the method describe in 2a(iii)

iv. Redisperse in 50 mL of desired solvent (water, ethanol, methanol, dichloromethane) and repeat centrifugation

v. Again remove as much supernatant as possible

vi. If a high concentration is needed, leave as is or dilute to desired concentration

Appendix 3. Identifying a Good Batch of CTAB

One of the challenges when producing GNRs is unreliable CTAB. Unfortunately, there can be significant lot-to-lot variability in the ability of CTAB to produce high-quality of GNRs. I have developed a protocol for identifying a good batch of CTAB, so that a larger amount of that lot can be purchased.

1. Buy a small container of CTAB when you are down to the last container of the old batch
    a. Call the supplier (Amresco) and see how many lots are available and how much of each lot they have stocked
    b. Purchase a small container of the lot for which they still have significant stock
2. Test the small batch
    a. Produce a batch of GNRs using the standard procedure established by Kozek et al. Quantities should be scaled to a 200 mL sample
    b. Examine the optical absorbance spectra of the primary and secondary growth
        i. Longitudinal LSPR
            1. Do the GNRs absorb at 800 nm?
            2. If not, is the LSPR 760 nm greater?

a. If less than 760 nm, this batch will probably not work
b. If above 760 nm the procedure can be modified to reach 800 nm

3. With proper dilution (0.5 mL GNRs + 2.5 mL CTAB solution), does the LSPR reach an absorbance of ~1.6.
4. Is the full width at half max (FWHM) consistent with GNRs you produce using a previous, good lot

ii. Transverse LSPR

1. Does the transverse peak look right?
   a. Is the peak small?
   b. Is the line shape correct?
   c. Are there any unexpected secondary peaks?

c. If the longitudinal LSPR is between 760-790 nm, do the following

i. Prepare 5 small batches of GNRs (30 mL scale) with different amounts of $AgNO_3$, but only prepare the primary growth solution

1. Warning. When preparing samples be aware of significant figures. If the scale only measures to 2 significant figures, increase the amount measured so that there are 3 significant figures
2. Prepare 5 samples using $1\times AgNO_3$, $1.1\times AgNO_3$, $1.2\times AgNO_3$, $1.3\times AgNO_3$, $1.4\times AgNO_3$, and $1.5\times AgNO_3$.

3. Measure at the absorption spectrum of each sample
    a. Does any sample have a longitudinal LSPR at ~820-840 nm
    b. If yes, does the rest of the spectrum look right?
    c. If the answer is yes for 1-2 samples, perform a secondary growth, and confirm that the GNRs absorb at ~800 nm

ii. Repeat on a larger scale

d. When you have a batch with absorbance spectrum that looks good, now do TEM on that sample

i. Acquire several images at a range of magnifications

ii. Do the GNR have the expected length and width?

iii. Is the shape of the ends round, flat, or dog-boned?

iv. Are there any irregular shapes (diamonds, boulders, cubes), and if so, are they acceptably infrequent? (This is why you should take many TEM images.)

3. Punctually call the company back and buy several kg of the good lot of CTAB while it is still available

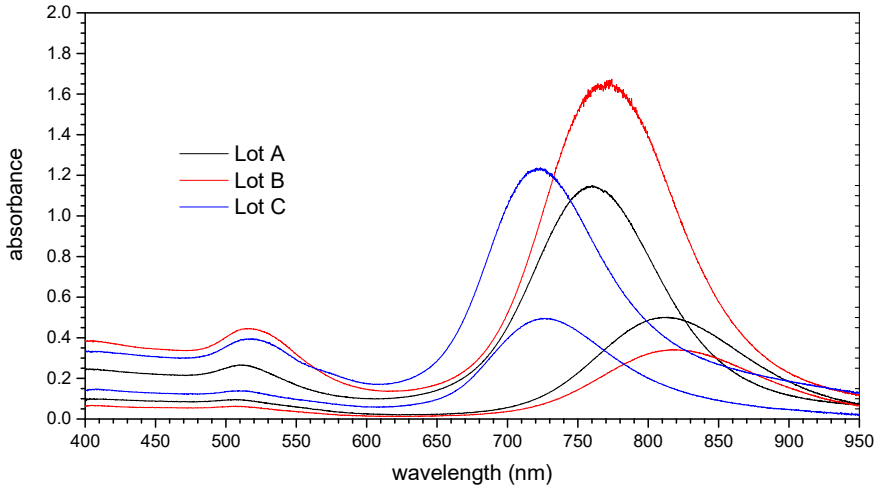

Figure A.1 Examples of absorbance spectra from primary and secondary growth of GNRs synthesized using different lots of CTAB using 1x$AgNO_3$. Lot B could potentially produce rods with a longitudinal LSPR at 800 nm.

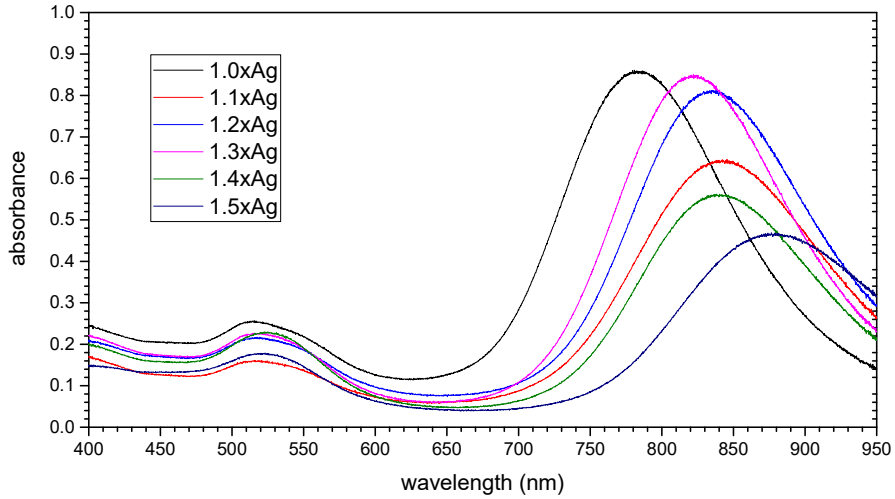

Figure A.2 Optical absorbance spectra of the primary growth of GNRs with using different amounts of Ag.

Appendix References

(1) Kozek, K. A.; Kozek, K. M.; Wu, W.-C.; Mishra, S. R.; Tracy, J. B. Large-Scale Synthesis of Gold Nanorods through Continuous Secondary Growth. *Chemistry of Materials* **2013**, *25*, 4537-4544.

(2) Wu, W. C. Multifunctional Gold Nanorods: Large-Scale Synthesis, Overcoating, Alignment, and Applications. North Carolina State University, 2014.